Understanding silicic volcanism: Constraints from elasticity and failure of vesicular magma

Inaugural-Dissertation

zur Erlangung des Doktorgrades

der Fakultät für Geowissenschaften der

Ludwig-Maximilians-Universität München

vorgelegt von

Bettina Scheu

07. Juli 2005

Contents

I

List of Figures

List of Tables

Preamble

Parts of this thesis are based on, or directly taken from papers to be published in scientific journals. Below, these papers are listed in order of their appearance in the text:

Kueppers U., Scheu B., Spieler O., Dingwell D.B., 2005. Field based density measurements as tool to recalculate pre-eruption dome structure: set-up and first results. Journal of Volcanology and Geothermal Research, 141, 65 - 75.

Scheu B., Kern H., Spieler O., Dingwell D.B., 2005. Temperature Dependence of Elastic P- and S-Wave Velocities in Porous Mt. Unzen Dacite. Accepted for publication at Journal of Volcanology and Geothermal Research.

Scheu B., Spieler O., Dingwell D.B., 2005. Dynamics of Explosive Volcanism at Unzen: an experimental Contribution. Accepted for publication at Bulletin of Volcanology.

Kennedy B., Spieler O., Scheu B., Kueppers U., Taddeucci J., Dingwell D.B., 2005. Conduit implosion during Vulcanian eruptions. Geology, 33, no. 7, 581-584, 2005.

Zusammenfassung

Seit jeher haben Vulkanausbrüche die Menschen fasziniert und ebenso in Angst und Schrecken versetzt. Weltweit entstanden unzählige Legenden über Götter und Dämonen um dieses Naturphänomen zu erklären. Vulkanausbrüche gibt es zwar seit Entstehung der Erde, ein gesteigertes Gefährdungspotential für den Menschen beinhalten sie jedoch erst, seit - ausgelöst durch einen größer werdenden sozioökonomischen Druck - vulkanische Gebiete immer dichter besiedelt werden. Ein damit verknüpftes Katastrophenpotential ergibt sich durch die immer dichter werdende Infrastruktur, sei es der Stromversorgung, Pipelines, Straßen oder der Flugrouten. In Anbetracht dessen ist Forschung zur Verbesserung des Verständnisses der Mechanismen von Vulkanausbrüchen und der sie begleitenden Phänomene, heutzutage wichtiger denn je. Die hierbei erzielten wissenschaftliche Erkenntnisse ermöglichen die immer genauere Erstellung von Gefährdungskarten und Notfallplänen.

Die vorliegende Arbeit beeinhaltet experimentelle Untersuchungen zum Bruchverhalten poröser Magmen sowie der Ausbreitungsgeschwindigkeit von elastischen Wellen in diesem Medium. Die hierbei gewonnen Erkenntnisse wurden mit Feldbeobachtungen abgegeglichen und ihre Bedeutung im Hinblick auf die für silikatreichen, explosiven Vulkanismus typischen Eruptionsprozesse analysiert.

Messungen mit einer Würfeltriaxialpresse im petrophysikalischen Labor der Universität Kiel ermöglichten die Bestimmung der Ausbreitungsgeschwindigkeiten elastischer Wellen in unterschiedlich porösen dazitischen Proben von Mt. Unzen (Japan). Hierbei wurde der Einfluß von erhöhtem Druck und erhöhter Temperatur in einem Bereich von bis zu 100 MPa und 600 °C auf die elastischen Eigenschaften der Dazite untersucht.

1

Hierbei konnte festgestellt werden, daß bei konstanter Temperatur die seismischen Geschwindigkeiten mit steigendem Druck zunehmen, während die Anisotropie der Geschwindigkeiten dabei abnimmt. Beides kann auf Kompaktion und das Schließen von Mikrorissen zurückgeführt werden. Bei einem angelegten Druck von 100 MPa konnten im untersuchten Dichtebereich von 1,93 - 2,50 g/cm^3 mittlere P-Wellen Geschwindigkeiten von 4,21 - 5,38 km/s sowie mittlere S-Wellen Geschwindigkeiten von 2,20 - 3,15 km/s gemessen werden.

Eine Erhöhung der Temperatur führte ebenfalls zu einer Erhöhung der Ausbreitungsgeschwindigkeiten elastischer Wellen und zu verringerten Anisotropien eben dieser. Dieser Trend muß besonders hervorgeboben werden, da genau das gegenläufige Verhalten für einen Großteil der sedimentären, metamorphen und eruptiven Gesteine festgestellt wurde. Der beobachtete Effekt kann auf eine Reduktion des Porenraums zurückgeführt werden. Das Schliessen von beim Abkühlen des Magmas entstandenen Mikrorissen aufgrund der Verminderung von thermischen Spannungen, kann ebenfalls zu einer Verringerung der Anisotropie und einer Erhöhung der seismischen Geschwindigkeiten mit steigender Temperatur beitragen. Bei 600 °C wurden mittlere P-Wellen Geschwindigkeiten von 4,31 - 5,64 km/s sowie mittlere S-Wellen Geschwindigkeiten von 2,20 - 3,32 km/s gemessen.

Das anisotrope Verhalten der Geschwindigkeiten kann in Zusammenhang mit der Textur der untersuchten Proben gebracht werden: Proben mit hoher Anisotropie weisen eine ausgeprägte Vorzugsrichtung der Phäno- und Mikrokristalle auf. Manchmal wurde zusätzlich zur Ausrichtung der Kristalle eine "Bänderung" innerhalb der Probe beobachtet, bestehend aus zumeist zwei Grundmassenschichten mit unterschiedlichem Mikrokristallgehalt. Da Kristalle üblicherweise parallel zur Fließrichtung im Magmenaufstiegkanals ausgerichtet sind, kann davon ausgegangen werden, dass die seismischen Geschwindigkeiten senkrecht zu dessen Wänden herabgesetzt sind.

Die physikalischen Eigenschaften von Magma in einem Vulkanschlot oder Dom sind ausschlaggebend für die Modellierung von Eruptionen. Im Rahmen dieser Arbeit wurden Probensätze dazitischer bzw. andesitischer Zusammensetzung von Mt. Unzen, Japan, sowie Soufrière Hills, Montserrat, Kleine Antillen, auf ihr Fragmentationsverhalten hin (Bruchschwellenwert und Fortpflanzungsgeschwindigkeit) analysiert. Die Untersuchungen hierzu wurden mittels eines auf dem Stoßrohr-prinzip basierenden

Fragmentationsapparates durchgeführt. Die dabei ablaufenden Prozesse lassen sich dem Bereich des Sprödbruches zuordnen. Die Ergebnisse zeigen, daß das Fragmentationsverhalten stark von der offenen Porosität und dem angelegtem Druck abhängt. Die Fortpflanzungsgeschwindigkeit des Fragmentationsprozesses folgt einem logarithmischem Zusammenhang mit dem angelegten Druckunterschied und steigt in aller Regel mit steigender Porosität der Probe, während der Bruchschwellenwert mit steigender Porosität, einem Exponentialtrend folgend, sinkt. In dieser Studie konnten an Proben in einem Porositätsbereich von 2,5 - 67,1 vol.% und bei angelegten Druckunterschieden von bis zu 40 MPa Fragmentationsgeschwindigkeiten zwischen 15 und 150 m/s gemessen werden. Die entsprechenden Bruchschwellenwerte in diesem Bereich kamen zwischen 30.0 - 2.5 MPa zu liegen.

Die den Fragmentationsprozess vorantreibende Energie wird größtenteils von der Expansion des unter Überdruck stehenden Gases im Porenraum der Probe geliefert. Die Resultate der Fragmentationsgeschwindigkeit aller untersuchten Proben weisen einen engen Zusammenhang mit der Energiedichte (der auf das Volumen standardisierten Fragmentationsenergie) auf. Sobald ein experimentell bestimmter Schwellenwert der Energiedichte von $(2,0 \pm 0,5) \cdot 10^{-6}$ J/m^3 überschritten war, konnte der bereits erwähnte logarithmische Anstieg der Geschwindigkeit der Fragmentation mit der Energiedichte beobachtet werden. Weiterhin konnte gezeigt werden, daß die Fortpflanzungsgeschwindigkeit der Fragmentation weitgehend unabhängig von Ursprung und Zusammensetzung der Proben ist. Dies unterstreicht die Schlüsselrolle der in der Gasphase gespeicherten Energie in bezug auf das Fragmentationverhalten.

Verschiedene Mechanismen können zu einer Fragmentation porösen Gesteines bei einer schnellen Dekompression führen. Eine „lagenweise" Fragmentation, verursacht durch das Bersten von Poren aufgrund des internen Gasüberdrucks, wird als der vorrangige Prozess angesehen, der zum Zerbrechen von porösem Gestein führt. Für niedrigporöse Proben konnte eine gesteigerte Bedeutung des Bruchprozesses nachgewiesen werden, der von einem durch das Gestein laufenden Entlastungsstoß nach der schnellen Dekompression verursacht wird. Desweiteren wurde der Einfluss der Permeabilität der untersuchten Proben auf das Fragmentationsverhalten evaluiert. Hier zeigte sich, dass eine hohe Permeabilität der Initiierung des Fragmentationsprozesses entgegenwirkt und die Fortpflanzungsgeschwindigkeit desselben bei einer gegebenen Energiedichte verringert.

Mit den erzielten Resultaten der Fragmentationsuntersuchungen wurden die Domkollaps-Ereignisse und die Vulkanianischen Explosionen der 1990-1995 Aktivitätsphase von Mt. Unzen, Japan, sowie die Vulkanianischen Ausbrüche 1997 von Soufrière Hills, Montserrat, analysiert. In den Ablagerungen der Block-und- Aschenströme des Mt. Unzen wurden große Blöcke gefunden, die Bänder bzw. Zonen unterschiedlicher Porosität aufweisen. Diese Beobachtung unterstützt die Modellvorstellung eines aus Bereichen unterschiedlicher Porosität aufgebauten Domes bzw. einzelner Domloben. Ähnlich hierzu ermöglichen es die von Montserrat stammenden Proben, einen Porositätsgradienten durch den Vulkanschlot zu postulieren, charakterisiert durch niedrig-poröses Magma nahe den Schlotwänden und hoch-poröses Magma im zentralen Bereich des Schlotes. Ein lagenweiser Aufbau eines Domes oder einzelner Domloben kann zu der Fragmentation nur einzelner dieser Lagen führen, zumeist gefolgt von einem Kollaps der darüberliegenden Bereiche. Solche Ereignisse vermögen gravitativ induzierte Domkollaps-Ereignisse zu katalysieren und können so zu heftigen pyroklastischen Strömen führen und / oder einen Sektorkollaps auslösen, dem wiederum Vulkanianische Explosionen folgen können. Ein Porositätsgradient innerhalb des Magmas in einem Schlot resultiert in einer konkaven Ausbildung der Fragmentationsfront und schafft damit die Voraussetzungen für laterale Fragmentation von dichterem Magma nahe der Schlotwände. Derartige „Schlot-Implosionen " sind während der meisten explosiven Eruptionen möglich und können den Ablauf einer Eruption beeinflussen, indem sie zu einer Pulsation oder gar zum Erliegen dieser führen können.

Der langsame Magmenaufstieg und die langsame Extrusionsrate des Mt. Unzen führte zu relativ dichtem extrudierten Magma, da das Magma während des Aufstiegs fast vollständig entgasen konnte. Die im allgemeinen niedrige Porosität dieses Magmas verursacht bei dem Großteil des Materials einen hohen Fragmentationsschwellenwert. Dieser ist zu hoch für eine rein durch Gasüberdruck induzierte Fragmentation. Daher traten innerhalb der Aktivitätsphase von 1990-1995 hauptsächlich gravitativ bedingte Domkollaps-Ereignisse auf, welche in einer Vielzahl von Block-und-Aschenströmen resultierten. Kollaps-Ereignisse, verstärkt durch die Fragmentation einzelner Bereiche, wie in der vorgelegten Arbeit ausgeführt, sind ebenso denkbar. Dies trifft vorallem auf die von energiereichen pyroklastischen Strömen begleiteten, lang andauernden Kollaps-Ereignisse im frühen Stadium der Aktivitätsphase im Juni 1991 zu. Diese wur-

den von schwächeren Vulkanianischen Explosionen gefolgt. Eine stärkere explosive Tätigkeit blieb aus, auch wenn dies im Rahmen eines großen Hangrutsch / Schuttlawine oder eines Sektorkollaps des Vulkanbaus, ähnlich zu dem Lateral-Kollaps des Mt. St. Helens am 18. Mai 1980, möglich gewesen wäre.

Ähnlich zu dem Verhalten des Mt. Unzen, wurde auch die erste Aktivitätsphase von Soufrière Hills, Montserrat, gekennzeichnet durch eine Vielzahl von Domkollaps-Ereignissen, begleitet von heftigen pyroklastischen Strömen. Da die Extrusionsrate des Magmas in dieser Phase relativ hoch war, wurde im Vergleich zu Mt. Unzen höher poröses Magma gefördert, was in einer explosiveren Entwicklung der vulkanischen Aktivität resultierte. Große Kollaps-Ereignisse des Vulkandomes führten häufig zu Vulkanianischen Explosionen, von August bis September 1997 traten sogar zwei Zyklen Vulkanianischen Explosionstätigkeit auf. Basierend auf den experimentell gewonnenen Daten der Fragmentationsgeschwindigkeit, konnten für diese Explosionen Fragmentationstiefen von bis zu 1500 m berechnet werden. Diese Werte stimmen gut mit den Ergebnissen numerischer Modelle sowie vor Ort gemachten Beobachtungen überein.

Der Stil und die Entwicklung einer Eruption ist abhängig von den Eigenschaften des geförderten blasenhaltigen Magmas. Falls dessen Bruchschwellenwert innerhalb des Ausbruchsgeschehens überschritten wird, wechselt das Regime zur explosiven Tätigkeit. Andernfalls wird das Magma ruhig extrudiert und ein Dom gebildet. Die Übergangszone zwischen porösem Magma im zentralen Bereich des Magmenaufstiegkanals und dichtem Magma nahe den Schlotwänden bzw. den Schlotwänden selber birgt maßgebliche Implikationen, sowohl für explosive Ausbruchstätigkeit, als auch für Ausbreitung seismischer Signale. Innerhalb der Übergangszone ebenso wie im angrenzenden Nebengestein kann eine ausschlaggebende Änderung der Temperatur ebenso wie der Porosität angenommen werden. Laterale Fragmentation aufgrund der unterschiedlichen Porosität innerhalb dieser Übergangszone kann die Entwicklung des explosiven Geschehens erheblich beeinflußen. Aus dem Temperaturunterschied in den niedrig porösen Schlotwänden resultiert eine signifikante Verschiebung der Ausbreitungsgeschwindigkeiten elastischer Wellen und dies kann sogar in manchen Fällen zu in dieser Schicht gefangenen Wellen führen, wie dies z.B. in Montserrat beobachtet wurde.

Abschließend kann festgestellt werden, daß die im Rahmen der vorliegenden Arbeit erzielten Ergebnisse Folgerungen für verschiedene Bereiche eines Vulkankomplexes mit der Übergangszone als Verbindungsglied erlauben. Die gewonnenen Daten ermöglichen eine bessere Evaluierung der Eigenschaften silikatreicher vulkanischer Gesteine in einem oberfächennahen Bereich innerhalb eines vulkanischen Komplexes, z.B. bei den Wänden des Magmenaufstiegkanals. Diese Abschätzungen sind von grundlegender Bedeutung für die numerische Simulierung der im Vulkanschlot ablaufenden Prozesse während eines Ausbruchs, ebenso wie für die Modellierung vulkanoseismischer Daten. Somit stellen die hier vorgestellten Ergebnisse einen Baustein dar, auf dem Weg zu einer verbesserten Auswertung von prä-eruptiven Phänomenen in vulkanischen Gebieten und zu einer verfeinerten Abschätzung des Risikopotentials einzelner vulkanisch aktiver Gebiete.

Chapter 1

Introduction

1.1   Silicic volcanism: explosive versus effusive

"A volcano is a mountain with a Jekyll and Hyde personality. For most of its life, it is inactive. Ones image is that of a graceful cone, capped with snow, commanding the cherry-blossom-draped landscape of a Japanese travel poster. This serene mood may continue for millennia, until the darker side of the volcanos character is abruptly manifested in a violent eruption. Convoluted clouds climb many kilometres into the atmosphere, bringing darkness at noon, and raining hot ashes on towns and villages beneath. Tongues of molten rock ooze down the slopes of the volcano, engulfing the flimsy structures standing in their way."
(Francis and Oppenheimer, Volcanoes)

In ancient societies, volcanoes were often regarded as the manifestation of deities or evil spirits and treated with respect but also with superstitious fear. In fact, volcanic eruptions are one of the most spectacular and dangerous natural phenomena. Volcanic activity can either be effusive, dominated by quiescent emission of lava or explosive, dominated by the eruption of pyroclastic material. A rapid transition between these two regimes is possible. On a broad scale, a clear distinction of the eruption style can be drawn by magma composition. Large-scale basaltic eruptions are mostly effusive,

whereas large-scale silicic eruptions are mostly explosive. Thus silicic volcanism possesses a severe hazard potential and can have devastating effects on human population. The eruptions of volcanoes like Vesuvius (Italy), Krakatau and Tambora (both Indonesia), Mount St. Helens (USA) or Pinatubo (Philippine) serve as examples.

Recent dome forming eruptions such as Mount St. Helens (USA), Unzen Volcano (Japan) or Soufrière Hills Volcano (Montserrat, West Indies), have provided opportunities for detailed study of many volcanic processes including effusive and explosive behavior. The transitions in eruptive style have been explained principally by differences in magma ascent rate and resultant changes in efficiency of ascent-driven degassing and crystallization, with its enormous effect on magma rheology (*Eichelberger et al.*, 1986; *Jaupart and Allègre*, 1991; *Melnik and Sparks*, 1999; *Nakada and Motomura*, 1999).

Lava dome eruptions are an important example of effusive silicic activity. The chemistry and phenocryst abundance of the dacite of the 1990 - 1995 lava dome eruption at Unzen (Japan), which occurred without large explosive eruptions, is similar to dacites of the 1980 - 1986 eruption at Mount St. Helens (*Cashman*, 1992), and of the 1991 eruption at Pinatubo (*Pallister et al.*, 1992), both of which produced large-scale Plinian explosions. The recent dome eruption at Soufrière Hills Volcano, Montserrat, West Indies (*Young et al.*, 1997) is another example of effusive eruption which, like Unzen, was not preceded by large explosive eruptions. However, many Vulcanian explosions that occurred during the dome growth at Soufrière Hills were more violent than those at Unzen, and produced pumiceous pyroclastic flows. Unzen, therefore, is the most purely effusive least explosive example among recent dome eruptions of silicic to intermediate magma.

1.2   Fragmentation process

Explosive eruptions are thought to be generated by two fundamentally different mechanisms. 1) magmatic fragmentation, caused solely by gas originally dissolved in the magma and 2) phreatomagmatic fragmentation, where magma interacts with external water. This study is focused on magmatic fragmentation, and attempts to advance our understanding of the fragmentation process itself, as this is the defining feature of an

explosive event.

Fragmentation is the process of disintegrating magma into pyroclasts. During fragmentation the potential energy stored in overpressure in bubbles and melt is used to fracture the magma and creating new surface, the surplus is transformed into kinetic energy of ejected particles. Magmatic fragmentation may occur associated with high ascent rates of magma, leading to Plinian eruptions, or via rapid decompression of a volcanic system by e.g. a dome collapse resulting mostly in Vulcanian eruptions. Additionally, fragmentation of hot rocks may as well occur in smaller scale due to impact processes during dome collapse and block-and-ash flow events. All mentioned processes may take place within a single eruptive crisis (*Cashman et al.*, 2000).

Various models have been proposed for fragmentation. They have been based on investigations of deposits of explosive eruptions, theoretical models and laboratory experiments. Early models mentioned magma disruption by bubble coalescence as main mechanism (*Verhoogen*, 1951). However, *McBirney and Murase* (1970) and *Sparks* (1978) demonstrated that coalescence is unlikely to be the leading fragmentation mechanism for highly viscous magmas, although possibly applicable for eruptions of low viscosity magmas. Basically two main groups of processes leading to fragmentation can be distinguished:

Fragmentation due to rapidly accelerating two phase flow

Hereby the driving force for expansion and acceleration is derived from vesiculation and bubble growth. High strain rates within the magma cause the fragmentation, either due to instabilities in the fluid (ductile) or by brittle fracture. Low-viscosity magma is likely to fragment by fluid instabilities resulting in Hawaiian fire fountains or Strombolian bubble bursts. Fragmentation by brittle fracture due to high strain rates may be important for Plinian eruptions of higher viscous magma. (*Dingwell and Webb*, 1989; *Gilbert and Sparks*, 1998; *Papale et al.*, 1998; *Papale*, 1999; *Cashman et al.*, 2000).

Fragmentation of vesicular magma due to rapid decompression of an edifice

This fragmentation process likely accounts for the eruption style of most silicic events, e.g. for dome collapse events and for the disintegration of (highly) viscous magma in
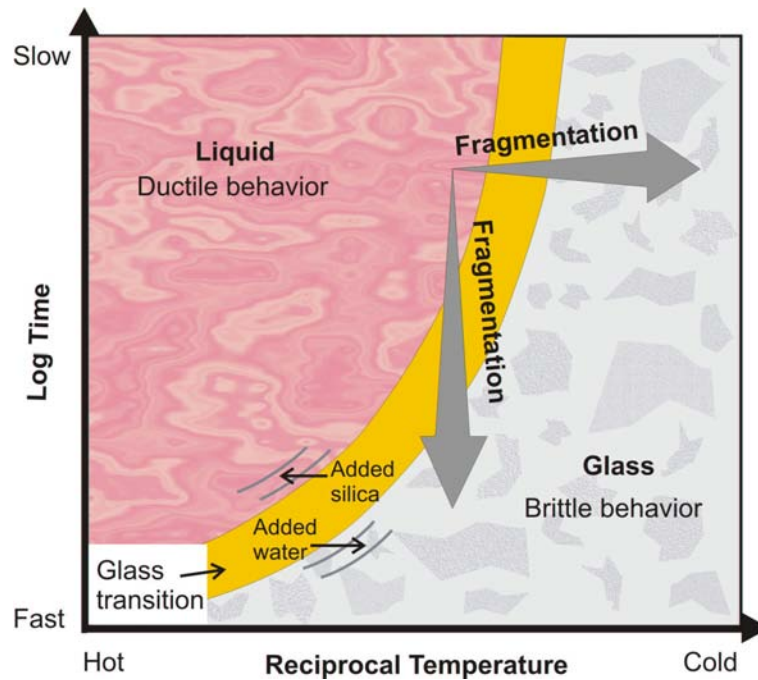
Figure 1.1: The glass transition in a plot of the deformation time against the reciprocal temperature. Above the glass transition magma behaves like a viscous liquid and responds ductile to deformation. Below the glass transition magma behaves solid-like resulting in brittle deformation. The glass transition can be crossed from the liquid to the solid field either by cooling or by accelerating the deformation process (modified after *Dingwell* (1996)).

Vulcanian eruptions. It may further contribute to Plinian eruptions of silicic magma, most likely in combination with the mechanism, mentioned above.

In most cases silicic, high-viscous magma will disrupt in a brittle manner. This is caused by the behavior of magma close to the glass transition. The glass transition is temperature dependent and marks the change from ductile to brittle response of magma to strain (Fig. 1.1). It can be crossed either by cooling due to magma ascent or emplacement, or an increase in the strain rate. An enhancement in silica content increases the melt viscosity and thus widens the brittle field towards higher temperature. Similarly, the loss of volatiles (water) shifts the glass transition to higher temperatures. As magma fragmentation is a relatively rapid physical process, subjecting vesicular magma to high deformation rates, the fracture process is likely to occur brittle.

Alidibirov and Dingwell (2000) considered three mechanisms for fragmentation of high viscosity vesicular magma based on the assumption of the brittle character of fragmentation. Fragmentation may be caused by:

- unloading elastic wave propagation

- layer-by-layer vesicle bursting (fragmentation wave)

- gas-filtration flow

The first process is the fastest one, as the unloading wave will propagate downward through the vesicular magma with a speed of sound. Thereby failure of vesicular magma may occur if the tensile stress, exerted by the unloading wave, exceeds the tensile strength of the vesicular magma. As the unloading elastic wave migrates through the vesicular magma, it exposes the magma to tensile stresses in relevant section leading to disruption of the magma by generation of cracks parallel to the wave front. This mechanism can be amplified by the expansion of compressed gas in the bubbles. This may lead to additional cracking or fragmentation and will mainly enhance the ejection of the gas-particle mixture. The velocity of fragmentation will be determined in this case mainly by the mechanical properties of material and the sound speed can be considered as the upper limit (*Alidibirov and Dingwell*, 2000). Similar models have been assumed for rock burst processes (*Kovalenko*, 1980; *Poplawski*, 1997).

At the second mechanism, the stress exerted on the magma by the unloading wave is not high enough to cause fragmentation. Rather a sudden decompression resulting in bursting of vesicles drives this process. A pressure gradient is built up at top of the magma body between the pressurized gas in the vesicles and the low pressure area behind the unloading wave. At a certain pressure differential, the tensile strength of the magma is overcome and the brittle disruption of the upper layer within the vesicular magma will occur. The fragments are ejected with the remaining energy of the expanding gas phase. Now a newly formed free surface is exposed to low pressures and again a pressure gradient is built up, leading to the fragmentation of the next layer. Thus, a layer-by-layer fragmentation process (fragmentation wave) moves downwards into the magma (*Alidibirov and Dingwell*, 2000). Calculations demonstrate that fragmentation wave velocity should be far slower than the speed of sound. This was confirmed subsequently experimentally at values between 2 - 110 m/s (*Spieler et al.*, 2004a).

For vesicular magma with connected pores undergoing a rapid decompression event which is neither fragmented by the unloading wave propagation, nor by layer-by-layer vesicle bursting, a third fragmentation mechanism, caused by the rapid gas flow through the sample, was proposed by (*Alidibirov and Dingwell*, 2000). Drag forces and the tortuosity of gas flow caused by the skeletal form of the vesicular magma matrix may sustain a pressure gradient and corresponding tensile stress is imposed on the vesicular magma. If this tensile stress exceeds the tensile strength of the vesicular magma, then the magma will be disrupted. This is the slowest of the mentioned mechanisms for fragmentation during rapid decompression.

The layer-by-layer fragmentation is now widely accepted as being the predominant fracturing process caused by rapid decompression (*Cashman et al.*, 2000; *Melnik*, 2000; *Ichihara et al.*, 2002). Nevertheless some combination of the different mechanisms is likely. Several physical models were proposed accounting the stress distribution caused by pressurized gas within the vesicles of a magma body. *McBirney and Murase* (1970) used solely elasticity theory and Griffith theory. More recent models are based on the stress distribution of thin walled spheres (*Alidibirov*, 1994) or thick walled spheres (*Zhang*, 1999). A comparative study of this models, including a comparison to experimental data, showed that none of these approaches fit the entire range of data accurately enough, leading to the suggestion that the process is intrinsically more complex.

1.3   Experimental volcanology

The investigation of volcanic eruptions and magmatic processes is becoming increasingly systematic, quantitative and rigorous. This is partially driven by rising importance of hazard and risk management, which requires reliable and quantitative predictions of volcanic processes to substantiate decisions during volcanic crises. However, the scientific study of volcanic phenomena cannot rely solely on field data, as direct observations of eruption processes in the field are limited to those parts of an eruption that are accessible. This restricts detailed observations to a limited range of superficial processes. Thus intense laboratory experimentation is becoming an increasingly important feature within volcanic research, as experiments are used to explore novel phenomena and to provide systematic observations of processes. Further laboratory experiments

permit the determination of values of key parameters, testing of hypotheses and theoretical models, and validation of computational models (*Mader et al.*, 2004). More recently, experiments have become more widely applied to the investigations of complex dynamical processes and their mechanisms. Nevertheless, experiments on natural materials provide a certain "ground truthing"of the applicability of analogue material experiments. They may also exploit material-specific mechanisms wholly inaccessible to analogue material experiments.

In a laboratory experiment, the problems of accessibility are reduced significantly. The process can be repeated at fixed conditions and the known starting conditions can be correlated with the results. The experiments can be divided into those using natural materials and those that use non-magmatic materials, so-called magma analogues. This duality has to be taken into account for the strengths and limitations of the experimental approach. For example, the dynamic process of bubble nucleation and growth has been widely studied by decompression experiments on natural melts (*Hurwitz and Navon*, 1994; *Gardner et al.*, 1999; *Mourtada-Bonnefoi and Laporte*, 2000; *Mangan and Sisson*, 2000; *Lensky et al.*, 2004). As natural materials can be extremely complex in composition and texture, it can be difficult to reproduce the starting conditions. Many of these problems are circumvented by the use of analogue materials. For example, waxes are often used to study lava flow mechanics and morphology as they reproduce the transition from liquid to solid at easily accessible temperatures (e.g. *Fink and Griffiths*, 1990; *Lyman et al.*, 2004).

Fragmentation experiments

The study of magmatic fragmentation provides a good example of the way dynamic experiments using both analogue and natural materials can interface with hypotheses and numerical models to lead to a better understanding of a highly complex process that is inaccessible to direct observation in the field (*Mader et al.*, 2004).

During the last decades, the fragmentation behavior has been (largely in the absence of any experimental data) frequently discussed in theoretical models (e.g. *Sparks*, 1978; *Sugioka and Bursik*, 1995; *Papale*, 1999; *Zhang*, 1999; *Alidibirov and Dingwell*, 2000) and numerical models (e.g. *Dobran*, 1992; *Melnik*, 2000) describing conduit and eruption processes. Several fragmentation experiments, sometimes combined

with degassing experiments, have been performed on analogue materials, as H_2O-CO_2 polymer or gum-rosin-acetone systems (*Mader et al.*, 1994; *Phillips et al.*, 1995; *Zhang et al.*, 1997; *Mourtada-Bonnefoi and Mader*, 2004). Experiments on viscoelastic silicone oil derivatives allowed to have a closer look on the physical (brittle - ductile) behavior of magma during rapid expansion and fragmentation (*Ichihara et al.*, 2002). Experiments on natural magma were carried out first by *Alidibirov and Dingwell* (1996a,b). These experiments and subsequent studies of this nature have demonstrated that the dependence of a number of parameters on a wide variety of natural samples could be accessed, including importantly the analysis of fragmented pyroclasts (*Dingwell*, 1998; *Martel et al.*, 2000; *Spieler et al.*, 2003, 2004b; *Mueller et al.*, 2005; *Kueppers et al.*, 2005a).

1.4 Eruption history of Unzen Volcano

Unzen Volcano (Mt. Unzen), is located in the central part of Shimabara Peninsula, Kyushu, Southwest Japan, approximately 70 km west of the volcanic front of the Southwest Japan arc, which is related to the steeply dipping subduction zone of the Philippine Sea plate. Upwelling of mantle in the back-arc region may be responsible for magma genesis in the Unzen area (*Nakada et al.*, 1999). Unzen Volcano is situated in a volcanotectonic depression, the Unzen Graben, which spreads in N-S direction at a rate of 1.4 cm/year (*Tada*, 1985). The Unzen Graben is the western part of a larger graben system, the 20 - 30 km wide Beppu-Shimabara Graben System, trending in an ENE-WSW direction across central Kyushu (*Umakoshi et al.*, 2001).

Unzen Volcano started its activity about 0.5 Myr ago and maintained its growth resulting in the formation of a massive volcanic edifice. The eruption products are andesitic to dacitic in composition and consist mainly of thick lava flows, domes and their collapse deposits (*Nakada and Motomura*, 1999; *Hoshizumi et al.*, 1999).

Lava dome eruptions around Mt. Fugen, the central peak of Unzen Volcano, occurred every 4000 - 5000 years. Historical eruptions took place in 1663, 1792, and 1990 - 1995 (*Nakada and Motomura*, 1999).

1990 - 1995 eruption

Elevated seismic activity of Shimabara Peninsula began in 1985, mostly in the area of Tachibana Bay, about 15 km west of Unzen Volcano. Seismicity was greatest the entire year before the eruption, starting with a vigorous volcano-tectonic swarm in November 1989. The hypocenter migrated eastward from about 15 km depth below Tachibana Bay towards the summit of Unzen Volcano, shallowing in an angle of roughly 40° - 50° (*Umakoshi et al.*, 2001). The eruption started on 17 November 1990 with a small phreatic eruption, followed by phreatomagmatic explosions in February 1991. First lava extrusion occurred on 20 May 1991 and continued at changing effusion rates until February 1995. High effusion rate resulted in exogenous dome growth and low effusion rate in endogenous growth (*Nakada et al.*, 1999). During this eruption 13 lobes were extruded as result of exogenous dome growth and formed a complex dome that extends down the eastern flank of Unzen. Each lobe extrusion was preceded by earthquake swarms. The dome growth was accompanied by frequent pyroclastic flows and some minor explosive events. The majority and the most violent pyroclastic flows occurred at the initial stage during a period of high effusion rate, most of them were triggered by dome collapse events. An unexpectedly large pyroclastic flow led to 43 fatalities on 3 June 1991 (*Nakada et al.*, 1999). Large dome collapse events resulted in vigorous pyroclastic flows on 8 June 1991 and 15 September 1991, the first of them was accompanied by explosions. Vulcanian explosions occurred in June and August 1991, the two largest on 8 and 11 June 1991. The former was associated with series of pyroclastic flows triggered by a collapse of big parts of the dome. The Vulcanian explosions were accompanied by shallow earthquakes located at a depth of about 500 m below surface (*Nakada et al.*, 1999). Pumices produced during the Vulcanian explosions could only be found in the Peléan pyroclastic-flow deposits of June 1991 (*Yanagi et al.*, 1992). Preceded by a seismic crisis, a second pulse of effusion occurred in February 1993, resulting in large pyroclastic flows during March to June 1993. The eruption finished in February 1995 with extrusion of a spine at the endogenous dome (*Nakada et al.*, 1999).

1.5   Eruption history of Soufrière Hills Volcano

The island of Montserrat is located in the northern part of the $\sim$ 750 km long Lesser Antilles island arc, which formed by westward subduction of the Atlantic oceanic lithosphere beneath the Caribbean Plate. Volcanic activity started on Montserrat about 4 - 5 Myr ago. Five centers, all mainly andesitic, have been active since that time, Soufrière Hills Volcano is the most recent one. The 1995 - present eruption of Soufrière Hills Volcano is the latest series of andesitic, dome forming eruptions in a history spanning more than 175 kyr (*Roobol and Smith*, 1998; *Harford et al.*, 2003).

1995 - present eruption

The recent period of activity of Soufrière Hills Volcano started 1896 with a seismic swarm lasting for a year and was followed by three more seismic crisis at about 30 years intervals, the last one starting 1992 and continuing till the beginning of the eruption (*Robertson et al.*, 2000). The current period of activity is thought to be triggered by the injection of magma with basaltic or basaltic andesite composition into a pre-existing andesitic magma storage region (*Devine et al.*, 1998, 2003).

To date, two different phases of the eruption can be distinguished, both involving prolonged phases of andesitic dome growth at the volcano's summit. The first phase lasted from November 1995 to March 1998. It started with increasingly energetic phreatic activity and continued with vigorous dome growth, pyroclastic flows and surges, Vulcanian explosions and one debris avalanche that triggered a lateral blast on 26 December 1997 (*Robertson et al.*, 2000; *Druitt et al.*, 2002; *Woods et al.*, 2002). This phase was followed by a period of residual activity, including dome degradation and further explosive events but almost no extrusion of fresh lava (*Norton et al.*, 2002).

The second phase started in November 1999, again with the extrusion of fresh andesitic magma and lasted till end of July 2003. Generally this phase involved more stable dome growth and significantly fewer periods of vigorous pyroclastic flow and collapse activity than the first phase. Thus the active dome was able to attain larger volumes. Nevertheless, this phase was interrupted by three major dome collapse events (20 March 2000, 29 July 2001 and 12 July 2003), the third of which removed $> 100 \cdot 10^6$ m^3. All produced pyroclastic flows, significant ash clouds and extensive

lahars as well as debris flows. However, the expected vigorous Vulcanian eruptions accompanying dome collapse events of that size, did not take place, only minor explosive events occurred (*Carn et al.*, 2004). All three major collapses coincided with periods of exceptionally intense rainfall on the island, and thus were classified as rainfall-triggered collapse events (*Matthews et al.*, 2002; *Elsworth et al.*, 2004). This second phase is again followed by a still ongoing period of residual volcanic activity consisting of ash venting, mild explosions and minor dome-collapse and virtually no dome growth.

Chapter 2

Sample characterization

2.1 Petrology

2.1.1 Unzen Volcano, Japan

The last period of activity of Unzen volcano took place from 1990 until 1995 (*Nakada et al.*, 1999). During this time, the SiO_2 content of the erupted magma remained nearly constant around 65 wt.%. The erupted lavas are porphyritic and contain 23 - 28 vol.% phenocrysts of plagioclase, hornblende, biotite and quartz (Fig. 2.1). Plagioclase and hornblende exhibit the largest phenocrysts with average sizes up to 5 mm (*Nakada and Motomura*, 1999). The groundmass is composed of rhyolitic glass (78 - 80 wt.% SiO_2) with microlites of plagioclase, pargasite, pyroxene, Fe-Ti oxides, and apatite. The groundmass crystallinity appears to be related to the magma ascent rate, as it rises from 33 wt.% up to 50 wt.% with decreasing effusion rate (*Nakada and Motomura*, 1999).

Experimental petrologic studies postulate a water content of 6 wt. % for the pre-eruptive magma (*Kusakabe et al.*, 1999; *Botcharnikov et al.*, 2003). However, the water content in the extruded magma is about 0.25 wt.% for the bulk rock of the 1991 eruption products and negligible in the latest stage of the eruption. For breadcrust bombs a water content of 0.5 wt.% was measured in the chilled margin and 0.3 wt.% in the core and the blocks from the dome also had 0.3 wt.% water (*Kusakabe et al.*, 1999).

Photographs and scanned thin sections of the analyzed samples are shown in appendix A.1 and A.2. Therein an average size of around 5-6 mm was found at the large hornblende and plagioclase phenocrysts in agreement with *Nakada and Motomura* (1999). The largest plagioclase crystals reach up to 15 mm in length. A preferred phenocryst orientation is clearly observable in the denser samples. In the breadcrust bombs the phenocryst content was found to be lower than in the extruded magma (Fig. A.1). A flow alignment of the microlites within the groundmass parallel to orientation of the phenocrysts is also apparent from the photomicrographs (Fig. 2.1a - c). Although highly porous samples show a tendency for more random phenocryst orientation, a slight alignment is still discernable (Fig. appendix). The bubbles are irregular shaped, often fringed and hardly aligned (Fig. 2.1c, d). In the dense samples bubbles are often attached to phenocryst surfaces (Fig. 2.1a). The breadcrust bombs show a lower microlite content than the extruded magma. The vesicles within the breadcrust bomb are quite small, irregularly shaped and show incipient coalescence (Fig. 2.1d).

2.1.2 Soufrière Hills Volcano, Montserrat

The andesites erupted at Soufrière Hills Volcano are typically highly porphyritic and contain 58 - 62 wt.% SiO_2 (Fig. 2.2a, b). They consist of about 45 - 55 wt.% phenocrysts ($> 300 \, \mu$m), 15 - 20 wt.% microphenocrysts (300 - 100 μm) and 20 - 30 wt.% microlites (groundmass crystals $< 100 \, \mu$m). The groundmass is composed of rhyolitic glass with an SiO_2 content of 76 - 79 wt.% (*Horwell et al.*, 2001; *Murphy et al.*, 2000). The glass content varies from 35 to 5 wt.% with high contents to be found in samples presumably erupted at higher discharge rates. Concordantly the glass content of the pumices was estimated to 30 - 35 wt.%. The main phenocrysts are plagioclase (30 - 35 %), amphibole (6 - 10 %), orthopyroxene, titanomagnetite and minor quartz (*Horwell et al.*, 2001). The composition of the lava did not vary in any systematic way throughout the eruption (*Devine et al.*, 1998; *Murphy et al.*, 2000).

The water content of the glass matrix in pumice clasts was found to be 0.2 -0.6 wt.%. A residual water content of 1.8 wt.% was observed for a ballistic block ejected at the sub-Plinian explosive event on 17 September 1996. Matrix glass water contents are low (< 1 wt.%) compared with the water content of plagioclase melts inclusions of 4.3 ± 0.5 wt.%, measured by FTIR (*Barclay et al.*, 1998; *Harford et al.*, 2003). This
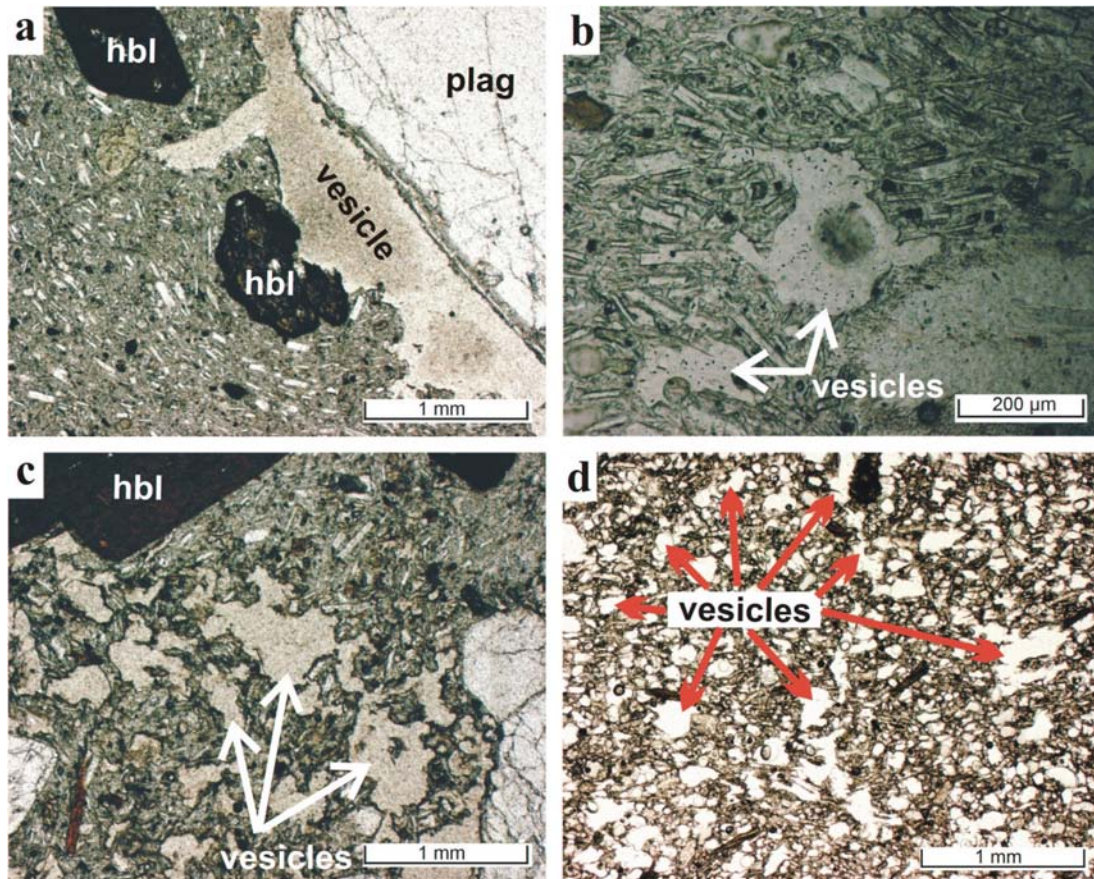
Figure 2.1: Thin section images of Unzen dacite. (a) A large vesicle attached to a large plagioclase and limited by a hornblende crystal. The crystals in the groundmass are mostly aligned and follow the stress distribution around the large phenocryst with the attached vesicle. (b) The groundmass is microlite-rich. The microlites are aligned and exhibit flow alignment around small vesicles. (c) A highly porous sample, showing fringed, possibly collapsed vesicles, which are poorly elongated or aligned. This vesicle shape was also observed in dense samples. (d) The interior of a breadcrust bomb. The vesicles are quite small and irregularly formed. Signs of bubble coalescence can be found.

indicates that water degasses efficiently during eruption at Montserrat.

Matrix glass compositions of andesites from the current eruption of Montserrat indicate 20 - 70 wt.% groundmass crystallization (*Harford et al.*, 2003). The large spectrum of observed crystallinity is attributed to the variation in extrusion rates and in residence time and location within the lava dome.

An average size of 2-4 mm was observed for the phenocrysts at the Montserrat andesite (Fig. 2.2a, b and A.1). Only the pumice contained large, often broken hornblende and plagioclase phenocrysts with up to 10 mm in length (Fig. A.1). A preferred orientation of the phenocrysts is observed in denser samples as well as in the pumice (Fig. A.1). Flow alignment of the microlites within the groundmass could be found mostly parallel to orientation of the phenocrysts (Fig. 2.2a). The size of vesicles found in the pumice varies strongly. The vesicles are irregularly formed and highly interconnected (Fig. 2.2c). In denser rocks vesicles are mostly smaller and roughly aligned (Fig. 2.2d). Signs for bubble coalescence can be observed in pumice and dense rocks.

2.2   Density and porosity

Common methods to determine the density and porosity of rocks are based either on complete water saturation of the sample (*Belikov et al.*, 1964; *Schopper*, 1982; *Cas and Wright*, 1987; *Gardner et al.*, 1996) or coating of the sample surface with materials as saran (*Mayfield and Schiffman*, 1998) or cellulose acetate (*Polacci et al.*, 2003). A method to determine the porosity together with the pore size distribution is given by the mercury-intrusion method (*Belikov et al.*, 1964). It requires small samples and is only applicable up to a certain pore size: At large pores the surface tension of the mercury becomes too high to ensure a complete moistening. All these methods have disadvantages as being time-intensive (water saturation) or changing the samples irreversibly (coating, Hg intrusion).

The total volume of accessible pore space as well as bubble shape, size, and distribution crucially affects the fragmentation behavior and the elastic wave velocities. Therefore, for this work the porosity of all samples was carefully analyzed.
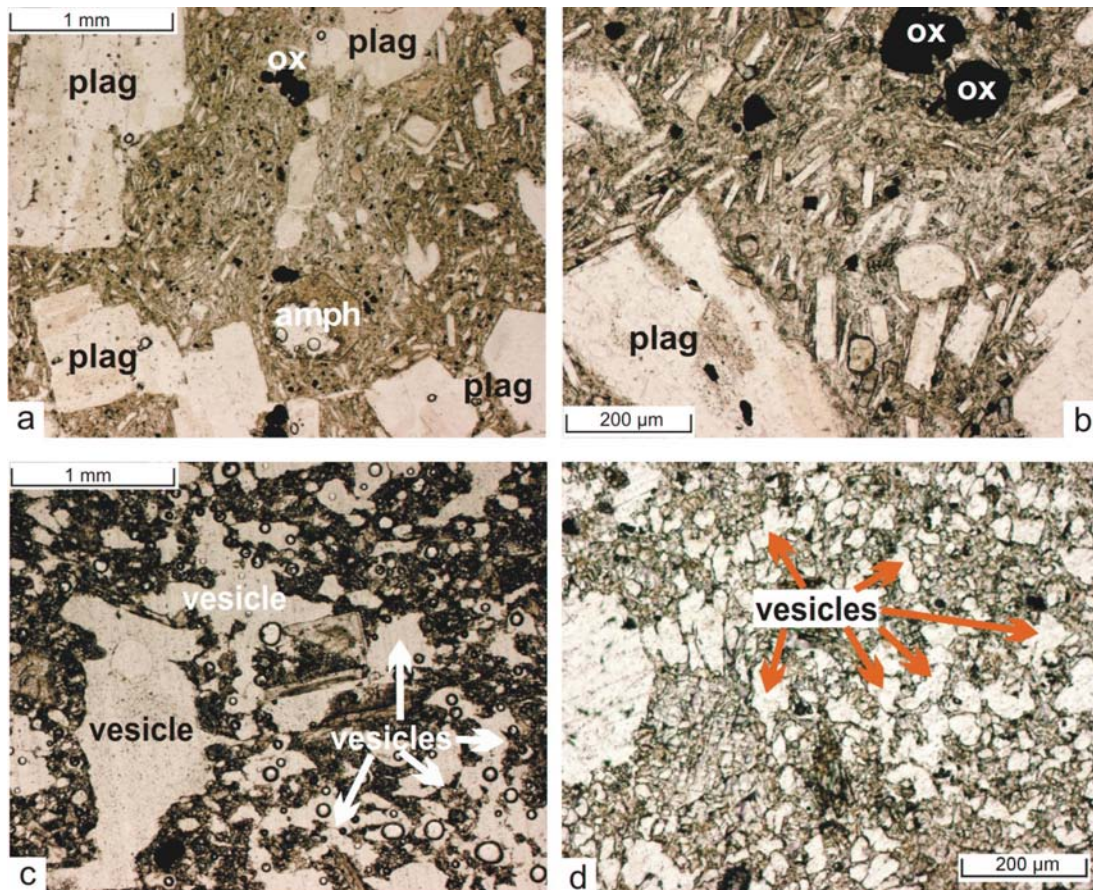
Figure 2.2: Thin section images of Montserrat andesite. (a) The erupted andesite is porphyritic and rich in microlites. In the central part of the image a vertical, brighter band can be observed. This band has a lower microlite content than the darker areas. (b) The groundmass is microlite-rich. The microlites are mostly aligned and "flow" around the phenocrysts and microphenocrysts (here oxides). (c) Image of a pumice sample. The glass content is higher compared to samples a, b, d. The vesicles are irregularly shaped, very variable in size and seem to be highly connected. The small thick walled spherical bubbles are artifacts of the thin section preparation. (d) In the denser samples very small vesicles can be observed which are slightly aligned.

2.2.1   Field measurements

To determine the density distribution of a huge amount of samples at a medium size range ($\sim 3 \times 10^{-3}$ m^3) as for example pyroclastic flow deposits, an in situ technique was developed following the Archimedean principle. Therefore samples were placed in plastic bags, evacuated and sealed, and their buoyancy in water was determined (*Kueppers et al.*, 2005a). This method quickly yields the bulk density of irregular formed samples.

At Unzen Volcano both, field and laboratory density measurements were carried out. During field work in 2000 the field density technique was successfully tested. In 2001 an extensive density mapping of the block-and-ash flow deposits was carried out in collaboration with Ulrich Küppers. In total about 1100 measurements were performed at 36 locations at the dome and the valleys mainly affected by the pyroclastic flows of the 1990-1995 eruption (from south to north Akamatsudani Valley, Mizunashi Valley and Oshigadani Valley, including Senbongi Valley). The location of the valleys and the measure points are shown in Figure 2.3.

The observed (bulk) density distribution ranges from 1.33 g/cm^3 to 2.50 g/cm^3 (Fig. 2.4). Here the breadcrust bombs are not included; their bulk density ranges in between 1.01 and 1.67 g/cm^3. This is equivalent to an open porosity of 3 to 39 vol.% without breadcrust bombs and to 55 vol.% including them. Overall, the clasts show a bimodal density distribution with maxima at 2.0 $\pm$ 0.1 g/cm^3 and 2.3 $\pm$ 0.1 g/cm^3. A more detailed description of field work and results is given at *Kueppers et al.* (2005a).

During both field seasons sample clasts with a broad variety in porosity were collected to analyze the fragmentation behavior and elastic wave velocities. The sampling occurred based on the observed density bandwidth within the block-and-ash flow deposits, to ensure best possible coverage of the density/porosity variation. Figure 2.4 shows the observed bulk density distribution. The samples clasts used for fragmentation experiments are marked blue; green represents the clasts used to analyze the elastic wave velocities and orange the samples for fracture toughness tests. Two of the green marked samples are derived from an earlier sampling by Dr. Joachim Gottsmann.

Samples of the pyroclastic flow deposits related to 1997 Vulcanian eruptions of Soufrière Hills Volcano were taken by Dr. Oliver Spieler in August 2002. The samples
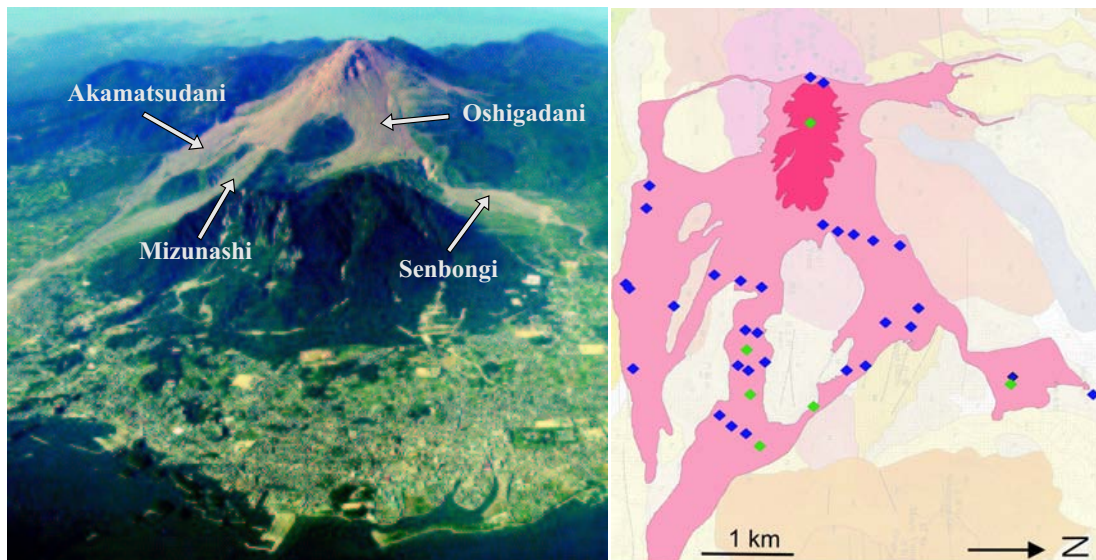
Figure 2.3: Areal view of Unzen Volcano with pyroclastic flow deposits of the 1990-1995 eruption (left). The valleys mainly affected by pyroclasic flows are named in the photograph (*taken on Oct. 13, 1995 by Nagasaki Photo Service*). A modified geological map from *Watanabe and Hoshizumi* (1995) shows the dacitic dome of Unzen (red) and the pyroclastic flow deposits (pink)(right). The blue diamonds mark the locations of density measurements in 2001, the green diamonds the one from the year 2000.

derive from the Belham Valley and buried Plymouth. During that time no field density measurements were possible due to the ongoing eruption of Soufrière Hills Volcano.

Cole et al. (2002) gained field density data of the 1997 deposits. They analyzed the density distribution of about 400 clasts at six locations, two of them at block-and-ash flow deposits and four locations at pumice-and-ash flow deposits. The density of coarse clasts ($>$ 3 cm) of block-and-ash flow deposits ranged from 1.9 to 2.7 g/cm^3. Pumice clasts were rare and were probably accidental, related to earlier Vulcanian explosions. The investigated pumice-and-ash flow deposits typically contained clasts up to 30 cm, ranging in density from 0.8 to 2.0 g/cm^3 (for clasts $>$ 3 cm).

Density measurements on 120 pumice clasts from fallout and pyroclastic flows of the 1997 eruptions were carried out by *Formenti et al.* (2003). They obtained vesicularities ranging from 50 to 80 vol.%, with a mean of 63 $\pm$ 8 vol.%. Pumiceous material (blocks, lapilli and ash) is mentioned to make up over 95 % of the explosion products (Clarke et al. 2002), so that this is representative of most of the magma dis-

charged. Only about 5% of the ejected material was poorly vesicular, as represented by the showers of dense ballistic blocks at the onset of each explosion (*Formenti et al.*, 2003).

2.2.2   Laboratory measurements

A helium pycnometer (Accupyc 1330, Micromeritics) was used in the laboratory to obtain density and porosity values of coplanar cylindrical samples. The pycnometry belongs to the volumetric methods. A sample is placed in a test cell with a defined volume and the samples volume not accessible for helium gas is measured using a gas displacement technique. The pressures observed upon filling the test cell and then discharging it into a second empty cell yield the volume, displaced by the sample. Knowing the weight of the sample, the *matrix density* can be calculated. The *bulk density* is determined from the geometric volume and the weight of the sample. From these two density values, as well as from the geometrical and pycnometrical volume, the *open porosity* of the sample can be calculated. To quantify the *total and closed porosity*, sample material was milled to fine grained powder ($< 63~\mu$m) assuming to crack thereby all closed vesicles. The powder density was also achieved by pycnometric analysis. In combination with the matrix and the bulk density it allowed to determine the closed and the total porosity of the investigated samples.

Random samples from the field density measurement were taken to the laboratory for pycnometer analysis to verify the accuracy of the field measurements. The maximum deviation between field and laboratory bulk density values was found to be $< 5\%$ and proved the (high) precision of the field method (*Kueppers et al.*, 2005a). The matrix density values derived by pycnometry allowed to assign open porosity values to the measured field density distribution.

Cylindrical samples of 25 mm in diameter and 60 mm or smaller in length were drilled out of the field samples. These cylindrical samples were used to analyze the surface area as well as the fragmentation behavior. For all samples the open and closed porosity as well as the density were determined.

Table 2.1a shows the density and porosity of the six clasts of Unzen dacite chosen for investigations on the fragmentation behavior. The open porosity ranges from 6.7 vol.% - 33.8 vol.% without breadcrust bombs and to 52.2 including them. This range
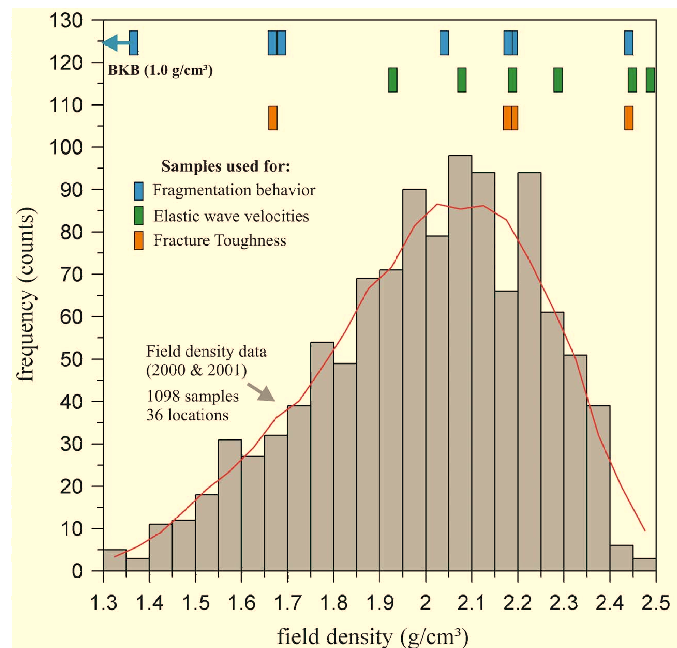
Figure 2.4: Frequency distribution of field density data of the pyroclastic flow deposits at Unzen Volcano. The red line represents the averaged distribution of the field density displayed at the histograms. At top the sample sets used to analyze the fragmentation behavior (blue), the elastic wave velocities (green) and the fracture toughness (orange) are indicated.

covers the porosity variation observed in the field (3.0 vol.% - 55.0 vol.%) very well (Fig. 2.4).

The andesitic samples taken at Montserrat could be classed in four groups, depending on density and texture. The open porosity of this groups ranges from 2.5 vol.% up to 67.1 vol.%. All other density and porosity values are given in Table 2.1b.

The sample size required for the analysis of the elastic wave velocities and the fracture toughness exceeded the dimensions of the testing cell of the helium pycnometer. Therefore a set of cylindrical samples was prepared from the same sample clast as the huge samples and analyzed by helium pycnometry. The total and open porosity of the samples used to determine elastic wave velocities and the fracture toughness was calculated by hand of the pycnometrical results of the cylindrical samples, assuming homogeneous density and porosity for one clast. Table 2.1 shows the density and porosity of the elastic wave velocities samples. The ones used for fracture toughness are not additionally mentioned as their values correspond with the values given for the

same sample clast in Table 2.1a,b.

2.3 Surface area

The surface area of rock samples is an interesting parameter. It is supposed to react much more sensitive to cracks and fractures, as the porosity, especially in the case of moderate to highly porous samples as investigated in this study. Thermal cracking, fragmentation, and secondary mineralization lead to increased values of the surface area. This yields important information on the strength as well as alteration of the natural material and its behavior in a stress field.

2.3.1 Methodology

The surface area was measured with a gas-sorption analyzer (Gemini 2375, Micromeritics). This device allowed to measure cylindrical samples with diameters of up to 26 mm. The surface area of the samples was calculated using the multipoint method of Brunauer-Emmett-Teller (BET) based on gas sorption theory (*Brunauer et al.*, 1938; *Gregg and Sing*, 1982).

The samples were pre-treated by applying a combination of heat (200 °C) and vacuum to remove adsorbed contaminants acquired from atmospheric exposure. The sample is cooled under vacuum to cryogenic temperature. An adsorptive gas is admitted in controlled increments to the sample and a reference tube. The pressure is stepwise increased within a certain relative pressure range with respect to the saturation pressure (p/p_0). Following the gas sorption theory, within a p/p_0 range of about 0.05 - 0.2 a monolayer of gas atoms is formed on the sample surface, above this pressure range multilayer adsorption starts. At each pressure step the quantity of gas adsorbed is calculated. The adsorbed gas volume at these pressure steps defines an adsorption isotherm, from which the quantity of gas forming a monolayer over the surface of the solid phase is determined. The minimum specific surface area that can be measured by this device is 0.01 m^2/g. At least 0.1 m^2 is required to determine total surface areas within an error of $\pm$ 0.03 m^2, but for high-quality measurements a minimum total area of approximately 1 m^2 is necessary.

Traditionally Nitrogen is used as adsorbate gas. Using argon as adsorbate gas can

(a)

sample	bulk density (g/cm³)	std (g/cm³)	matrix density (g/cm³)	std (g/cm³)	powder density (g/cm³)	total porosity (vol.%)	std (vol.%)	open porosity (vol.%)	std (vol.%)	closed porosity (vol.%)	std (vol.%)	closed / open porosity (%)
2001A	2,43	0,044	2,61	0,005	2,62	7,1	1,68	6,7	1,52	0,4	0,17	5,83
2000D	2,20	0,017	2,54	0,008	2,60	15,4	0,67	13,3	0,90	2,1	0,30	15,47
2001C	2,04	0,012	2,57	0,004	2,60	21,6	0,45	20,8	0,45	0,8	0,12	3,85
2000G	1,72	0,115	2,56	0,006	2,62	34,2	4,37	33,0	4,46	1,3	0,23	3,88
2000F	1,67	0,034	2,52	0,007	2,61	35,9	1,30	33,8	1,50	2,1	0,23	6,09
BKB	1,06	0,075	2,22	0,022	2,56	58,5	2,93	52,2	3,67	6,3	0,83	12,16
2000G	without 2 max and 2 min values:											
	1,72	0,072	2,56	0,006	2,62	34,2	2,79	33,0	2,85	1,3	0,23	3,88

(b)

sample	bulk density (g/cm³)	std (g/cm³)	matrix density (g/cm³)	std (g/cm³)	powder density (g/cm³)	total porosity (vol.%)	std (vol.%)	open porosity (vol.%)	std (vol.%)	closed porosity (vol.%)	std (vol.%)	closed / open porosity (%)
really dense	2,63	0,006	2,70	0,004	2,73	3,5	0,21	2,5	0,18	1,0	0,14	38,65
mid dense	2,16	0,020	2,68	0,065	2,71	20,3	0,73	19,4	2,04	0,9	1,97	4,75
stripy	1,38	0,088	2,46	0,079	2,69	48,6	3,29	43,9	2,33	4,7	1,58	10,69
pumice	0,70	0,015	2,15	0,055	2,69	73,8	0,56	67,1	0,84	6,7	0,81	9,93

(c)

sample	bulk density (g/cm³)	matrix density (g/cm³)	powder density (g/cm³)	total porosity (vol.%)	open porosity (vol.%)	closed porosity (vol.%)	closed / open porosity (%)
15.9.91-b	1,93	2,54	2,60	25,9	24,3	1,6	6,7
MUZ 2000B	2,08	2,55	2,60	19,9	18,2	1,7	9,5
MUZ 2000E	2,18	2,55	2,60	16,3	14,5	1,8	12,5
MUZ 2000C	2,29	2,55	2,59	11,5	10,2	1,2	12,2
Ensp-2	2,45	2,60	2,61	6,3	6,1	0,2	3,6
2000A	2,50	2,59	2,60	3,7	3,3	0,4	11,2

Table 2.1: Overview of the density and porosity including the standard deviation (std) of all sample clasts or groups used for experiments. (a) sample clasts of Unzen dacite used for fragmentation experiments. (b) sample groups of Montserrat andesite used for fragmentation experiments. (c) Samples of Unzen dacite used to analyze elastic wave velocities. *(Note: For the values at Table (c) no standard deviation is given, as only one sample each was analyzed.)*

improve the sensitivity by a factor of four, as its atomic cross-section is smaller than the molecular cross-section of N_2. This is relevant in cases where the specific surface area is low (< 2 m^2/g). As the samples analyzed in this study range at the lower part of the measurability range of the Gemini device, or marginally below, the adsorptive gas was changed to Argon. The boiling point of Argon accords approximately the one of Nitrogen (N_2: 77.35 K, Ar: 87.35 K) and therefore fluid Nitrogen can be used as coolant. This only affects the saturation pressure of Argon and had to be taken into account for the applied pressure range.

2.3.2   Results

The surface area of 65 samples from Unzen and 20 samples from Montserrat was analyzed, covering the entire porosity range observed for these sample sets (Tab. 2.1). The measurements were performed on cylindrical samples with a diameter of 25 - 26 mm and a maximum length of 40 mm. The length of the samples was restricted by the position of the samples in the dewar containing the liquid nitrogen. At samples longer than 40 mm the thermal equilibrium over the sample could not be assured for the entire experimental run.

Unzen Volcano, Japan

The specific surface area of the investigated Unzen samples range from 0.03 m^2/g to up to 0.08 m^2/g, or 0.10 m^2/g including the bread-crust bombs (Fig. 2.5). Multiplied with the sample weight this value yields the total surface area of the sample. The specific surface area increases almost linear with the open porosity. Some samples, especially breadcrust bombs but also a very dense and some highly porous ones, showed elevated surface areas compared to the main trend. These samples are marked green in Figure 2.5. Samples with these exceptional surface areas as well as some samples fitting to the common trend were heat-treated: They were heated with a rate of 2.5 °C per minute up to 850 °C kept there for one hour, and then allowed to cool slowly (approximately at 2 °C/min). Then they were measured again. The specific surface area of the "regular" samples stayed constant or dropped slightly, whereas the values for the "elevated"
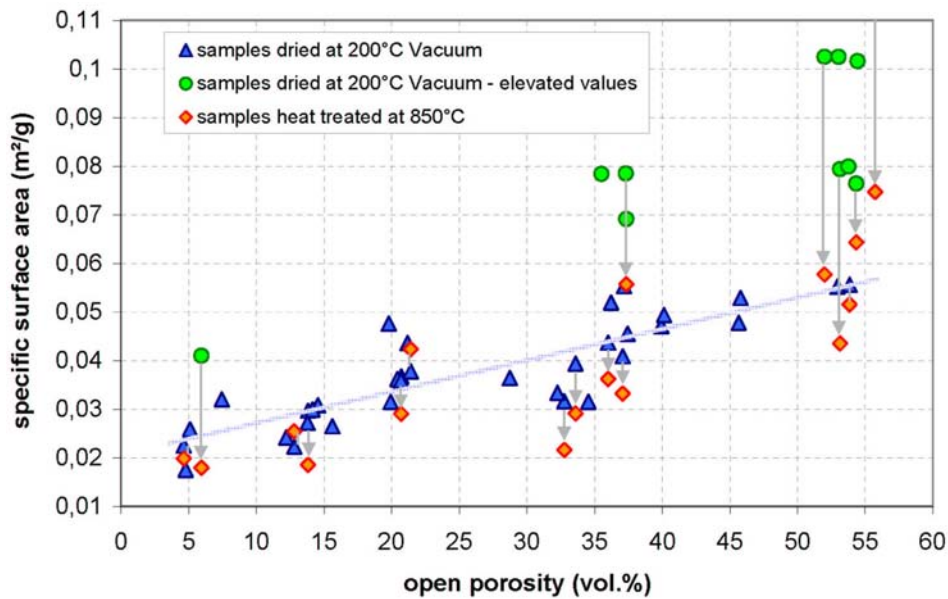
Figure 2.5: Specific surface area of samples from Unzen Volcano. The specific surface area seems to be largely dependent on the porosity of the samples. Some samples show significantly elevated values compared to the common trend. Heat-treatment of these samples resulted in a pronounced surface area decrease and a general trend slightly below the common trend of non treated samples. The elevated surface areas may be caused by secondary mineralization.

samples decreased significantly. All values gained for heat-treated samples are marked orange in Figure 2.5. Again a linear increase of the specific surface area with increasing open porosity could be observed, slightly lowered compared to the trend found at the non heat-treated samples. Thus it can be concluded that secondary mineralization (e.g. zeolites) or presence of microcracks (due to cooling tensions gained during eruptive emplacement) most possibly caused the elevated values of the specific surface of samples. A possible microporosity, e.g. in breadcrust bombs, can be considered to bear only minor influence, as this should result in temperature independent shifts of the specific surface area.

For comparison, analysis of the fine fraction ($< 250\ \mu$m) of fragmented samples revealed specific surface areas around 0.16 m^2/g and higher (*Kueppers et al.*, 2005b).
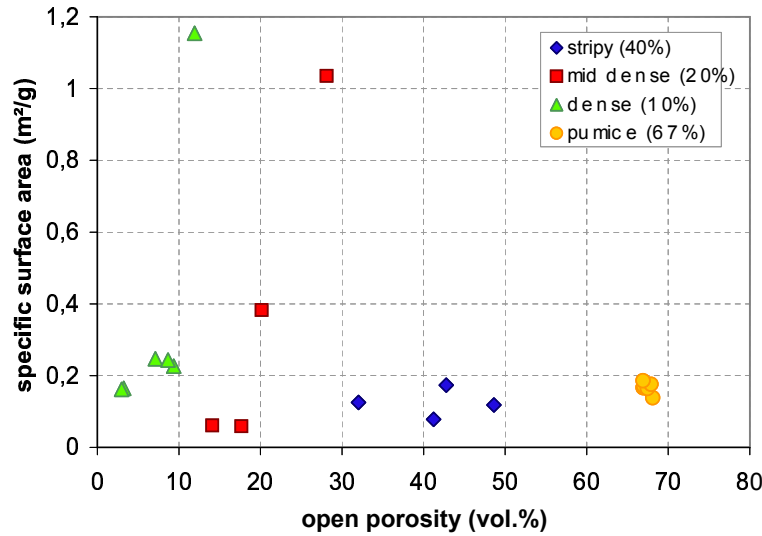
Figure 2.6: Specific surface area of samples from Soufrière Hills Volcano, Montserrat. The specific surface area seems to be largely independent of the porosity of the samples. Two extremely high values could be observed. They result most probably from a high microvesicularity.

Soufrière Hills Volcano, Montserrat

The investigated samples of Montserrat show a slightly different behavior. In contradiction to the results obtained for the Unzen samples, the specific surface area seems to be more or less independent of the open porosity of the samples. The specific surface area over the analyzed porosity range was determined to be between 0.05 and 0.23 m^2/g. Nevertheless three outliers leading to specific surface values of 0.38 m^2/g, 1.04 m^2/g and 1.15 m^2/g could be observed and proved in additional measurements (Fig. 2.6). These extremely high values can be most probably explained by a high microporosity of the samples. The used gas-sorption analyzer allows to investigate the microporosity of samples following the method of Barrett, Joyner and Halenda (BJH). This method uses a model of pore filling with condensed adsorptive gas at higher values of p/p$_0$, where multilayer adsorption starts (*Gregg and Sing*, 1982). At all three samples bearing extremely elevated surface areas, a microporosity could be detected.

The investigation of ash samples derived from explosive eruption of Montserrat yielded specific surface areas of 0.81 m^2/g and even 3.32 m^2/g at an ash sample containing respirable particles (< 5 μm).

2.4   Fracture toughness

The fracture toughness is a material property of rocks describing its resistance to tensile failure. The fracture toughness has been extensively investigated in materials science in order to study stress response in metals, ceramics or concrete. Measurements of fracture toughness on volcanic rocks remain relatively unexplored, especially under simulated volcanic conditions. Significant contributions to the experimental study of fracture toughness at high-temperature were made by *Meredith and Atkinson* (1985), who measured the fracture toughness of quartz, black gabbro and Westerly granite over the temperature range of 20 - 400 °C, and *Balme et al.* (2004), who analyzed the fracture toughness of mainly basaltic samples at temperatures of up to 750 °C and confining pressures of up to 30 MPa.

2.4.1   Methodology

Fracture toughness tests were conducted at the Mineral Rock & Ice Physics Laboratory at the University College London in collaboration with Prof. P. Sammonds and V. Rocchi. The tests were performed using the short rod (SR) specimen with standard core sample configuration according to the suggestions of the International Society of Rock Mechanics (*ISRM*, 1988; *Ouchterlony*, 1989). The sample diameter was 60 mm, all other dimensions are given in relation to the diameter by ISRM, the sample length for instance needed to be 87 mm. The standard sample configuration is shown in the left sketch of Figure 2.7. At the SR setup the opening tensile force must be applied perpendicular to the core axis of the sample. Therefor the chevron-notched specimen was located over two machined knife edges at top of a split cylindrical housing, which is forced apart by an internal hydraulic actuator. The transverse movement of the knife edges is measured by a displacement transducer. A detailed description of the test apparatus is given by *Balme et al.* (2004). All experiments were carried out at temperatures $\approx$ 500 °C and ambient pressure.

The apparatus allowed level I and level II fracture toughness tests. Level I tests only require the applied force at failure to be measured, whilst crack mouth opening displacement (CMOD) must be monitored (at least in the differential sense) for level II tests in order to correct for the specimen size "plasticity" variations (*ISRM*, 1988). To achieve level II values repeated loading / unloading cycles before and after the crack
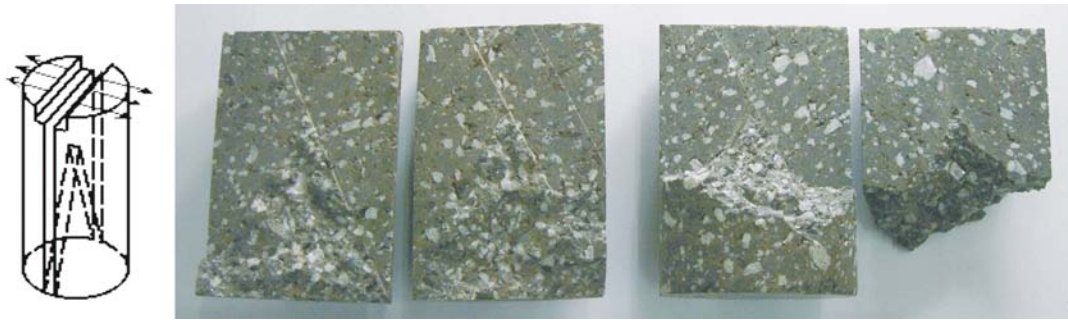
Figure 2.7: The standard core sample configuration for short rod fracture toughness tests suggested by the ISRM (left) and two samples used for fracture toughness tests at the Mineral Rock & Ice Physics Laboratory at the UCL. The sample diameter is 60 mm. The left sample is broken as expected, the right sample failed along a transverse plain. The transverse failure happens often in coarse grained rocks.

initiation have to be performed.

2.4.2   Results

The measurements were conducted at three sample sets of Unzen dacite containing an open porosity of 6.7 %, 13.0 % and 33.8 %, respectively. For each set three samples were prepared. Figure 2.7 shows two samples broken during fracture toughness tests. At the left one the fracture pathway runs in the expected manner. If the maximum load at which the fracturing occurred permitted several loading / unloading cycles before complete failure of the sample, level II fracture toughness values can be calculated. At the right sample, the rock failure occurred along a transverse plain. In this case the fracture path seemed to follow a weakening zone within the sample, as it might be for instance represented by old, preexisting cracks or locally restricted porous areas. For most of the samples following this fracture behavior, level I fracture toughness values can be calculated.

The majority of the fracture toughness tests on Unzen samples seemed to fail along a transverse plane. This fracture behavior is quite common in coarse grained rocks and sedimentary rocks (*pers. com. Phil Meredith*). In the case of the Unzen dacite it may be caused by the large phenocryst fraction eventually in combination with preexisting (cooling) cracks. Therefore only level I fracture toughness values could be calculated
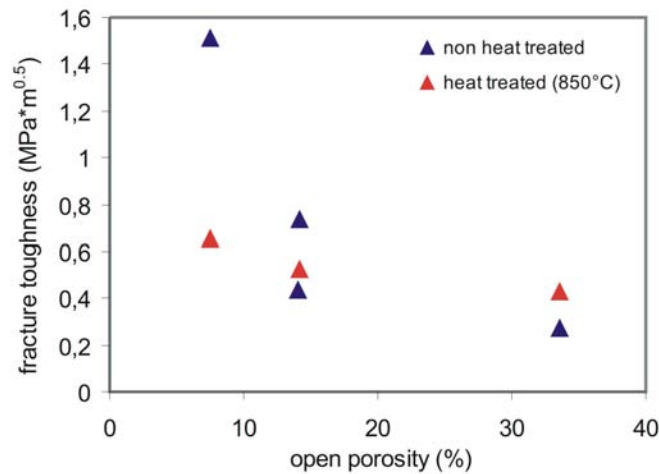
Figure 2.8: Results of the level I fracture toughness tests on Unzen dacites, carried out at the UCL in collaboration with Prof. Sammonds. The tests were conducted at about 500 °C. A heat-treatment of the sample before the test seemed to lower the fracture toughness.

from the achieved failure load following the equation:

$$K_{I\_SR} = 24 \cdot \frac{F_{max}}{\sqrt[3]{D}}$$

with K_{I_SR} being the fracture toughness derived by the short rod setup (SR) and F_{max} being the failure load.

A much higher number of tests would have to be performed in order to get more reliable values from level II tests, as the failure load is very low and many samples tend to fail along transverse plains. Nevertheless, the obtained level I values can be taken as a lower boundary for the fracture toughness of the Unzen dacite. They range between 0.3 - 1.5 $MPa\sqrt{m}$ (Fig. 2.8). For comparison, Etna crust yielded fracture toughness values of $\sim 1.3\ MPa\sqrt{m}$ and Icelandic basalts 2.2 - 3.8 $MPa\sqrt{m}$ (*Balme et al.*, 2004).

Some samples have undergone a heat-treatment before the FT tests. The samples were heated with a heating rate of 5 °C/min to 850 °C, kept there for one hour and than cooled down with approximately the sample rate of 5 °C/min. This procedure was meant to thermally relax the samples by reducing cooling tensions and thereby induced cracks. These samples showed lower or about the same fracture toughness values than the non-treated samples (Fig. 2.8).

One might expect a relation between the fracture toughness, which is controlling the opening mode, and the tensile strength of a rock, in which the rock fails in tension. *Zhang* (2002) analyzed the fracture toughness and the tensile strength over a broad variety of rock types (e.g. basalt, granites, sandstones, limestone, tuff and marble) and even different testing methods. He obtained an empirical relationship between the fracture toughness K_I, gained for mode I (tensile) fracturing, and the tensile strength σ_t of rock following the equation:

$$\sigma_t = 6.88 \cdot K_I$$

With this relation the tensile strength of the Unzen dacite can be estimated. The values acquired range between 1.9 - 5.1 MPa, one low porous sample yields 10.4 MPa.

Jaeger and Cook (1979) pointed out that the (uniaxial) compressive strength of a rock is usually 8 - 15 times greater than its (uniaxial) tensile strength. *Brook* (1993) showed that a generally recognized ratio of compressive / tensile strength is 10 / 1. This allows also a rough estimation of the compressive strength of the Unzen dacite.

Chapter 3

Elastic wave velocities

Numerous laboratory measurements have been performed to determine the pressure dependence of ultrasonic wave velocities in rocks (*Christensen*, 1982; *Gebrande*, 1982). However, experiments focussing on the temperature dependence of ultrasonic wave velocities in rocks are rare. The small volcanic rock contribution to this inherently sparse dataset consists mostly of measurements on basalts (*Kern*, 1982a). Significantly, no measurements have yet been performed on silica-rich volcanic rocks, even though knowledge of seismic energy propagation trough silicic volcanoes is of paramount importance for hazard mitigation (*Chouet*, 1996; *Neuberg*, 2000); particularly because many explosive volcanoes are fed by silica-rich magma (e.g. Mount St. Helen's (USA), Rabaul (Papua New Guinea), Unzen (Japan), Montserrat (West Indies)). As volcanic rocks have undergone a significant thermal shock and decompression upon eruption, the reconstitution of their original in-situ properties requires measurements under relevant pressure and temperature conditions.

Seismic velocities of silica-rich rocks measured under realistic conditions are required for numerical modelling of conduit processes and seismic wave propagation (*Jousset et al.*, 2003; *Neuberg et al.*, 2000; *Sturton and Neuberg*, 2003). Estimates of P- and S-wave velocities of silicic magma are further required to ameliorate the knowledge of the structure of many active volcanoes (as Rabaul, Taupo Volcanic Zone, Nevado del Ruiz) derived e.g. by seismic tomography and the velocity structure (*Finlayson et al.*, 2003; *Londono and Sudo*, 2003). The velocity model of Unzen Volcano was acquired during the "1995 Unzen seismic experiment"and consists of approximately 2 km wide cubic blocks (*Ohmi and Lees*, 1995). This velocity model is very

large scaled and can therefore only be used as a first order assumption to model processes such as those inside the conduit.

3.1   Sample description

Six dacitic samples from Unzen Volcano, Japan, were investigated. They were collected from the block-and-ash flow deposits down the Mizunashi valley as well as from the dome. The clasts for this analyses were chosen to be as representative as possible, in terms of density and homogeneity/heterogeneity of the eruption products of Unzen Volcano. For the experiments cube-shaped specimens with 43 mm edge lengths were cut from these clasts. The orientation of the cube axes followed visible mesoscopic fabric coordinates where possible: X and Y are within the plane of magmatic layering (magma flow), X is parallel to a shape preferred crystal orientation, if present, and Z is normal to the layering.

Densities were calculated from mass and dimensions of the cubic specimen, the porosities being derived by Helium pycnometric analysis. As the cubic specimen exceeded the chamber dimensions of the pycnometer, the analyses were performed on cylindrical samples prepared from the same big clasts as the cubic samples. The bulk densities of these cylindrical samples are in good agreement with the densities of the cubic samples. The determined density values range of 1.93 - 2.50 g/cm^3 corresponding to a open porosity range of 3.3 - 24.3 vol.%. This covers the density range from the most abundant to the maximum density observed for the block-and-ash flow deposits (Fig. 2.4). A sample with a density of 1.67 g/cm^3 (34 % porosity) collapsed during pressurization.

3.2   Methodology

The elastic P- and S-wave velocities and velocity anisotropies of the Unzen dacites were determined experimentally in collaboration with Prof. H. Kern (Christian-Albrechts-Universität Kiel). The measurements were conducted on cube-shaped specimens in a true triaxial multi-anvil press using the ultrasonic pulse-transmission technique (Fig. 3.1). A state of nearly hydrostatic stress was achieved by pressing six
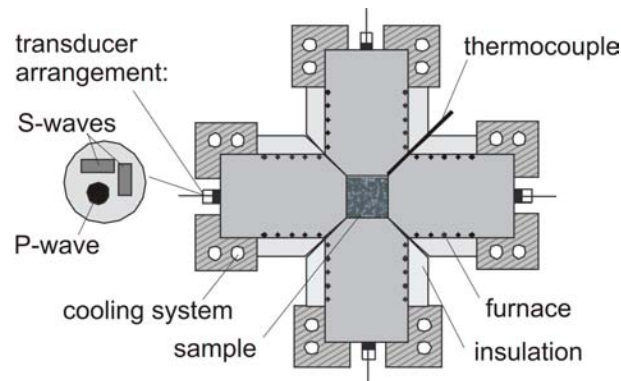
Figure 3.1: Schematic draw of the triaxial multi-anvil press used to measure the elastic P- and S-wave velocities. The measurements were performed up to 100 MPa pressure and 600 °C temperature. The experiments were carried out in collaboration with Prof H. Kern at the petrophysical laboratory at the University Kiel, Germany.

pyramidal pistons onto the sample cubes. The special arrangement of the sample-piston-transducer assembly allows simultaneous measurements of compressional (P) and orthogonally polarized shear wave velocities (S1, S2). The end of each piston next to the specimen is surrounded by a furnace and heat is transmitted from the pistons to the specimen, allowing homogenous heating and temperature distribution within the large volume specimens, as has been confirmed by temperature measurements at different places within a test sample (*Kern and Fakhimi*, 1975). Temperature is measured using thermocouples placed in a cavity at the end of each piston very close ($\sim$ 1mm) to the specimen. The transducers (2 MHz and 1 MHz) are placed on the low-temperature side of each piston, and the travel time of the pulses through the specimen is obtained by subtracting the calibrated time needed for the pulse to travel to and from the specimen through the pistons from the total time measured by the transducers. Length and resulting volume changes of the sample cubes, due to changes of principal stress and temperature, are obtained by the piston displacement. The cumulative error in Vp and Vs is estimated to be around 1 % (*Kern*, 1982b; *Kern et al.*, 1997).

3.3 Results

P- and S-wave velocities were measured simultaneously in the three structural directions. Measurements were performed first at room temperature up to 100 MPa, fol-

lowed by measurements at the constant confining pressure of 100 MPa over the temperature range 20 - 600 °C. The temperature was increased in steps of about 80 - 100 °C over 30 minutes periods. To ensure that the samples had reached temperature equilibrium, successive readings were taken at time intervals of at least 40 minutes.

3.3.1   Pressure effect

The investigated pressure range corresponds to in situ pressures from the surface to about 4000 m depth inside a volcanic complex, which is the depth range of interest for most volcano-seismic activity (*Chouet et al.*, 1997; *Hidayat et al.*, 2000; *Neuberg*, 2000; *Umakoshi et al.*, 2001). Typical slopes are shown in Figure 3.2 for sample MUZ 2000 A. P- and S- wave velocities increase slightly and non-linearly with increasing pressure with the highest change at the beginning of pressurization. The Vp values in the three orthogonal directions of sample MUZ 2000 A (Fig. 3.2a) increase from 4.15 - 4.87 km/s at ambient pressure to 5.11 - 5.48 km/s at 100 MPa. The velocity anisotropy, calculated as

$$A = \frac{Vmin + Vmax}{Vmean}$$

shows an inverse behavior. It decreases towards higher pressures from 15.6 % down to 6.9 %. The general velocity increase as well as the decrease of the velocity anisotropy at increasing pressure holds for all investigated samples. The mean P-wave velocities of all samples increase from 3.87 - 4.60 km/s at 25 MPa to 4.21 - 5.35 km/s at 100 MPa. *Birch* (1960) determined compressional wave velocities of a broad variety of rocks within a pressure range of 1 - 1000 MPa and observed a similar change of the elastic properties with pressure. He obtained the strongest velocity increase in the pressure range from ambient pressure to 100 - 200 MPa, and then a more gradual increase at higher pressures, sometimes reaching a constant value. *Birch* (1960, 1961) and others (*Brace*, 1965; *Kern and Fakhimi*, 1975) related this effect to a compaction of the sample due to closure of microcracks.

The shear wave velocities show a similar trend. The velocity difference of the orthogonal polarized shear waves propagating in the three directions X, Y, Z differs only slightly by a few percent. Therefore, a velocity Vs* is introduced as the mean of the two S-wave velocities measured in each direction. Figure 3.2b shows the pressure dependence of Vs* for the sample MUZ 2000 A. The Vs* values for the three directions

Figure 3.2: Elastic wave velocities as a function of pressure for the sample MUZ 2000 A. The measurements were carried out at room temperature. (a) The compressional wave velocities (Vp) increase slightly with increasing pressure, whereas the anisotropy (A) decreases. (b) The averaged shear wave velocities (Vs*) rise slightly with increasing pressure.

of this sample increase from 2.64 - 2.90 km/s at 25 MPa to 3.13 - 3.19 km/s at 100 MPa. The corresponding values of Vs* for all samples vary between 1.81 km/s and 2.90 km/s at 25 MPa and between 2.02 km/s and 3.17 km/s at 100 MPa. The general increase of P- and S-wave velocities with increasing pressure is basically the result of the sample compaction, as is confirmed by the volumetric strain vs. pressure (Fig. 3.5a) and density vs. pressure curves (Fig. 3.5c).

3.3.2 Temperature effect

The measurements were carried out at a constant pressure of 100 MPa, which was needed as contact pressure to ensure best signal transmission through the sample. Figure 3.3a shows the change of the P-wave velocities and the Vp anisotropy of the sample MUZ 2000 A as a function of temperature at 100 MPa. Surprisingly, the velocities measured in the three directions increase slightly with rising temperature from 5.11 - 5.48 km/s at room temperature to 5.51 - 5.73 km/s at 600 °C, resulting in an increase of the average velocities from 5.38 km/s to 5.64 km/s at 600 °C. Coevally, anisotropy decreases from 6.88 % to 3.92 %. Concordant to the behavior at rising pressure, a notable reduction of the P-wave velocity in the Z - direction was observed at starting
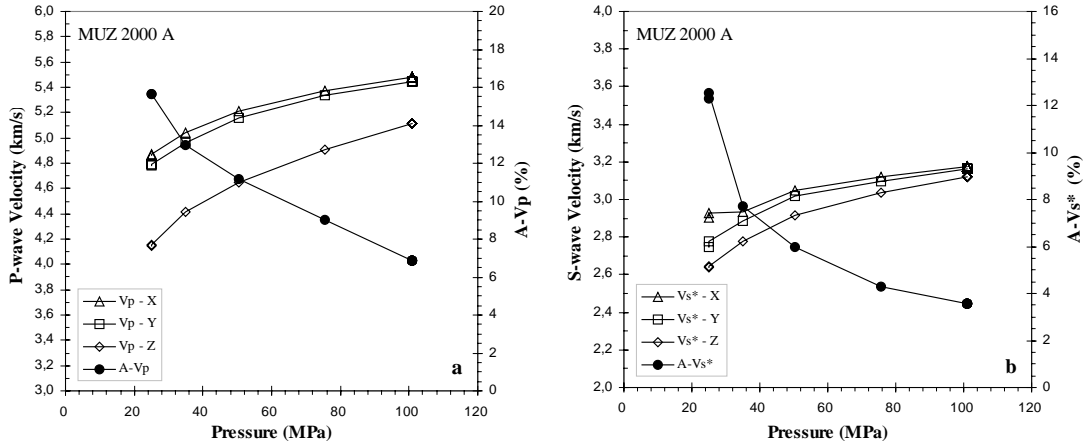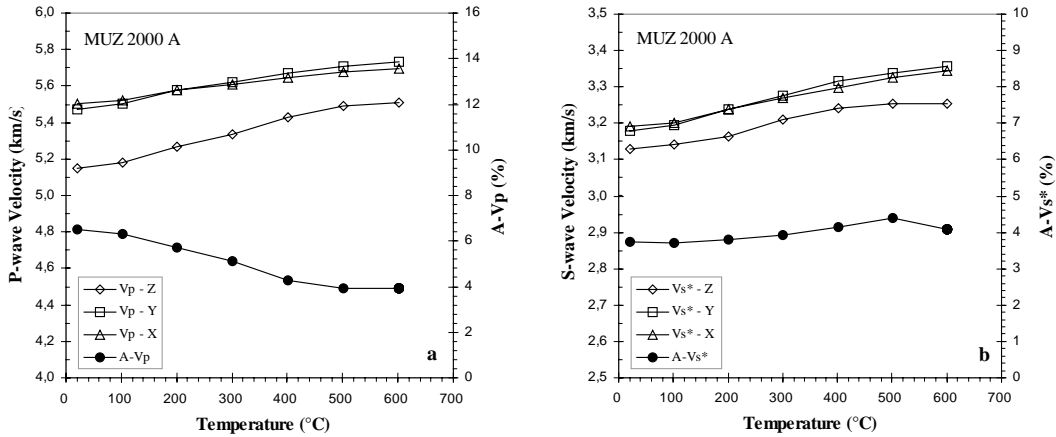
Figure 3.3: Elastic wave velocities as a function of temperature for the sample MUZ 2000 A. The measurements were carried out at 100 MPa pressure. (a) The compressional wave velocities (Vp) increase slightly with increasing temperature, whereas the anisotropy (A) decreases. (b) The averaged shear wave velocities (Vs*) rise slightly with increasing temperature.

conditions (100 MPa, 20 °C). With rising temperature, the increase of P-wave velocity is more pronounced in the Z - direction than in the X and Y directions. The velocities converge and so the Vp anisotropy declines (Fig. 3.3a).

A similar behavior at increasing temperature was observed on all other samples. The mean P-wave velocities for all measured samples rose from 4.21 - 5.35 km/s at room temperature up to 4.31 - 5.64 km/s at 600 °C (Fig. 3.4 and Table B.1). A lower velocity in one orthogonal direction was clearly observed in most of the analyzed samples. As expected, the velocities increased with the density of the analyzed samples.

The S-wave velocities show a similar trend. Figure 3.3b shows the Vs* velocities of the sample MUZ 2000 A as function of temperature. All three Vs* velocities increased from 3.12 - 3.17 km/s at room temperature to 3.25 - 3.36 km/s at 600 °C. A lowered Vs* value could be detected in the Z - direction, leading to a Vs* anisotropy of 3.55 %, which remained nearly constant over the entire temperature interval.

At most of the samples the mean elastic wave velocities rose slightly with increasing temperature (Fig. 3.4b). The Vs* values of all samples analyzed in this study, range from 2.02 - 3.17 km/s at room temperature to 2.03 - 3.36 km/s at 600 °C, all these values are given for the contact pressure of 100 MPa. From Figure 3.4a a clear relationship between velocity and density is apparent: the higher the density, the higher
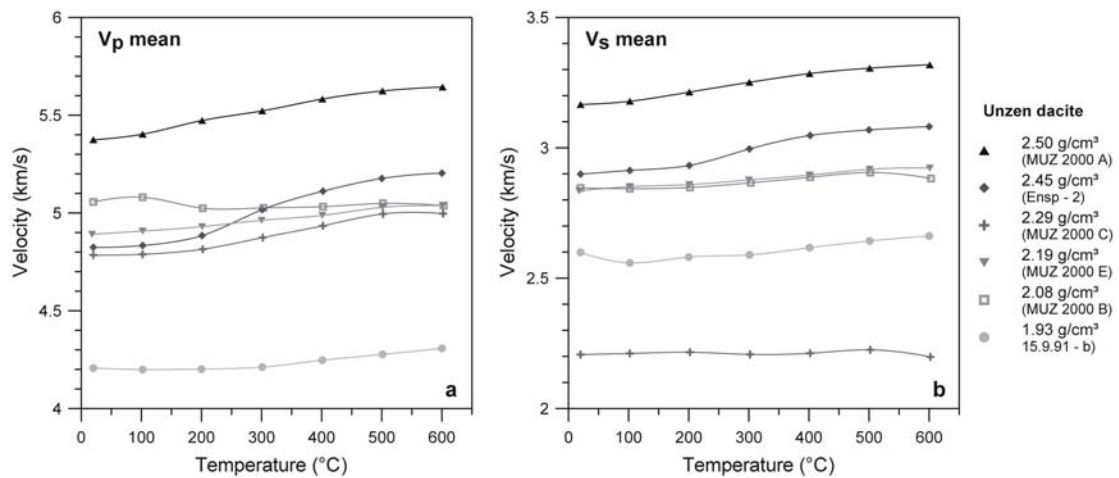
Figure 3.4: Overview of all obtained mean Vp and Vs* values as a function of temperature. The measurements were conducted at a contact pressure of 100 MPa. (a) The mean Vp values increase towards higher temperatures, an exception is the sample MUZ 2000 B, where the velocity decreases between 100 °C and 200 °C and than stays constant. (b) The values for the mean Vs* increase slightly with increasing temperature. The sample MUZ 2000 C is an exception; the velocity stays more or less constant at a remarkably low value.

the P- and S*-wave velocities. Interestingly, the unusual velocity increase with increasing temperature is most pronounced in the samples with the highest velocities (lowest porosities), presumably as a result of further closure of microcracks.

The temperature-induced increase of P- and S-wave is in sharp contrast to the "classical" velocity-temperature relationship observed in many igneous and metamorphic rocks (e.g. *Kern and Tubia*, 1993; *Kern*, 1993; *Mueller and Raab*, 1997). The same holds with respect to the relationships between volumetric strain vs. temperature (Fig. 3.5b) and density vs. temperature (Fig. 3.5d). At the constant confining pressure of 100 MPa the bulk volume increases in all samples with increasing temperature and coevally the density decreases slightly.
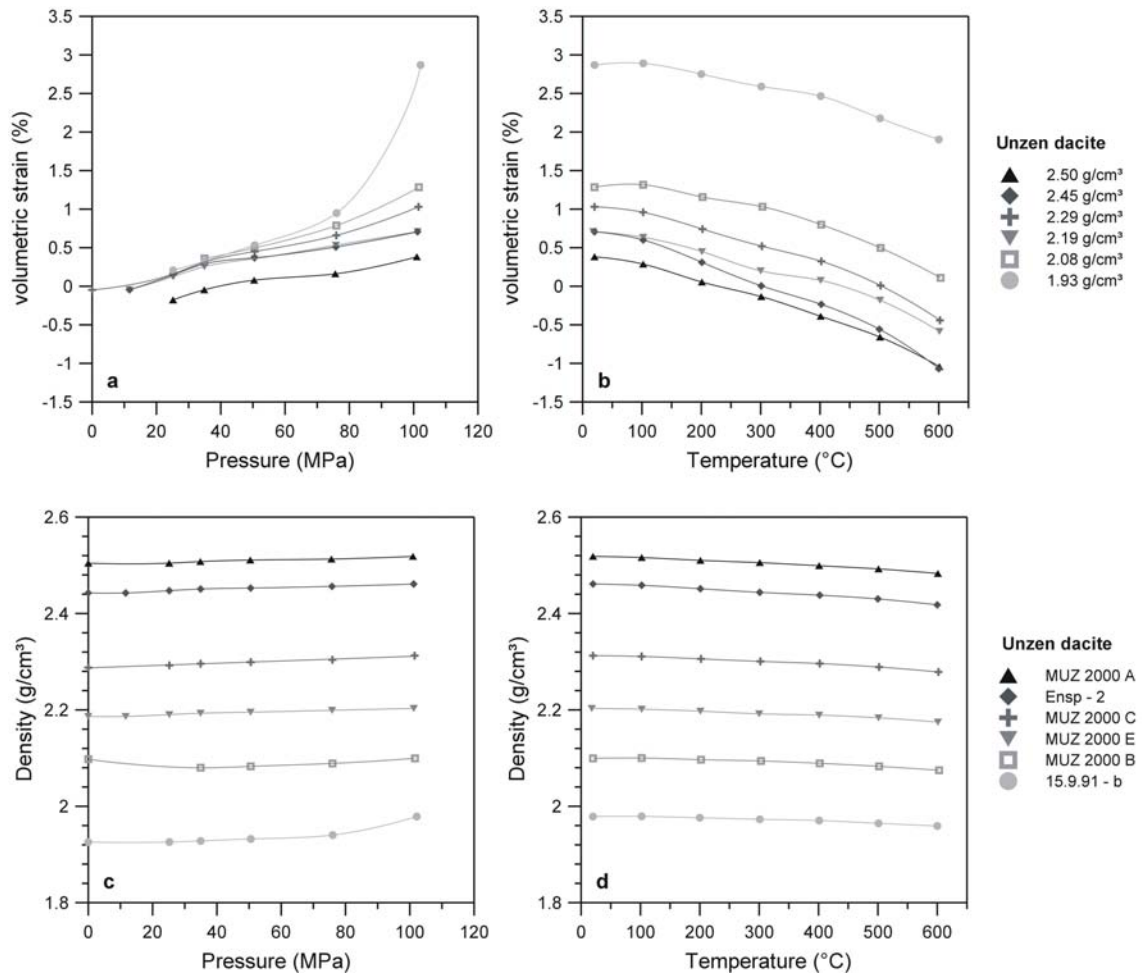
Figure 3.5: Length changes and resulting volume changes of the sample cubes, due to changes of principal stress and temperature, are obtained by the piston displacement. Bulk density changes are calculated with the changed volume. Diagrams (a, c) show the volumetric strain and bulk density as a function of pressure. Diagrams (b, d) show the influence of temperature at 100 MPa confining pressure on the volumetric strain and bulk density.

3.4 Discussion

A close relationship between density, porosity and elastic wave velocities could be ob-
served in the investigated samples; a similar relationship between velocity anisotropy,
density and porosity, however, was not observed. This may be explained by the rela-
tively homogeneous and only poorly aligned pore distribution with poorly elongated
vesicles. In the dense samples, vesicles are often attached to phenocrysts, and there-
fore also slightly aligned (Fig. 2.1a and Fig. A.2). The vesicles apparently formed at
the pressure shadow behind the crystals (Fig. 3.6a). Hereby the vesicles may enhance
the anisotropy caused by crystal alignment, but as the total porosity is only in the order
of 3.7 - 6.3 vol.%, this effect may be of minor importance. Samples with a higher total
porosity (11.5 - 25.9 vol.%) often contain large fringed, collapsed vesicles (Fig. 2.1c,
Fig. 3.6b).

The results of this study show that for Unzen dacites a temperature increase leads
to higher elastic wave velocities and lower velocity anisotropies. As mentioned above,
the opposite behavior is documented for the majority of rocks. The velocity drop
with increasing temperature is usually explained by the creation of microcracks during
heating (*Kern*, 1982a). For this study the opposite can be stated. Presently, the reason
for the unusual increase in P- and S-wave velocities with increasing temperature is
not fully understood. Thermal expansion of the matrix minerals of the rock into the
open pore space may probably reduce the pore volume. In addition, the relaxation of
samples may lead to closing of microcracks, removing tensions and cracks acquired
during fast cooling of the erupted rocks. The presence of a glassy groundmass may
also be important, as the seismic velocities in glass tend to increase with temperature
(*Hughes and Jones*, 1950).

Velocity anisotropy can be linked to sample texture: Samples with a high anisotropy,
such as MUZ 2000 C and MUZ 2000 B (Table B.1) show a pronounced shape preferred
orientation of phenocrysts and microcrystals. On these samples, an additional layer-
ing of two groundmass phases parallel to this orientation may enhance the anisotropy.
Figure 3.6c shows a contact of these two groundmass layers, with subtle difference
in color and crystal alignment. Generally, the crystals were probably aligned parallel
to the conduit walls during shallow ascent. Cracks inside the samples, which may be
caused by cooling tensions, tend to be oriented roughly parallel to the phenocrysts. The
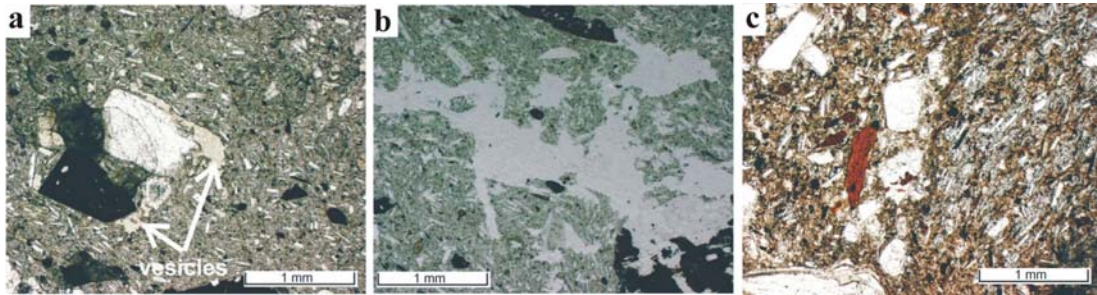
Figure 3.6: Thin section images showing vesicles and groundmass of analyzed samples of Unzen dacite. (a) Small vesicles are attached to crystals in the pressure shadow of phenocrysts. (b) Fringed vesicle behind a large hornblende crystal (only partially to be seen at the lower bottom). This vesicles form is often observed in higher porous samples. (c) Contact of two groundmass layers. The right layer shows greater crystal alignment than the left layer (sample MUZ 2000 C).

seismic velocities measured normal to this orientation (usually in the Z-direction) are therefore significantly lower than the seismic velocities within the orientation plane. It can be postulated that the Vp anisotropy decreases with increasing temperature caused by further closing of microcracks. Due to preferred crack orientations, the velocity increase in one direction (usually the Z-direction) is more pronounced than in the remaining two directions (Fig. 3.4, Table B.1).

A comparison with the results of the "1995 Unzen seismic experiment" (*Ohmi and Lees*, 1995) shows quite good agreement, even though their velocities are somewhat high. For the layer between surface and 2.5 km they obtain P-wave velocities of 5.44 - 5.76 km/s and mean S-wave velocities of 3.09 - 3.30 km/s.

Regarding the maximum temperature in experiments performed in this study, it would be desirable to investigate highly crystalline rocks e.g. at about 800 - 850 °C for dacitic composition. However, in the cubic-anvil press the maximum temperature is limited to about 600 - 700 °C. Very few values of elastic wave velocities at a higher temperature (up to 1000 °C) have been published to date (*Lebedev and Zharikov*, 2000; *Mueller and Raab*, 1997). These studies used an internally heated gas pressure apparatus, with limited sizes of the cylindrical samples: approximately 5 mm in length and 8 mm in diameter (*Lebedev and Zharikov*, 2000), and 25 mm in length and 13 mm in diameter, respectively (*Mueller and Raab*, 1997). Unfortunately, devices that allow measurements at melting temperatures on large-volume samples, to analyze for exam-

ple porphyritic rocks containing phenocrysts of around 5 mm length, as the dacite in this study, are not available. Although the data acquired in this study are of restricted use for relying on the magma properties inside the conduit itself, they are highly relevant for processes within or near the conduit walls, where temperatures should be lower and the magma already solidified.

3.5 Implications

In a mafic volcanic system the conduit seems to be well defined with sharp boundaries (conduit walls), clearly detectible by deformation field measurements (*Cayol and Cornet*, 1997, 1998). Felsic magma has lower temperatures and higher viscosities than mafic magma. Within felsic volcanic systems, the conduit boundaries cannot be easily detected by the deformation field methods, suggesting a diffuse transition from the conduit to the host rock (*Cayol et al.* 2004; *pers. com. Cayol and Tuffen*). *Jousset et al.* (2003) also use a transition zone for the modelling of low-frequency volcanic earthquakes to account for the gradients in the physical properties between the viscous magma in the conduit and the solid host rock. These changes in the physical properties influence the wave propagation through the conduit as well as the behavior of waves generated inside the conduit, and need therefore a particular consideration. The results of this study help to quantify these properties. Indeed, recent work has shown that a temperature gradient across silicic conduits may influence the flow regime and generation of seismic events (*Polacci et al.*, 2001; *Tuffen et al.*, 2003; *Neuberg et al.*, 2005).

In particular, the temperature effect (increasing seismic velocities towards higher temperature) has to be taken into account, as it may lead to a high velocity zone at the hot, but solidified conduit walls. As a result of the property changes, *Jousset et al.* (2003) obtained guided or trapped waves within the transition zone, a high velocity region may enforce this effect. Trapped waves are also a common phenomenon in fault zone regimes (*Li and Leary*, 1990; *Li and Vernon*, 2001). In this case, a velocity reduction caused by the ground weakening (fracturing) yields to a strong diffraction and finally trapping of the seismic waves inside a fault zone layer (*Ben-Zion*, 1998; *Jahnke et al.*, 2002).

The host rock close to the conduit is fractured during the emplacement of a fresh magma body (*Kilburn*, 2003). Therefore the fractures should show a preferred orientation, yielding a velocity anisotropy. The alignment of the crystals in the magma further increases the anisotropy, as the seismic velocities normal to their orientation will be reduced. Internal shearing during the magma ascent may additionally lead to a layering parallel to the conduit wall, amplifying the velocity anisotropy. A consideration of the anisotropic character of the seismic velocities, as analyzed in this study for the Unzen dacite, should considerably improve the existing models.

The data gained in this study are therefore crucial for fine adjustment of existing models as well as future seismic models of volcanic complexes in general and conduits in particular.

Chapter 4

Fragmentation behavior

The dynamics of the fragmentation of magma exerts a strong influence on the explosive behavior and thus the eruptive style of a volcano (*Dingwell*, 1996). The fragmentation speed, a hallmark of the eruption dynamics, is likely to be directly affected by the pressure distribution within the volcanic conduit or dome.

4.1   Sample description

During two field campaigns at Unzen Volcano several blocks (approximately 40 cm x 40 cm x 9 cm) of different porosity were sampled from the 1990-1995 pyroclastic flow deposits of Unzen, most of them in the Mizunashi Valley. The investigated rocks of Soufrière Hills Volcano (Montserrat) were sampled by Dr. Oliver Spieler at the Belham Valley from the pyroclastic flow deposits of the 1997 Vulcanian eruptions.

For fragmentation experiments, cylindrical samples of 25 mm diameter were drilled out of sampled blocks. The samples were cut and polished to a length of 60 mm with parallel ends. For all samples the open and closed porosity as well as the density were determined using a helium pycnometer. The mean density and porosity of each set of samples were calculated. The density scatter of the samples from each set was analyzed and the samples with smallest deviation were chosen for fragmentation experiments to ensure comparable starting conditions.

It is important to note that the samples taken for fragmentation experiments, as well as all other experimental investigations, simply represent the large grain size

fraction of the block and ash flow deposits. A complementary fine fraction also exists. Importantly, no evidence could be found that these complementary coarse and fine fractions differ in initial porosity. Thus they do not appear to be generated from different starting materials. Therefore the obtained porosity range can be regarded as representative of the pre-fragmentation porosity range in the respective Unzen domes, from which they originated. For the same reason the samples from Montserrat are supposed to allow a re-assemblage of the pre-eruption state of the conduit of Soufrière Hills volcano, Montserrat, prior to the Vulcanian eruptions August - October 1997 and on Boxing Day 1997.

4.2   Methodology

The fragmentation experiments were performed with a shock-tube-like apparatus (*Alidibirov and Dingwell*, 1996a,b; *Spieler et al.*, 2003, 2004a). The apparatus consists of two main parts; a large low-pressure tank to collect the fragmented sample, 3 m long, 0.4 m wide and at atmospheric pressure conditions. The second part is the autoclave with the sample inside. The autoclave can be pressurized to up to 40 MPa using Argon gas and gas compressor to reach higher pressure values than flask pressure. A system of two to three diaphragms separates the tank from the autoclave (Fig. 4.1). The diaphragms are produced by imprinting a circle and a cross in a circular metal plate. The pressure resistivity of the diaphragms can be influenced by using different material (aluminium, copper, iron), different thickness (0.3 mm - 1.0 mm) and different imprint depth. By this, diaphragms with an failure pressure from 0.7 MPa to up to 17 MPa can be produced, the variation in the opening pressure is 5 - 10 %. The advantage of using more than one diaphragms persists in the gradual pressure built-up and allows the pressurization of the autoclave to exactly the desired conditions. For example a set of three diaphragms with failure pressure of 13 MPa may be used to setup a 30 MPa experiment; each diaphragms is exposed to a relative pressure difference of 10 MPa. The system is triggered by the systematical failure of the uppermost diaphragm. This almost instantaneously leads to the failure of the other two diaphragms and thus the rapid decompression of the high pressure autoclave. A shock wave is generated and travels into the low pressure tank, and a rarefaction wave propagates down into the autoclave.
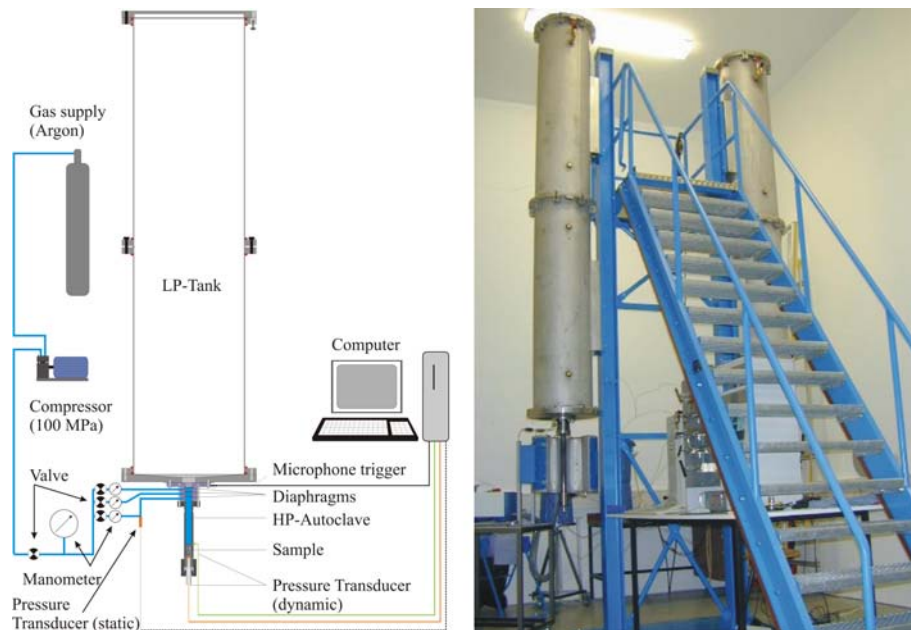
Figure 4.1: The shock-tube based fragmentation apparatus, also called the fragmentation bomb, to the left a schematic draw, to the right a photo. (modified after *Spieler et al.* (2004a)).

By the time this rarefaction wave reaches the sample, a pressure gradient is created below the sample surface. Once a certain height and steepness of the gradient is overcome, a layer-by-layer fragmentation due to vesicle bursting of the sample ensues (Fig. 4.2). In the case, that the critical pressure gradient is not reached, no fragmentation occurs and the pressure within the sample is reduced solely by gas filtration through the sample. The steepness of the pressure gradient is controlled by the initial pressure difference between the pressurized sample and the atmospheric conditions in the low pressure tank as well as the permeability of the sample (*Mueller et al.*, 2005).

Previously the sample size usable for fragmentation experiments was limited to 50 mm length and 17 mm diameter (*Spieler et al.*, 2004a). A modified autoclave now allows cylindrical samples of 60 mm length and 25 mm diameter. The length of the autoclave above the sample is 102.5 mm. The sample is glued with a mounting adhesive (crystalbond 509) into a brass sample container (Fig. 4.3). Remnants of the sample or only partially fragmented samples can be removed from the sample container by applying heat and cleaning with acetone.
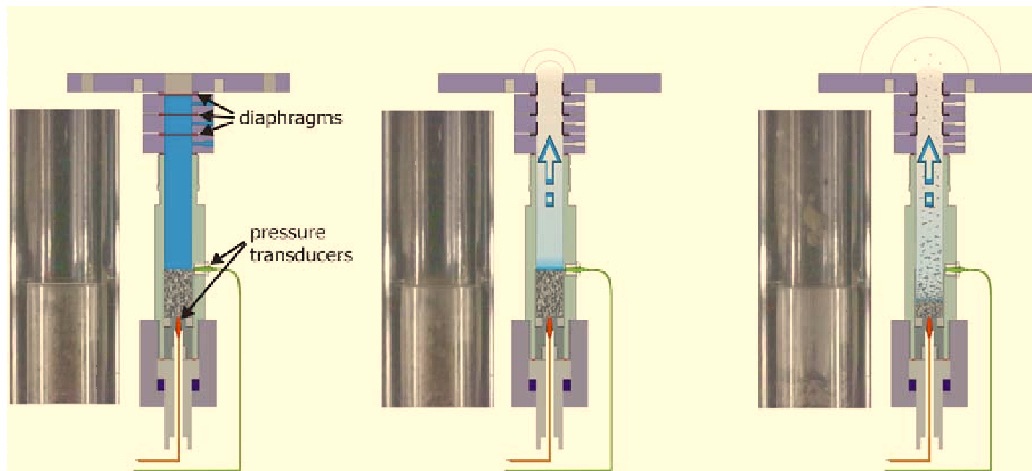
Figure 4.2: The high pressure autoclave is separated by three diaphragms from the low pressure tank. Two dynamic pressure transducers are installed directly above and below the sample (25 x 60 mm) to record the pressure drop curves during rapid decompression of the sample. Left next to the sketches there are screen shots taken out of an high speed movie recorded of an experiment with a MUZ BKB sample. Left: The diaphragms are closed and sample and autoclave are pressurized. Middle: The unloading wave arrives at the sample and first particles are blown out of the sample surface. The pressure gradient through the sample starts to build up. Right: The threshold of the sample is overcome and a layer-by-layer fragmentation is travelling into the sample. At the screen shot the sample is already 2/3 fragmented.
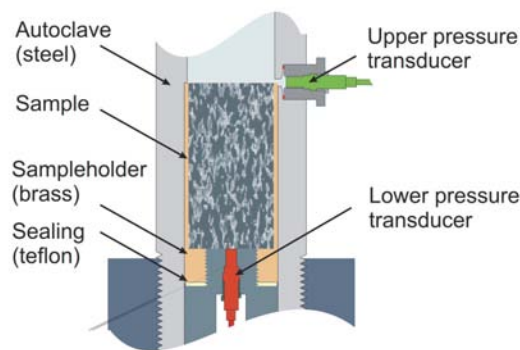
Figure 4.3: Close-up of the autoclave used for fragmentation speed analysis. The sample is glued in a brass sample holder and placed in the gastight sealed autoclave. At the top and the bottom of the sample a dynamic pressure transducer (Kistler, 601H) is located, which detects the pressure drop at that place.

The pressure evolution in the autoclave is recorded with a static pressure transducer (Kistler, 4075A500) fixed to the gas inlet below the undermost diaphragm. Two dynamic pressure transducers (Kistler, 601H) are used to quantify the speed of the fragmentation front travelling into the sample. These transducers are located directly above and below the sample (Fig. 4.3). As the operating temperature range of the transducers is 0 - 200 °C, the experiments are performed at room temperature. The speed of fragmentation is calculated from the distance of the pressure transducers (which is equal to the sample length) and the time delay between pressure drop above and below the sample. The additional static pressure transducer allows to control the slow pressurization of autoclave and sample. The actual pressure at the dynamic transducers can be monitored over the entire experiment. This enables to control roughly the pressurization process of the sample. At dense samples sometimes a huge time lag was observed, in these cases the pressurization rate was reduced. Once the final pressure for an experiment is reached at all transducers, the sample dwells under these conditions for 5 - 10 minutes. After this time, it is assumed that even small open pores got filled with argon, resulting in a homogeneous pressure distribution over the entire sample.

4.3   Testing of setup and transducers

Figure 4.3 showed the exact location of the dynamic pressure transducers in respect to the sample. A time delay between arrival of the unloading wave at the samples surface and the signal drop on the upper pressure transducer, resulted by the embedding of the transducer in the autoclave might be expected. Therefore a setup was developed to clarify this question and, if necessary, correct the gained data. A distance holder was constructed, which brought the lower pressure transducer to exactly the same height as the sample surface in an experiment. Then rapid decompression experiments were conducted at several initial pressures and the pressure signals recorded. The analysis of the pressure drop signals revealed that there is no obvious time delay between the onset of pressure drop at the two pressure transducers or, in other words between the arrival of the rarefaction wave at the sample surface and the upper transducer. A slightly slower pressure drop was observed at the upper pressure transducer, this can be related to the filtration effect of the gas through the 1.87 mm drilling in front of the pressure

applied pressure (MPa)	sound speed in Ar (m/s)	decompression rate within 0.1 ms (GPa/s)
0.1	319	0
10	356	16
20	383	46
30	422	90
40	451	135

Table 4.1: The sound speed of pressurized Argon gas was determined for different applied pressures from the records of decompression experiments with an empty sample container. Additionally the decompression rates for the used setup were calculated at these different applied pressures steps.

transducer.

In another set of experiments an empty sample container was used to determine the speed of the rarefaction wave travelling through compressed Argon gas at different initial pressure steps. The speed of sound of Argon under atmospheric pressure conditions and 20 °C is given as 319 m/s in literature (*Glenn*, 2005). At 10 MPa an unloading velocity of 356 m/s was determined, and at 40 MPa in 451 m/s (Tab. 4.1). In addition the decompression rates for the setup geometry at different applied pressure were calculated. Within the first 0.1 millisecond the decompression rate was determined to 135 GPa/s at 40 MPa initial pressurization, and to 16 GPa/s at 10 MPa (Tab. 4.1).

4.4   Results

For each sample set a series of experiments with increasing applied pressure were performed in order to determine the fragmentation threshold. The initial pressure applied to the sample in the first test was usually 2.0 MPa. If no fragmentation occurred, the initial pressure was raised by an increment of circa 1.0 MPa and the same sample was used for the next experiment. This process was continued until a first fragmentation occurred with, in most cases, a removal of only a few millimeters of the sample surface. This pressure is termed the fragmentation initiation (FI). Usually with about 0.5 - 1.5 MPa above FI, complete fragmentation of the sample is reached. This pres-

sure is called the fragmentation threshold (FT). At pressures between FI and FT, only parts of the samples are fragmented. Either permeable flow through the sample apparently reduces the pressure gradient below FI, or a variation in the tensile strength within the sample, caused by natural inhomogeneities of the vesicle and crystal distribution increases FI. In any case, the energy provided by the compressed gas is not high enough to fragment another layer and the fragmentation stops. The remaining overpressure is reduced by permeable flow through the sample (see also *Spieler et al.*, 2004a; *Mueller et al.*, 2005). At a pressure range between FI and FT or slightly higher, the fragmentation process is very sensitive to any kind of irregularity. Material inhomogeneities can trigger a fragmentation below the average threshold of the sample or prevent a fragmentation above this threshold. Therefore the threshold is best described as a pressure range over $\pm$ 0.5 - 1.5 MPa, dependent on the natural textural variability of the sample.

The question may arise whether the repetitive pressurization and decompression of the same sample below FI influences the rocks strength. However, it turned out that repeated experiments at a pressure slightly below FI did not result in a lowered FT.

4.4.1 Unzen Volcano

More than 100 experiments were carried out on six field samples with differing porosities. The open porosity of the sample sets were compiled to 5.5, 6.7, 13.1, 20.8, 33.0, 33.8 and 52.2 vol.%, the highest porosity being from a breadcrust bomb (see Tab. 2.1 and Tab. 4.2). As mentioned earlier, this range covered the porosity variation determined for the block-and-ash flow deposits of Unzen Volcano by field measurements very well (3.0 vol.% - 55.0 vol.%, Fig. 2.4).

For each sample set, first the fragmentation threshold was analyzed as described above. The threshold was reproduced in several experiments and an average threshold was defined (Tab. 4.2). A characteristic selection of all experiments is listed in Table B.2. The speed of fragmentation wave was measured at initial pressure differences ΔP of 10 MPa, 20 MPa, 30 MPa, and 40 MPa, as soon as the fragmentation threshold of the relevant sample set was overcome. At some sample sets, experiments at intermediate pressure differences were conducted in order to refine the observed speed curves. The fragmentation speed is calculated from the sample length (60 mm) and the time delay

sample	open porosity (%)	mean FT (MPa)	std FT
MUZ 2001 A*	5.5	23.0	1.8
MUZ 2001 A	7.6	18.0	2.5
MUZ 2000 D	13.3	13.5	1.2
MUZ 2001C	20.8	10.5	1.0
MUZ 2000 G	33.0	8.0	1.3
MUZ 2000 F	33.8	7.0	1.1
MUZ BKB	52.2	5.0	0.5

Table 4.2: The fragmentation threshold of the analyzed sample set of Unzen dacite. The FT values were averaged over several experiments and their standard deviation (std) is given. At the sample set MUZ 2001 A, a subgroup with an open porosity of 5.5 % was established and treated separately. The open porosity is averaged over all performed fragmentation experiments (Tab. 2.1b).

Δt of the pressure drop over the entire sample, recorded by the transducers above and below the sample. Figure 4.4 shows pressure signals of two sample sets, each at several initial pressure differences (ΔP). At the top, five experiments of the sample BKB with 52.2 vol.% open porosity are shown, the lower diagram derives from the sample 2001 C (20.8 vol.% open porosity). With increasing ΔP, the time gap between the pressure drop above and below the sample decreases i.e., the speed of fragmentation increases.

Some of the pressure drop curves are quite noisy. Several kinds of noise were discernable. Noise with an average frequency of ~ 10 kHz could be related to insufficiently opened diaphragms. Parts of the diaphragm were not fully extracted from the gas flow and caused reflections. The expected and also observed frequency of ~ 10 kHz derived from the distance between the transducers and the diaphragms. This "diaphragm noise" is most strongly seen on recordings of the upper pressure transducer, as on the recordings of BKB at 20 MPa and 30 MPa (Fig. 4.4, top). This noise could sometimes also be traced to the recordings of the lower transducer, as seen on the record of 2001 C at 20 MPa (Fig. 4.4, bottom). The reflection on the lower transducer around 15 MPa as well as 10 MPa is caused by a badly-opened diaphragm. A higher frequency noise was observed dominantly on the lower transducer recordings. The origin of this noise is still open to speculation. It seems to be related to higher initial pressure differences and may result for instance from a relaxation of the teflon sealing between sample holder and pressure transducer assemblage, a general loosen of the fixing of the sample container or also a slight lifting of the sample. A pressure
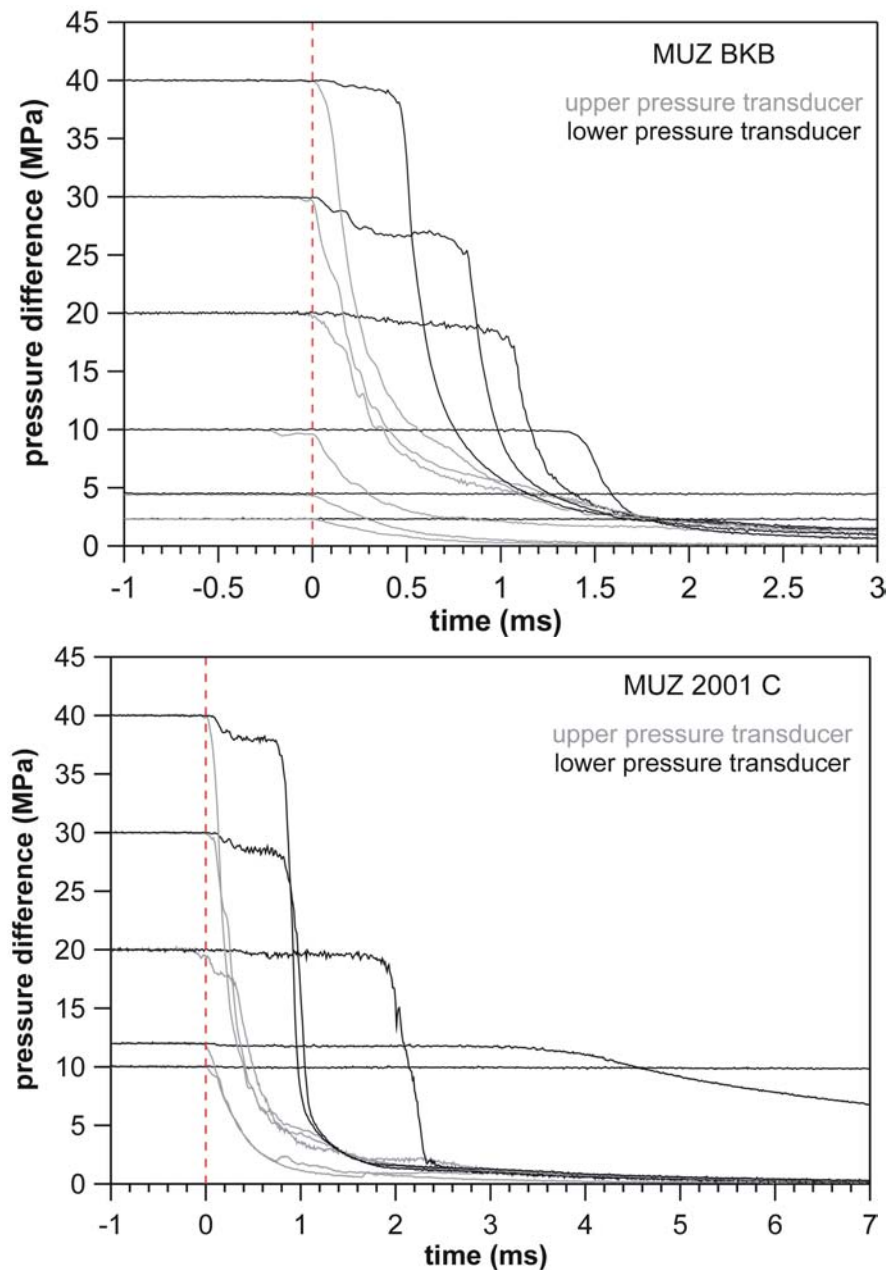
Figure 4.4: Pressure signals recorded during fragmentation experiments, using two dynamic pressure transducers above and below the sample. The speed of fragmentation is calculated from the sample length and the time lag of the pressure drop. With increasing pressure the time delay becomes shorter. Top: Five experiments of the sample MUZ BKB (52.2 vol.% open porosity) at different initial pressures. Bottom: Experiments on the sample MUZ 2001C (20.8 vol.% open porosity) at different initial pressures. At both sample sets, the experiment at lowest pressure is below FT, and the pressure is reduced by permeable gas flow trough the sample.

Figure 4.5: The speed of fragmentation (left) and the fragmentation threshold (right) for five sample sets with different porosity. The diagram on the right hand side contains also the experiments below FT, performed to determine the fragmentation threshold. The speed can be fitted using an logarithmic relationship, the threshold with an inversely proportional power-law relationship.

drop at most of the 30 MPa and 40 MPa experiments was detected on the recordings of the lower transducer at the time the rarefaction wave reaches the sample. This sudden pressure drop may be explained by a slight lifting of the sample in the sample container prior to fragmentation. Both kinds of noise do not affect the interpretability and significance of the recordings.

In some cases, the influence of permeable gas flow through the sample which reduces the effective pressure difference for the fragmentation, can be detected on the pressure drop curves during fragmentation. The experimental record of BKB at 20 MPa shows this effect (Fig. 4.4, top). The pressure on the lower transducer slowly decreases prior to the sudden pressure drop, indicating the full fragmentation of the sample. It is not possible to estimate the permeability from this recording, as the sample length changes constantly due to the ongoing fragmentation.

Figure 4.5 displays the fragmentation speed for the six investigated porosity sets relative to the initial pressure. The corresponding data are listed in Table B.2. The speed of fragmentation increases with increasing applied pressure. The strongest effect was observed at initial pressure values around FT. There is apparently a logarithmic

relationship between the fragmentation speed and the initial pressure difference. At the maximum pressure applied to the samples (40 MPa), 6.7 vol.% porosity resulted in a speed of 45 m/s and 52.2 vol.% porosity gave 134 m/s. This demonstrates that the speed is also highly influenced by porosity with an increase in porosity directly yielding an increase in the speed of the fragmentation process.

The intersections of the speed curves with the pressure axis in Figure 4.5 (corresponding to a speed of 0 m/s) represent the fragmentation initiation for the different samples. Here it was decided to merge the values FI and FT, since it turned out that for a single sample one can very well distinguish between these values, whereas the natural inhomogeneity of the entire sample sets causes variations too wide to maintain such a discrimination in a sensible manner. A mean FT value was defined, which is best understood as a range with the bandwidth given by the standard deviation (Tab. 4.2). A theoretical speed of 0 m/s was assigned to this (mean) FT. The relative values of FT reflect the strong influence of porosity on the threshold. The threshold seems to be related to the open porosity by an power-law relationship with an exponent of -0.65. For the most dense sample set (2001 A) a subdivision was formed containing again the most dense samples within this set. The subgroup 2001 A* exhibits a mean open porosity of 5.5 vol.%. The subgroup is marked with crosses in the fragmentation speed diagram of Figure 4.5, for the FT curve in the same figure it is illustrated as a separate point. The FT diagram of Figure 4.5 contains also experiments performed at very low initial pressure (below FT), performed in order to obtain the fragmentation threshold for each sample set. *Spieler et al.* (2004b) described in detail the decrease of the fragmentation threshold with porosity, based on the results of high temperature experiments (850 - 900 °C).

4.4.2 Montserrat

The investigated samples of Soufrière Hills Volcano, Montserrat, could be grouped into four sample sets, depending on their porosity and texture. These sets contain an average open porosity of 2.5 %, 19.4 %, 43.9 % and 67.1 % (see Tab. 2.1). More than 50 experiments were carried out to describe the fragmentation behavior of these samples. An outstanding characteristic of the Montserrat samples compared to the
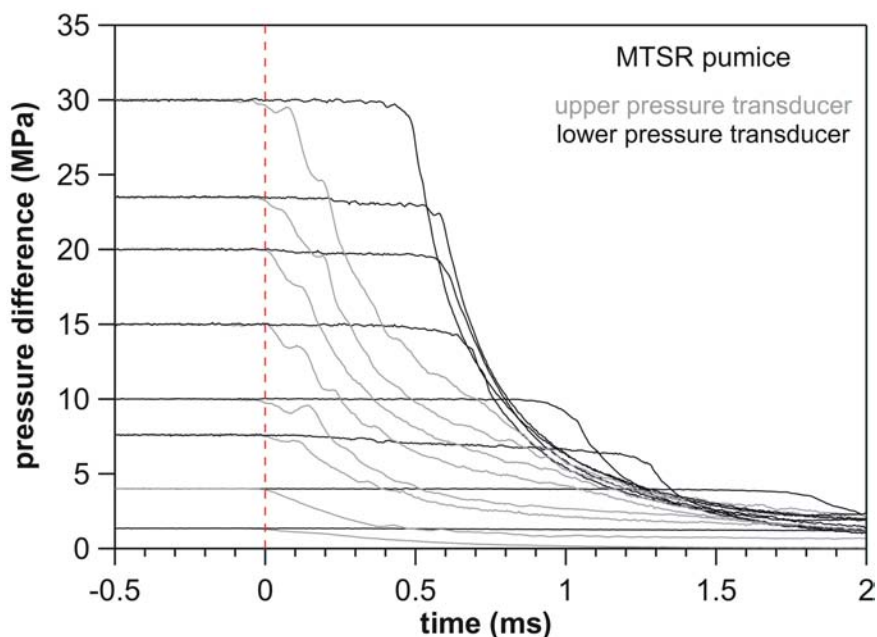
Figure 4.6: Pressure drop curves of fragmentation experiments on the sample set MTSR pumice (67.1 vol.% open porosity) at different initial pressures. The pressure signals were recorded with two dynamic pressure transducers above and below the sample. With increasing pressure the time delay becomes shorter. The experiment at lowest pressure is below FT, and the pressure is reduced by permeable gas flow trough the sample.
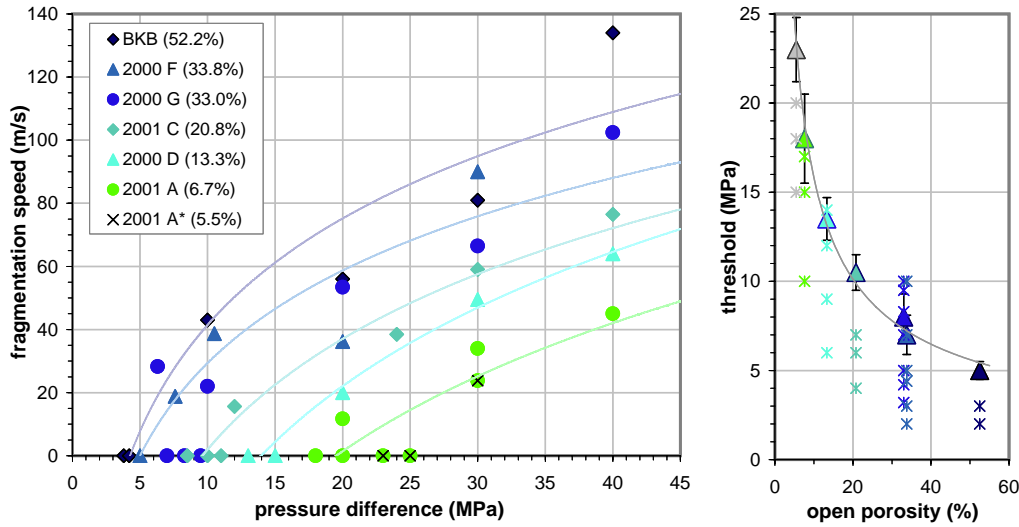
sample derived from Unzen is the, overall speaking, smaller size of the phenocrysts. Just the Montserrat pumice contains comparable large hornblende phenocrysts to the large phenocrysts fraction within the Unzen dacite (mainly plagioclase).

The analytical procedure was identical to the investigations made on Unzen samples. In a first series of experiments the fragmentation threshold was determined. An average FT was defined from several experiments. Analogous to the Unzen samples the discrimination of FI and FT was set aside. With a second set of experiments the propagation speed of the fragmentation process was analyzed. The experiments were conducted at differently initial pressure starting slightly above FT, preferentially at a ΔP of 10 MPa, than the applied pressure was raised by increments of 5 MPa to up to 30 MPa, for the very dense sample set to 40 MPa. A selection of all experiments which cover the range of observed behavior is given at Table B.3.

Figure 4.6 shows the records of eight experiments ranging from 2.4 MPa initial pressure difference and only slow gas filtration through the sample to a ΔP of 30 MPa

and a very fast fragmentation with 150 m/s. Most of the pressure drop curves recorded at the upper transducer showed the typical noise due to only moderately opened diaphragms. At 15 MPa however only the record of the lower transducer seemed to bear that diaphragm noise. The higher frequency noise could be observed again predominantly at the lower transducer recordings. Its amplitude increased slightly towards higher ΔP, supporting the possible origin of this noise by relaxation of the teflon sealing or the slightly loosing of the fixation of sample container and transducer.

Much less sample material derived from Montserrat was available for fragmentation experiments than in the case of Unzen. Therefore the sample length had to be reduced to values between 40 - 60 mm for some of the experiments at all sample sets but the pumice. The changed length was accounted for the fragmentation speed analysis.

The speed of fragmentation of each sample set increases clearly with increasing applied pressure difference (Fig. 4.7). The variance within most sets was found to be lower compared to the Unzen samples. Only the inhomogeneous sample set of the striped pumices (43.9 vol.% open porosity) exhibits a similar variance compared to Unzen samples (Fig. 4.5). The increase of the speed of fragmentation with initial pressure difference is best described by a logarithmical relationship; just slightly above FT the speed of fragmentation reacts very sensitively to small pressure changes. Further a clear influence of the open porosity on the fragmentation speed could be observed. For instance at a ΔP of 15 MPa a fragmentation speed of 90 m/s was calculated for the pumice samples, 60 m/s for the stripy samples, 22 m/s for the mid dense samples, whereas the pressure was far below FT at the very dense samples.

The fragmentation threshold of the four sets is shown in the right diagram of Figure 4.7 and as intersections of the speed curves with the pressure axis in the left graph of the same figure. Again, the threshold strongly decreases with increasing open porosity. The FT curve of the Montserrat samples could be best fitted using a power-law relationship with an exponent of -0.71. The right plot of Fig. 4.7 contains also the experiments at which no fragmentation occurred, they were marked with crosses in the plot. These experiments were conducted in order to evaluate the fragmentation threshold.

sample	open porosity (%)	mean FT (MPa)	std FT
MTSR very dense	2.5	30.0	2.5
MTSR mid dense	19.4	10.0	1.5
MTSR stripy	43.9	5.0	1.0
MTSR pumice	67.1	2.5	0.4

Table 4.3: The fragmentation threshold of the analyzed four sample sets of Montserrat. The FT values were averaged over several experiments and the standard deviation (std) is given. The open porosity is averaged over all performed fragmentation experiments (Tab. 2.1b).
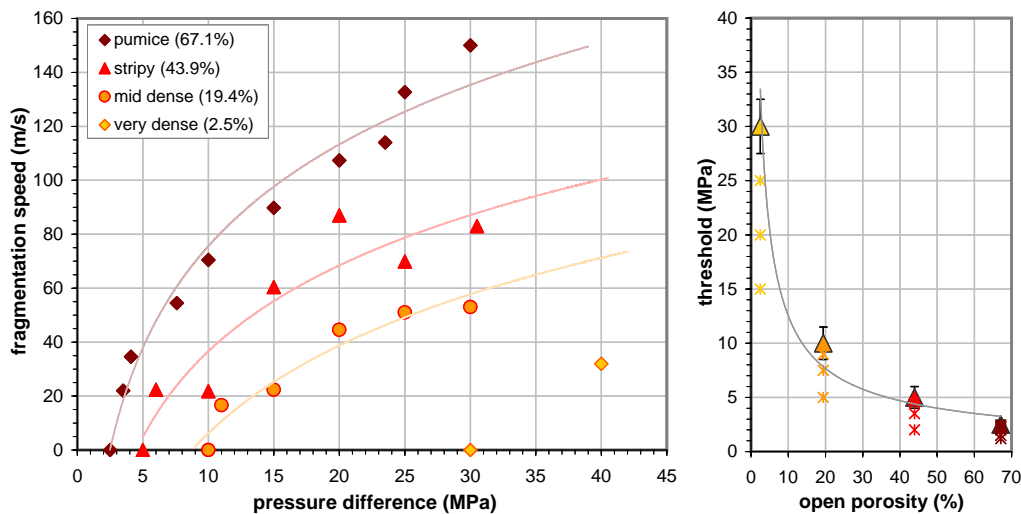
Figure 4.7: The speed of fragmentation (left) and the fragmentation threshold (right) for all analyzed samples sets of Soufrière Hills Volcano, Montserrat. The diagram at the righthand side shows also the experiments below FT, performed to determine the fragmentation threshold. The fragmentation speed follows a logarithmic relationship with the pressure difference, the threshold an inversely proportional power-law relationship with increasing porosity.

4.4.3   Influence of experimental temperature

During the Unzen dome eruptions the magma being fragmented ranged in temperature from ca. 800 °C down to a few hundred degrees. The highest fumarole gas temperature measured was constantly around 800 °C (*Nakada and Motomura*, 1992, 1999). During the initial stage of the eruption surface temperature measurements using an infrared thermal video system revealed temperatures around 550 °C at the dome and the active vent. In October 1991 a maximum temperature of 658 °C was measured at the dome (*Umakoshi et al.*, 1992). The thermal imagery showed temperatures up to 300 °C at the front of the growing lava dome and temperatures between 110 and 280 °C at rock falls and pyroclastic flows.

Spieler et al. (2003) obtained that at Mt. St. Helens cryptodome dacite the threshold is shifted drastically from 9 MPa at room temperature to 3 MPa at 900 °C. Further the size distribution of particles generated during comparable experiments shifts to finer particles at the cold experiments. These results were obtained at smaller samples than used in this study, the sample diameter was 17 mm at a sample length of 50 mm. At this small diameter the different glue used for cold and hot experiments is suggested to bear a much larger influence compared to the samples with 25 mm in diameter.

The experiments presented in this study were performed at room temperature (Fig. 4.8). The hereby gained FT values were compared to FT values resulted from experiments at 850 °C. The hot experiments were also conducted on large (25x60 mm) samples derived from Unzen Volcano and Montserrat (*Kueppers et al.*, 2005a; *Spieler et al.*, 2004b). At the experimental temperature of 850 °C the samples are above the calorimetric glass transition temperature. For Unzen dacites the glass transition temperature was determined to be 720 °C measured on glassy samples (quenched from powder molten at 1500 °C) at 20 K/min. heating rate (*M. Potuzak, pers. comm.*). The glass transition temperature can by predicted from the viscosity using two fits, Avramov and Tamman-Vogel-Fulcher equation, respectively (*Moynihan*, 1995). For Montserrat andesites values of the glass transition temperature between 670 - 700 °C were calculated following these equations (*M. Potuzak, pers. comm.*). In general the fragmentation threshold values derived by the cold experiments tend to be higher, but still comparable to the values gained at 850 °C. The slight difference may result from
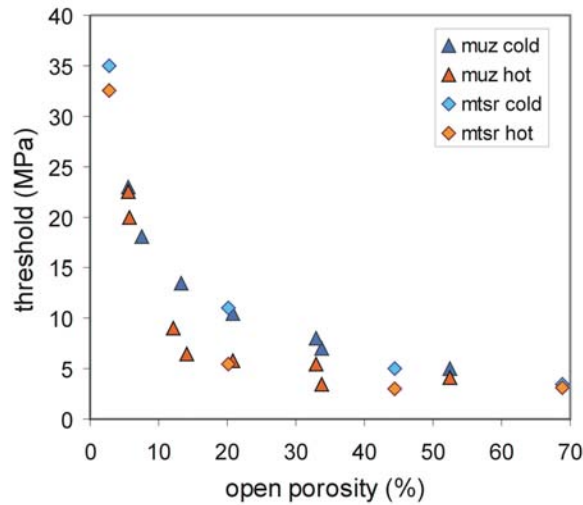
Figure 4.8: Comparison of hot (850 °C) and cold values of the fragmentation threshold of Unzen and Montserrat samples. The experiments at 850 °C were conducted by *Kueppers et al.* (2005a). In general the fragmentation values derived by the cold experiments tend to be higher.

the different assemblage and different glue used at room temperature and high temperature experiments.

Thus the dynamics of fragmentation investigated here are believed to be applicable to fragmentation over a wide range of temperature from room temperature up to eruptive temperature as long as the mechanism remains brittle.

4.5   Discussion

4.5.1   Restriction of the fragmentation speed

The measured fragmentation speed of each sample set exhibits a positive logarithmic dependence on the initial pressure difference. The maximum speed, reachable by the propagation of the fragmentation process, seems to be restricted. The restriction is assumed to be caused by the maximum speed, the gas-particle mixture can be ejected after fragmentation, as this defines the maximum pressure gradient which can be built up over the fragmentation front. This is presumed to be the sound speed of a pressurized dusty gas (*Cagnoli et al.*, 2002) with a solid to gas mixture equal to the porosity of the analyzed sample. The particle size of the ejected particles also influences the
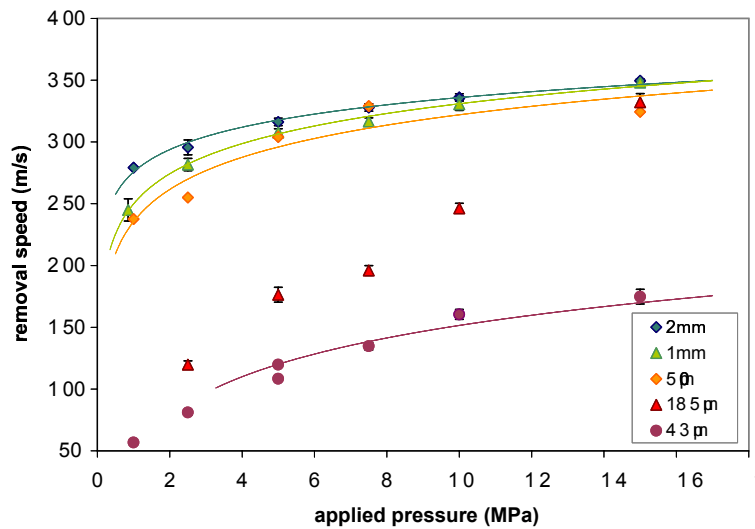
Figure 4.9: The removal speed of loose glass beads with different diameter out of the sample container was analyzed under several applied pressure situations. The speed was determined analogously to the fragmentation speed of a rock sample.

sound speed of a dusty gas. The ejection characteristics of differently large, loose glass beads at initial applied pressure values of 1 - 15 MPa is shown in Figure 4.9. The void space between the glass beads was calculated to be 36 - 40 %. The removal speed of particles $\geq$ 500 μm is very similar and seems to be limited to values shortly below the sound speed of pressurized gas, at 15 MPa a removal speed of about 350 m/s was observed. The difference between the removal speed of glass beads and gas, as well as the significantly slower removal speed at low applied pressure may result from the drag force, which has to be overcome before ejection. At the smallest particle size a removal speed of only 175 m/s was obtained, showing the influence of particle size on the ejection speed of a dusty gas. The particles with a diameter of 185 μm show a transitional behavior between fine and large particles.

As only a small part of the weight fraction of particles generated by the fragmentation process tend to be $\leq$ 500 μm, or for an applied pressure greater than 15 MPa $\leq$ 185 μm, the removal speed of the large glass beads can be regarded as the upper limit of the fragmentation speed in a rock with similar porosity of 36 - 40 %.

4.5.2   Fragmentation energy and fragmentation mechanisms

For all investigated sample sets of Unzen and Montserrat a clear dependence of the fragmentation behavior, in general, and the propagation speed of the fragmentation front, in detail, with the open porosity could be observed. An increasing porosity leads to a higher speed of fragmentation because more energy (gas expansion) is available. Furthermore, at a constant porosity, the fragmentation speed increases with increasing pressure due to a steepening of the pressure gradient, which results also in more available energy due to gas expansion.

The energy E, which drives the fragmentation process is largely provided by the expansion of the pressurized gas located in the pore space of the samples, therefore $E \sim \Delta P \cdot \Phi$. In addition, a higher vesicularity reduces the thickness of the bubble walls, which may lower the strength of the sample and with that less energy is necessary for fragmentation. This effect would additionally decrease the fragmentation threshold. In laboratory investigations, as described above, only the open porosity has to be taken into account. The closed porosity can be treated similar to crystals in the matrix. This is in contrast to pressure evolution within a volcanic conduit. Here the closed pores usually bear overpressure due to diffusion of volatiles from a supersaturated melt into bubbles (*Sparks et al.*, 1998; *Lensky et al.*, 2004). At a given porosity, the initial pressure determines the amount of gas, stored in the pore space, taking the compressibility of the gas into account.

To obtain the exact value of energy available for fragmentation and ejection of the fragments, the volume V of the sample has to be taken into account:

$$E = \Delta P \cdot \Phi \cdot V$$

with porosity Φ given as fraction between 0 and 1.

In this study different sample sizes have been used to analyze the fragmentation behavior. This required the standardization of the fragmentation energy to a unit volume. Accordingly, the energy density ρ_E is defined as:

$$\rho_E = \frac{E}{V} = \Delta P \cdot \Phi$$

The SI-unit of the energy density is J/m^3.

Figure 4.10 shows the relationship of the fragmentation speed in respect to the energy density of all investigated sample sets of Unzen Volcano. The speed of fragmentation increases with increasing energy density. The scatter of data is widest at the
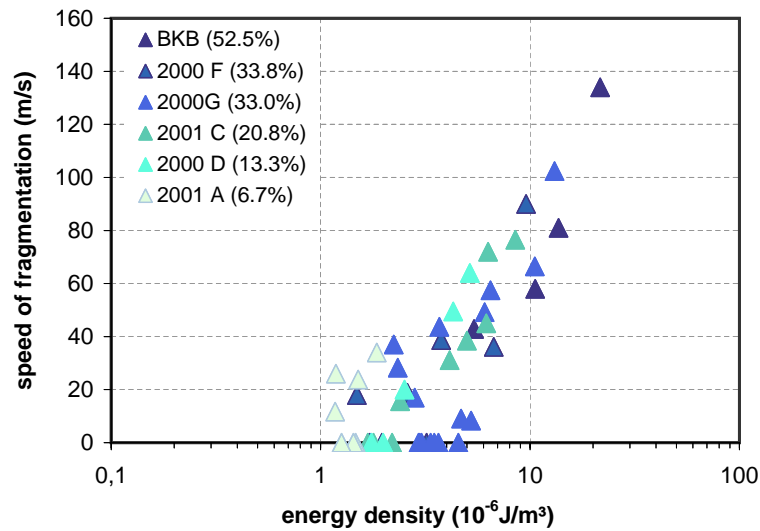
Figure 4.10: The relation of the speed of fragmentation and the energy density for all an-alyzed sample sets of Unzen dacite. In general, a logarithmical increase of the speed can be observed with the energy density as soon as a certain energy threshold is overcome. A group of highly porous samples with high permeability values deviates from the trend towards higher energy density values.
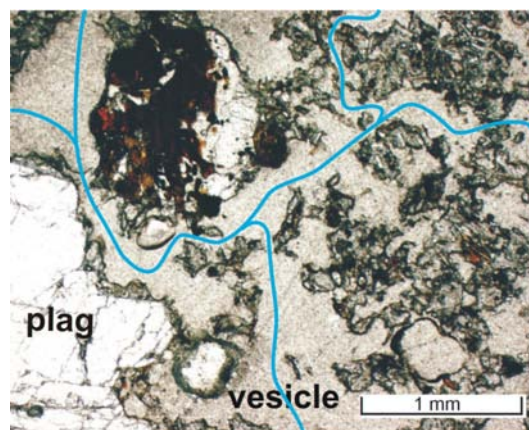
Figure 4.11: Microphotograph of a very porous Unzen dacite (2000 G, 33.0 % open porosity). The vesicles are irregularly formed and highly connected. The blue lines show a possible connected pathway through the sample.
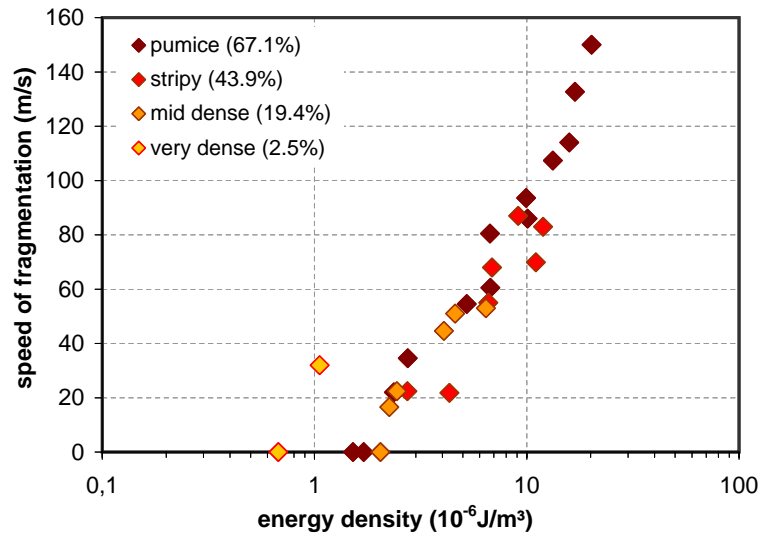
Figure 4.12: The relation of the speed of fragmentation and the energy density for all analyzed sample sets of Montserrat. A clear logarithmical increase of the fragmentation speed can be observed with the energy density as soon as a certain energy threshold is overcome. Only the very dense samples show a parallel shift to lower energy values.

energy values at the x-axis, describing the energy density needed to initiate fragmentation as well as shortly above this value. Again, this scatter is to a big part caused by the inhomogeneity of the Unzen dacite. Almost all samples in Figure 4.10 that require energy density values $> 2 \cdot 10^{-6}$ J/m^3 to undergo a fragmentation belong to the sample set 2000 G, containing 33.0 % porosity. This samples are characterized by mostly large fringed vesicles (Fig. 4.11). The vesicles seem to be highly connected, resulting in high permeability values (*Mueller et al.*, 2005).

The fragmentation speed of the Montserrat sample sets shows a close relationship to the energy density (Fig. 4.12). The results of all but the very dense data sets lie on a single trend. This supports the notion of a governing role of the energy to the initiation and propagation of the fragmentation process. The very dense samples are shifted to lower energy densities. They seem to exhibit the same gradient of the increase in speed with energy, presumably resulting in a parallel trend. Due to the low open porosity of 2.5 % of this sample set a very high initial pressure is necessary to initiate fragmentation. Figure 4.13 shows two samples of this set after a rapid decompression of 30 and 40 MPa. Both samples were only partially ejected from the sample container.
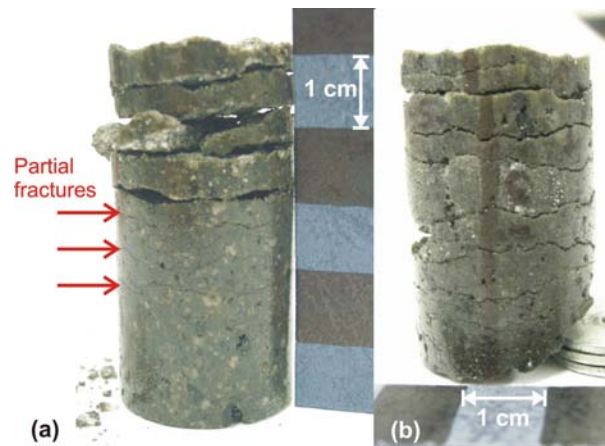
Figure 4.13: Fractured samples of the very dense sample set of Montserrat. (a) Sample with 2.25 % open porosity after experiment at 30 MPa pressure difference. The sample is only partially fractured. (b) Sample with 2.64 % open porosity after experiment at 40 MPa. The fragments of both samples were only partially ejected out of the sample container.
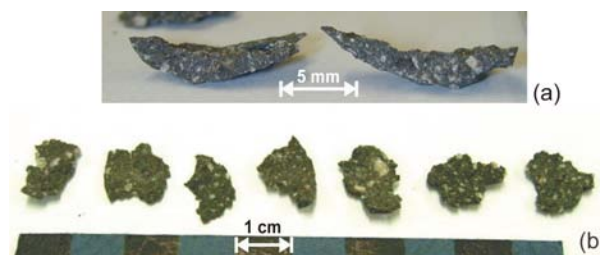
Figure 4.14: Fractured particles of Montserrat mid dense sample set. (a) Sample with 20.0 % open porosity after experiment at 20 MPa pressure difference. The platy clasts show a clear concave shape. (b) Platy clasts of a sample with 21.5 % open porosity generated by an experiment at 30 MPa initial different. Some of the very thin clasts exhibit a concave shape. This concave shape is supposed to form due to wall strengthening effects at a layer-by-layer fragmentation.

The longer part remained in the container, but was broken into more or less parallel slices. The sample at 30 MPa (Fig. 4.13a) represents an experiment close to the fragmentation threshold. Only the upper 3 cm of the sample were completely fractured, then the energy for fragmentation was attenuated leading to a partial fracture of another 1.5 cm of the sample. The bottom of the sample seems not to be fractured. The sample at 40 MPa (Fig. 4.13b) was entirely fractured, but only a few slices were ejected out of the sample container, a few more moved some millimeters up in the container and the others seemed to stay disassembled together. In both cases fractures parallel to the sample surface / rarefaction wave front were induced. The slices show no concave shape, as often observed due to wall strengthening effects during layer-by-layer fragmentation, as shown in Figure 4.14a. This, together with the high applied pressure values and the fact, that samples were entirely fragmented but not expelled gave rise to the assumption that here the fragmentation was at least partially caused by the propagation of the unloading wave through the sample (*Alidibirov and Dingwell*, 2000).

Figure 4.14 shows clasts of the mid dense sample set, generated at rapid decompression experiments of 20 MPa (a) and 30 MPa (b). Hereby the layer-by-layer fragmentation is proposed to be the major fragmentation process. The platy clasts often exhibit a concave shape related to wall strengthening effects. The glue used to fix the sample to the sample container filtrates about 1 mm into the sample (depending on porosity and pore shape), resulting in a reduced porosity at the sample rim. This lowers the fragmentation speed at the rim with respect to the center of the sample and thus leads to a concave fragmentation surface.

A comparison of Figure 4.10 and Figure 4.12 shows again the better consistency of the Montserrat sample sets, presumably caused by a generally smaller phenocryst size. A combination of both diagrams shows that the fragmentation speed is independent from the origin and composition of the samples and mainly influenced by the energy of the pressurized gas in the open pore space (Fig. 4.15). Three different areas can be distinguished in the diagram. The main part, the grey marked area, is the area dominated by layer-by-layer fragmentation due to vesicle bursting. This is assumed to be the main mechanism causing fragmentation (*Spieler et al.*, 2003, 2004b). Samples with a high permeability require higher energy densities to initiate fragmentation or to reach a certain speed, as the applied pressure may be effectively reduced due to gas

filtration flow. The area affected by this behavior is marked blue. The highly porous samples from the sets 2000 G and 2000 F of Unzen or samples of Montserrat stripy pumice represent this kind of trend. The most dense samples of both data sets deviate to lower energy values. As mentioned above this trend is very striking for the very dense samples (2.5 %) from Montserrat. A similar behavior could be observed at the most dense Unzen samples (MUZ 2001 A, 6.7 %), even though this trend is not that eye catching as for the Montserrat samples. The area of these samples is marked in red and describes the field affected by additional fracturing due to the passing of the rarefaction wave. A combination of several fragmentation processes is likely and a gradual shift of the dominating process is probable. Depending on the position within the red marked area the fragmentation may be mainly caused by the unloading wave. This accounts for samples at very low energy densities at the left side of the red area as the very dense Montserrat samples. For samples positioned on the right side of the red area a combination of both mechanisms, the fragmentation by unloading wave and the vesicle bursting, seems most reasonable. These results are in part consistent with the mechanisms proposed by *Alidibirov and Dingwell* (2000) for the fragmentation of vesicular magma.
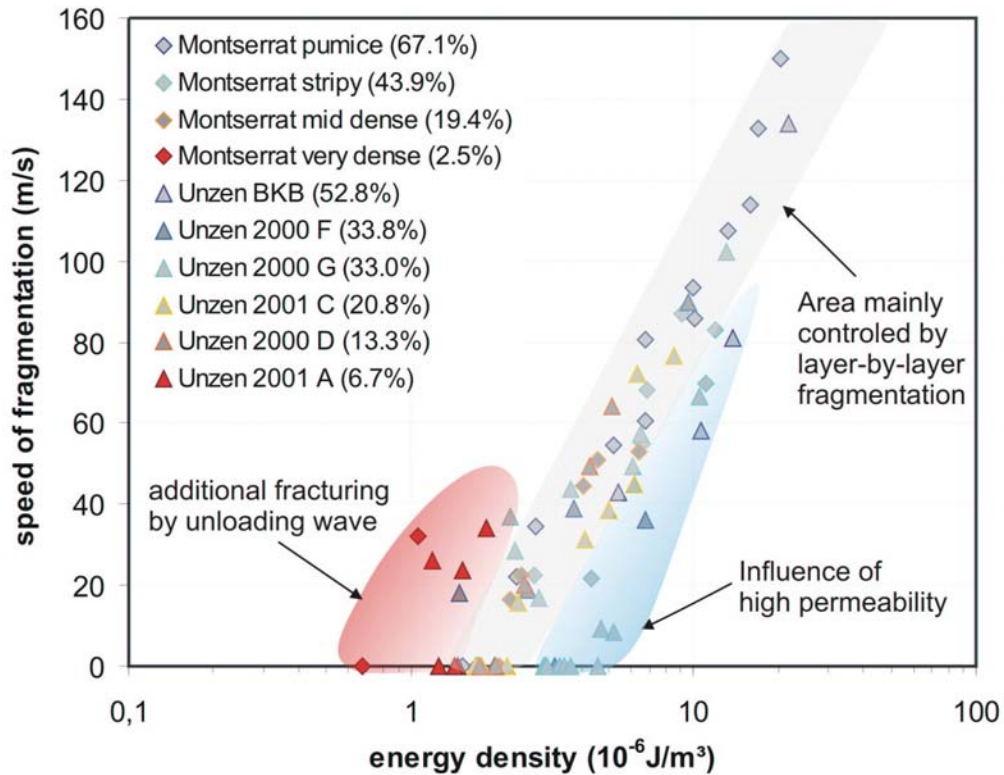
Figure 4.15: The speed of fragmentation versus the energy density for all analyzed sample sets. In general, a logarithmical increase of the speed can be observed with the energy density as soon as a certain energy threshold is overcome. Fragmentation due to vesicle burst is supposed to be the dominating fracture process (grey area). A group of highly porous samples with high permeability values deviates from the trend towards higher energy values (blue area). The most dense samples of this study deviate to lower energy values, suggesting the fracture process due to the unloading wave to become increasingly important (red area).

Chapter 5

Decompression history

This chapter focusses on the dynamics of layer-by-layer fragmentation and the pressure gradient over the sample, generated during rapid decompression of a porous rock. The shape of the pressure gradient is supposed to have a high influence on the fragmentation due to vesicle bursting. As shown in the previous chapter, this fragmentation mechanism accounts for samples over a wide range of porosity, from mid dense to porous (Fig. 4.15). Hence a special series of experiments was designed to model the pressure profile over a sample undergoing a rapid decompression event. A high permeability of the investigated samples affects the shape of the pressure profile and thus the fragmentation behavior.

5.1   Influence of permeability

The results of the fragmentation experiments discussed in the previous chapter showed that the fragmentation behavior depends in first order on the potential energy available for the fragmentation process. This energy results from the gas volume within the sample and the applied pressure. The pore structure (size, shape, and orientation) of the analyzed samples is of second order importance to the fragmentation behavior. For highly porous volcanic rocks the pore structure may result in a high permeability. High permeability values may counteract the fragmentation process as the gas overpressure inside the open pore space of the sample is efficiently reduced by filtration flow. This results in a shift of the fragmentation threshold to higher energy densities and in a significantly lower fragmentation speed for a certain energy value, compared to samples

with a lower permeability. It also leads to a faster flattening of the pressure gradient over the sample, which has been built up while rapid decompression.

An effect of permeability on the fragmentation behavior could be observed at the sample set MUZ 2000 G with an average open porosity of 33.0 vol.%. Generally the fragmentation speed increased with the energy density following a clear logarithmical relationship (Fig. 4.10). At the sample set MUZ 2000 G a subgroup was discriminated, strongly deviating from this trend towards higher energy densities (Fig. 5.1 left). Figure 5.1 (right) shows the relation of porosity and the energy density at the fragmentation threshold. The same subgroup was found to deviate from a common trend. Thus, the energy threshold was found to be largely constant over a huge range of porosity. Likewise a different origin of the samples does not affect the energy thresh-
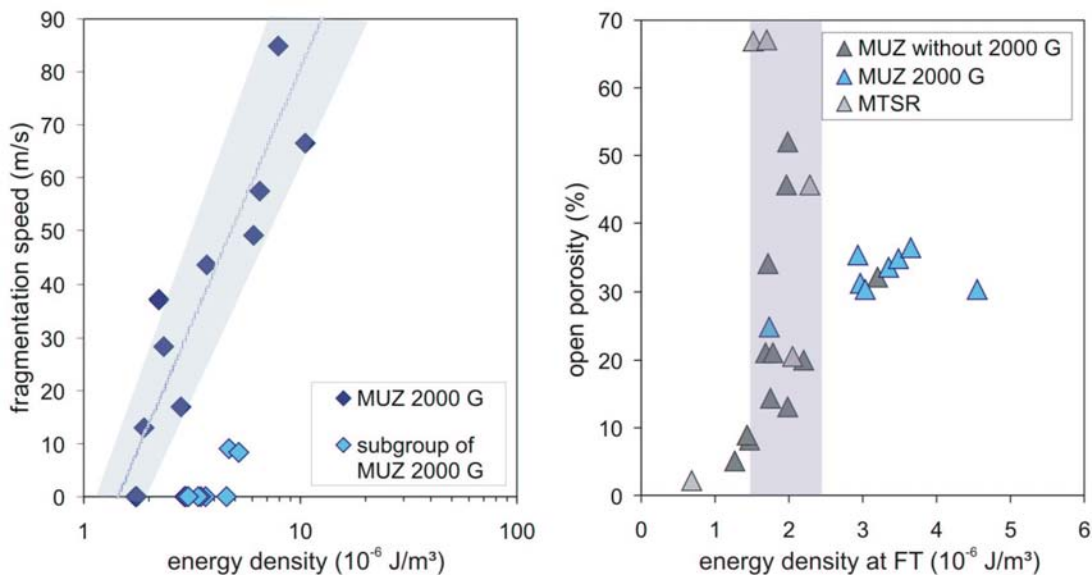
Figure 5.1: High permeability hinders the fragmentation process. Left: The fragmentation speed of the sample set MUZ 2000 G increases logarithmically with the energy density (dark blue). A subgroup (light blue) could be discriminated, which is shifted to higher energy values. Right: A certain energy density is needed to fragment the investigated samples. This energy threshold is largely independent from porosity and origin of the samples. Very dense samples show slightly lowered energy densities due to a second fracture mechanism. Most samples of the set MUZ 2000 G again deviate strongly from the trend found for all other samples towards higher energy values. The differing behavior of the subgroup of MUZ 2000 G is most likely caused by high permeability values.
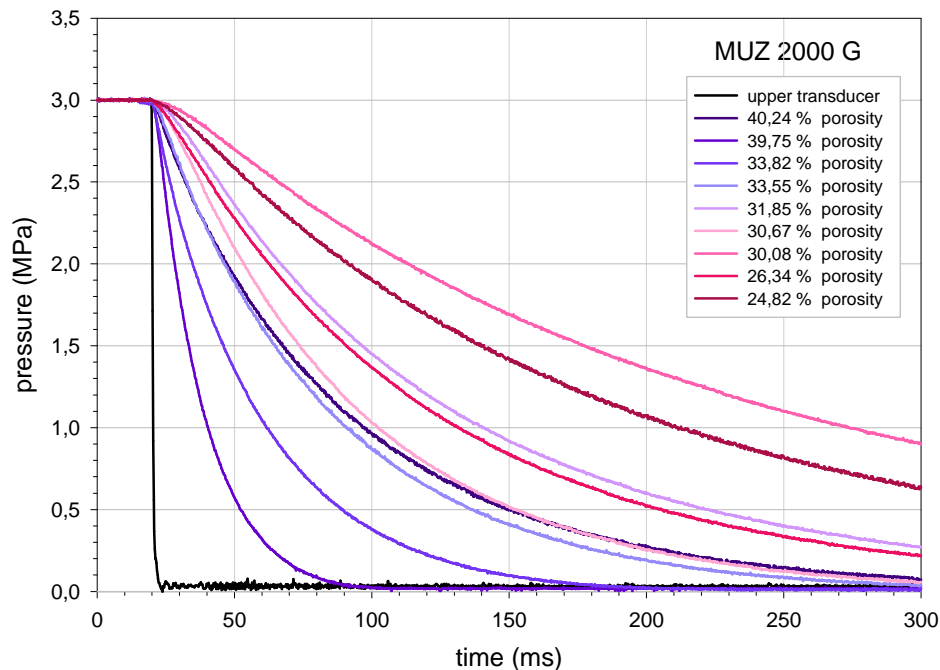
Figure 5.2: Permeable flow curves of different samples of the sample set MUZ 2000 G. All samples were decompressed from 3 MPa initial pressure to atmospheric conditions, which is clearly below the fragmentation threshold of this set (8.0 MPa). Apart from a few exceptions, the pressure drop curves become steeper with higher porosity of the sample.

old. The fragmentation seems to be initiated at an energy density of $(2.0 \pm 0.5) \cdot 10^{-6}$ J/m^3. The very dense samples exhibit slightly lowered energy densities at FT, as a second fracture mechanism (unloading wave) increasingly influences the fragmentation process (similar to Fig. 4.15). Most samples of the set MUZ 2000 G (marked blue in Fig. 5.1 right) again deviate strongly from the main trend of all other samples towards higher energy values. Their energy threshold was found to range between (2.9 - 4.7) $\cdot 10^{-6}$ J/m^3. The differing behavior of this subgroup of MUZ 2000 G is most likely caused by high permeability values. The typical vesicles observed in samples of MUZ 2000 G are comparatively large (up to 10 mm), strongly irregular in shape, and often bear a high interconnectivity (Fig. 4.11).

Pressure drop curves of various samples of the MUZ 2000 G set with a different porosity were recorded (Fig. 5.2). All experiments were conducted at an applied initial pressure of 3.0 MPa, clearly below FT of the sample set (8.0 MPa), to ensure that only

permeable flow occurred. The time interval needed for pressure equalization varied strongly. Apart form a few exceptions, the pressure drop curves become steeper with higher porosity of the sample. This is consistent with the increase of permeability observed with increasing porosity (Fig. 5.3).

Mueller et al. (2005) developed a method to determine unsteady-state permeability at a high initial pressure differential using a modified setup of the fragmentation apparatus (Fig. 4.1). The obtained permeability values of volcanic rocks range from $2.5 \cdot 10^{-15}$ to $7.6 \cdot 10^{-12}$ m^2 and show good agreement with the results of previous works (e.g. *Klug and Cashman*, 1996; *Saar and Manga*, 1999). Generally, the permeability increases with increasing porosity, following power-law relations (Fig. 5.3). The great scatter of the data demonstrates, that the permeability is not related uniquely to porosity. Textural parameters as pore size, shape and distribution may highly affect the gas flow. According to this, *Mueller et al.* (2005) interpreted the permeability distribution at the diagram as two distinct trends affected by two different textural properties influencing the gas flow: cracks and dynamically elongated pores on the one hand (Fig. 5.3a1 and a2, resp.), a network of interconnected, spherical bubbles on the other hand (Fig. 5.3b). Therefore the low-porosity range of the diagram (corresponding to effusive/dome rocks) is best described by power-law relations with exponents of 3.0 - 3.8, coincident with Kozeny-Carman-equations (based on capillary tube models; e.g. *Klug and Cashman*, 1996) and fracture flow models ("cubic law"). For approximating the trend of the highly porous samples (i.e. explosive products), a permeability - porosity model based on the percolation theory of fully penetrable spheres (FPS) was found to be appropriate (e.g. *Saar and Manga*, 1999; *Sahimi*, 1994). The combination of both approaches might be used to represent laminated pumices (Fig. 5.3c).

An investigation of the dependency between permeability and fragmentation threshold yielded no influence for low permeable samples. But from a certain transition zone between 10^{-13} and 10^{-12} m^2 on, the degassing efficiency seems to increasingly affects the fragmentation process (*Mueller et al.*, 2004). This accounts for the MUZ 2000 G sample set and proofs the permeability to be the cause for the differing behavior showed in Figure 5.1.
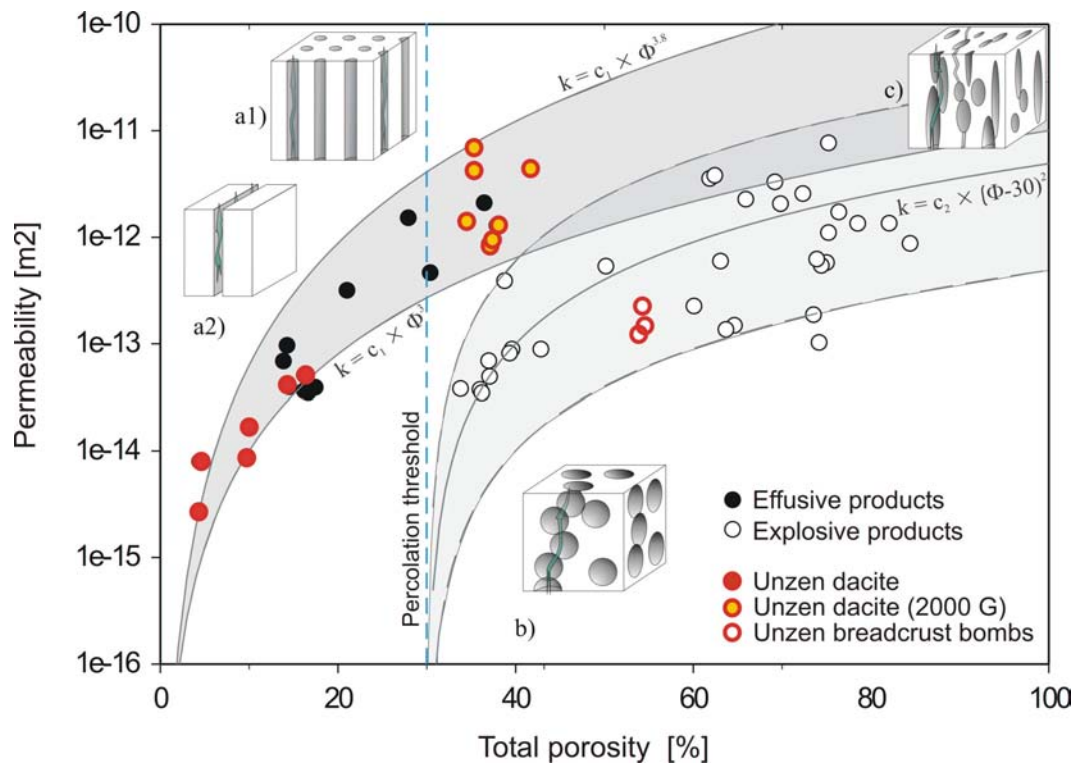
Figure 5.3: Permeability of volcanic rocks, modified after *Mueller et al.* (2005). Permeability depends on the pore texture (crack controlled, tubular structures, interconnectivity of vesicles). Different trends were observed for explosive and extrusive volcanic rocks, based on their different texture. Unzen dacite sample are shown colored in the diagram. The samples fit very well in the observed trends. The MUZ 2000 G samples (separately marked) exhibit the highest permeability values of all investigated Unzen dacites.

5.2 Pressure profile along a sample at rapid decompression

To elucidate the influence of the pressure gradient on the fragmentation behavior, an experimental setup was developed to reconstruct the pressure profiles within different porous samples undergoing rapid decompression.

5.2.1 Experimental setup

To investigate the pressure profile within a sample during permeable degassing it would be desirable to place several additional pressure transducer along the sample. As this is technically hard to realize, a different way to obtain the pressure evolution in the sample was chosen. A series of decompression experiments with the same sample, shortened stepwise from 60 mm down to 4.6 mm was conducted. All experiments were carried out at exactly the same applied initial pressure, which had to be below the fragmentation threshold. The setup for these experiments is very similar to the setup used to determine the speed of fragmentation; the same autoclave and pressure transducers have been used. The distance from the upper surface of the sample to the diaphragms is kept constant. For each part of the sample which was shortened, a brass distance holder was placed below the fitting ring of the lower pressure transducer (Fig. 5.4). The pressure drop curves above and below the sample were recorded identically as during the fragmentation speed analyzes. At several sample lengths the experiments were repeated to proof the reproducibility of the obtained pressure drop curves.

Figure 5.6 (top) shows a set of recorded pressure drop curves of a sample of the MUZ 2001 C set. Each pressure drop curve can be assigned to a distinct place in the sample (Fig. 5.5). As the curves stem from the transducer below the sample, a curve reflects the pressure evolution at the point within the sample corresponding to the actual sample length. Generally the bottom of the sample is attributed to the origin of the length axis. All samples measured 60 mm in length before they were stepwise sliced down. This means that the locations within the sample according to the pressure curves of the shortened samples were derived by: "60mm minus sample length".

The pressure values at certain time steps after the arrival of the rarefaction wave at the sample surface were excerpted out of all recordings (dashed lines at Fig. 5.6,

Figure 5.4: Setup to investigate the pressure profile within a sample. It is very similar to the setup used for the fragmentation speed analyzes. The sample is stepwise sliced down from 60 mm to 4.6 mm. The shortened sample was compensated with distance holder placed below the lower transducer.

top). These values were transposed and assigned to the relevant locations within the sample. Thus the pressure evolution at these locations at the chosen time steps could be reconstructed (Fig. 5.6, bottom).

Strictly speaking it has to be noted that this method can only be applied for the very initial, steep part of the pressure drop curve, as there is no gas volume below the shortened sample. This leads to a faster pressure drop for the shortened sample compared to the pressure evolution at the relevant location of an entire sample. But the method is applicable for the onset of the decompression event, while the steepest pressure profiles over a sample are built up. The later pressure evolution is also calculated and plotted as it still allows a qualitative statement concerning the permeability of the analyzed samples.
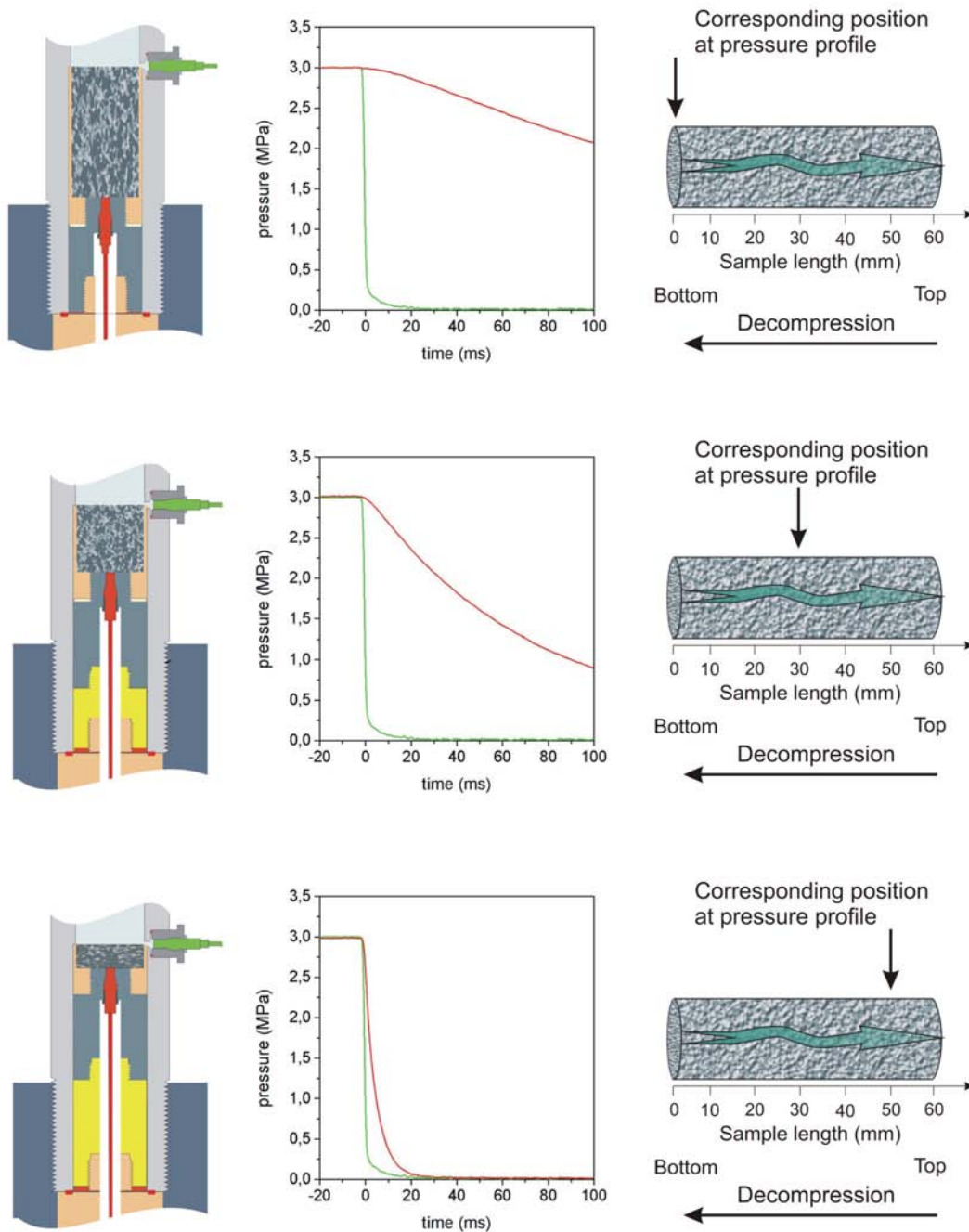
Figure 5.5: This figure aims to clarify how the pressure drop curves are related to locations along the sample undergoing rapid decompression. Left are cut-outs of the setup shown for three different sample length. A distance holder (marked yellow) to compensate the shortened sample is placed below the transducer. At the middle the recorded pressure drop curve for these samples are placed and right next to it the according position along the reconstructed sample facing a rapid decompression event.
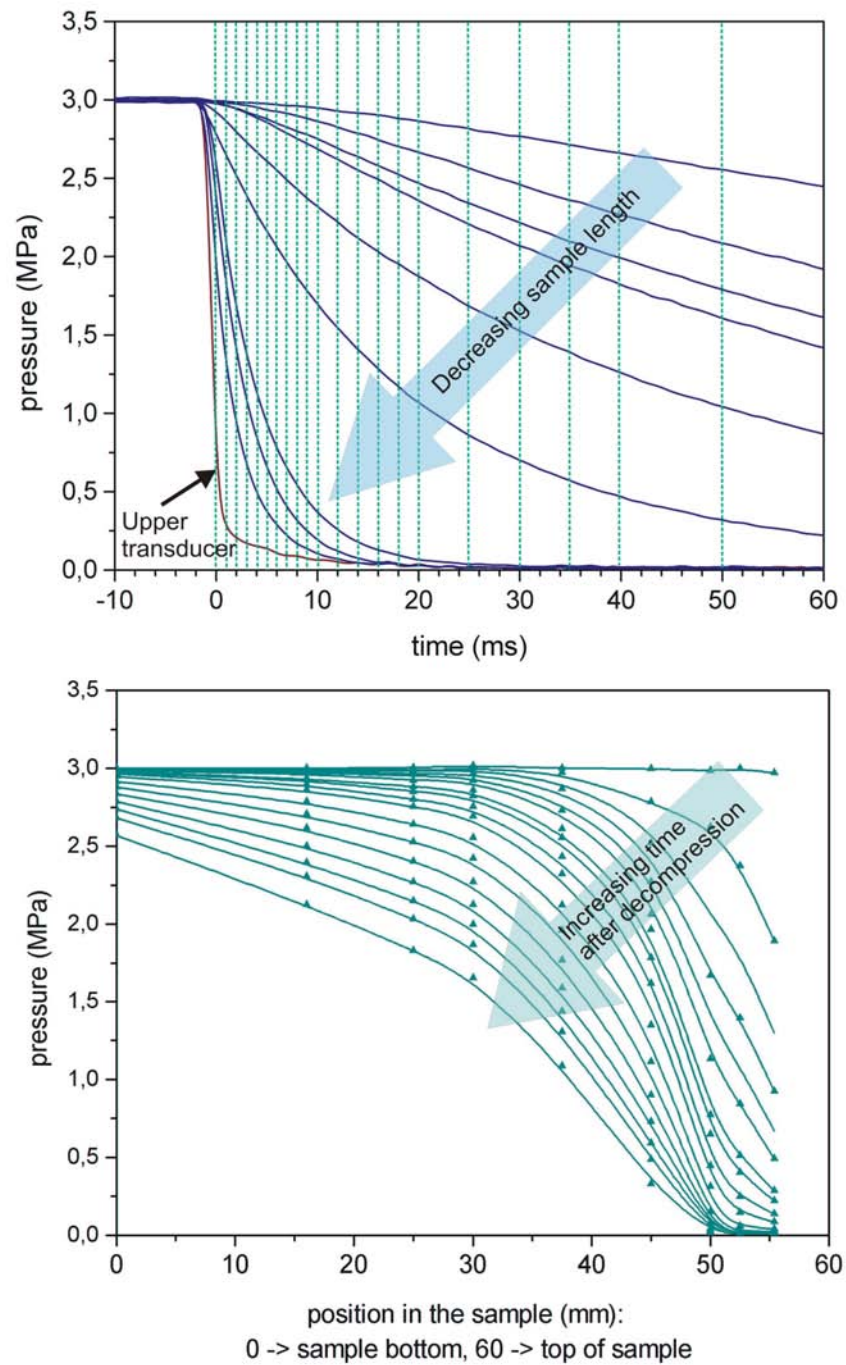
Figure 5.6: How to obtain a pressure profile from pressure drop curves. Top: Pressure drop curves of a shortened sample (MUZ 2001 C). All experiments started at 3 MPa initial pressure. The sample length changed from 60 mm to 44, 35, 30, 22.5, 15, 10, 7.5 and 4.6 mm. The pressure values at the marked time steps (dashed lines) were excerpted out of the recordings. Bottom: The pressure profile over the sample could be reconstructed by assigning each pressure drop curve to a location within the sample. The pressure evolution at this points (marked) is given by the transposed values of the pressures excerpted from the upper plot.

5.2.2 Results

The method was successfully tested at an andesitic sample from Merapi Volcano (Indonesia) with an open porosity of 13.8 vol.%. Subsequently four samples of Unzen dacite were investigated. The samples derived from the sets 2000 F (33.8 vol.%), 2000 G (33.0 vol.%), 2001 C (20.8 vol.%) and 2000 D (13.3 vol.%). All experiments were performed at an applied pressure of 3 MPa. A Montserrat pumice sample should be investigated at 2 MPa applied pressure, but at several sample lengths a partial fragmentation of a few millimeters occurred and thus hindered a reconstruction of the pressure profile.

Figure 5.7 shows the obtained pressure profiles along the Unzen dacites. The plots were arranged with increasing porosity. For a better comparison of the profiles, the curves at 2, 8 and 20 ms after decompression onset were marked blue in each plot. The speed at which the pressure drop migrates through the sample becomes faster with increasing porosity. The wobbling at the profiles of sample MUZ 2000 D is supposed to be artificial, it may result from a small gas leakage during the experiment at the sample length of 25 mm. The curvature of all pressure profiles is strongest close to the sample surface and shortly after decompression onset.

Comparison of measured and calculated pressure curves

The experimentally derived pressure profiles were compared to numerically modelled pressure profiles based on a 1D transient filtration code. Hereby a non-linear friction term is taken into account to describe the rapid filtration processes. The code was developed by Dr. Oleg Melnik (Moscow State University) to analyze the experimental data gained with the permeability setup at the fragmentation apparatus (*Mueller et al.*, 2005). A major difference of this setup compared to the setup used in this study consists in a medium sized gas volume below the sample, which is in pressure equilibrium with the sample before decompression. During the experiment the time the gas needs to filtrate through the sample is recorded. This leads to clearly longer time spans of the pressure drop curves. In contrast, the setup used in this study contains no gas below the sample.

Figure 5.8 (left) shows the pressure profiles along a sample with 30 % porosity, modelled with the above mentioned 1D filtration code. During the first 0.15 s the dis-
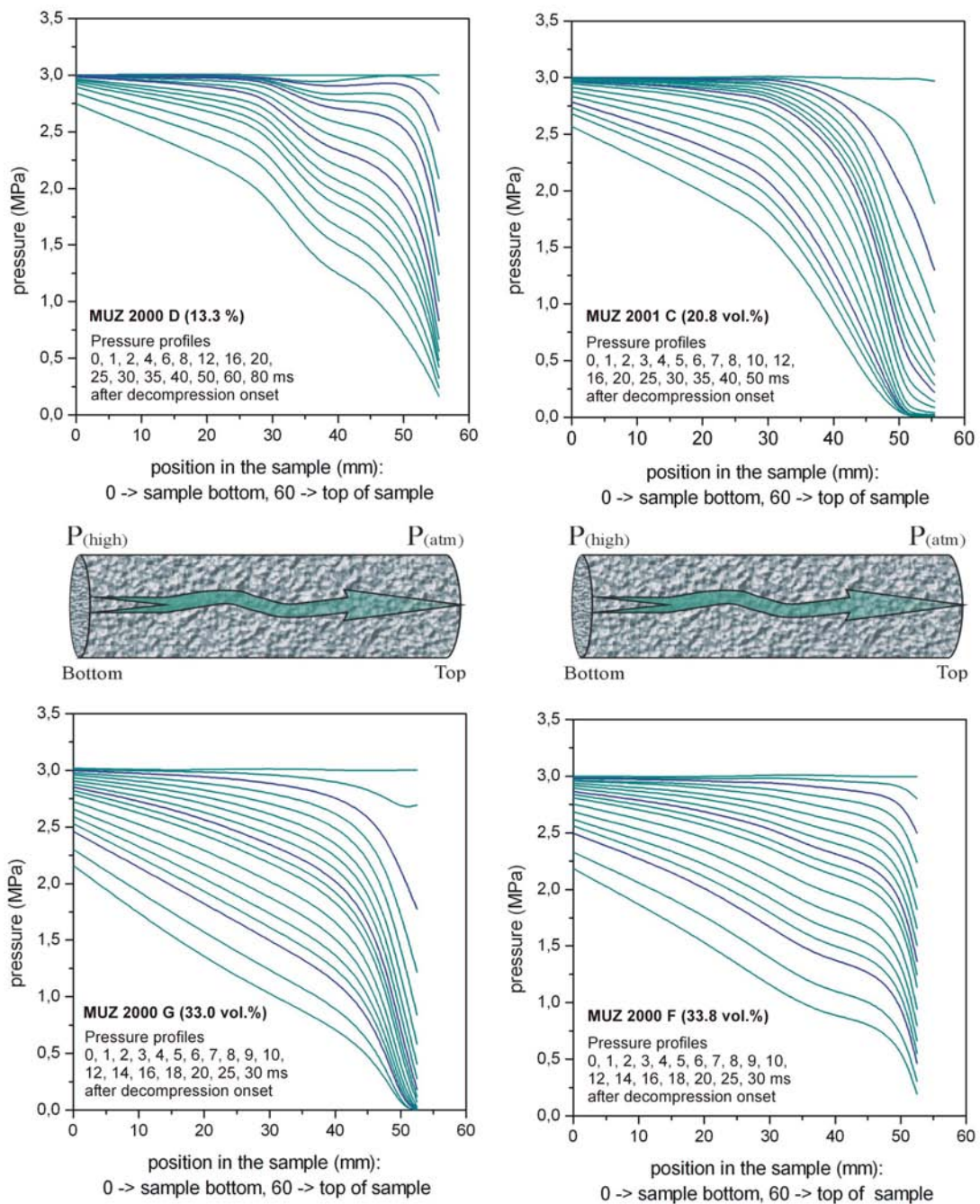
Figure 5.7: Pressure profiles over four dacitic samples from Unzen. The open porosity of the samples increases from 13.3 vol.% at the upper left plot to 33.8 vol.% at the lower right plot. For a better comparison the profiles 2, 8 20 ms after decompression onset were marked blue in each plot.
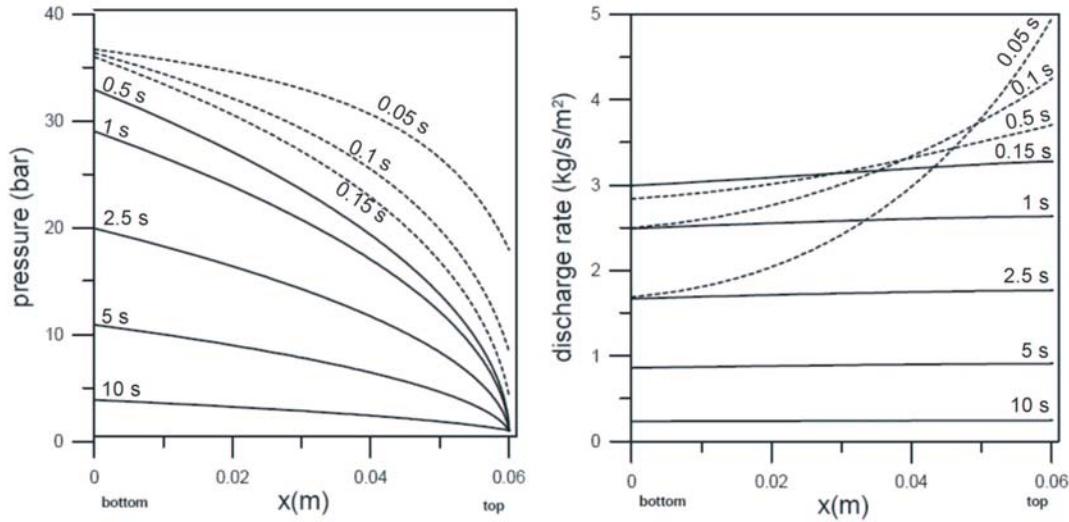
Figure 5.8: The pressure evolution within a porous sample (30 %), modelled with a 1D transient filtration flow code (left). The right diagram shows the numerically derived discharge rate for this sample. It has to be noted that a volume below the sample, containing pressurized gas, was implemented in the numerical model *(taken from Mueller et al. 2005)*.

charge rate at the top of the sample was found to be much higher than at the bottom (Fig. 5.8, right). This leads to the sharp pressure drop close to the sample surface. Later, the difference in the discharge rate along the sample decreases as the system moves towards quasi-static conditions. As the discharge rate decreases, the resistance of the sample to gas flow decreases. This results in a decrease of the pressure gradient along the sample. As noted above, the numerical model contained a defined volume of pressurized gas below the sample. Therefore the time steps marked in diagrams of the experimentally (Fig. 5.7) and numerically gained profiles (Fig. 5.8) vary strongly. Nevertheless a similar change of shape could be observed at experimentally reconstructed pressure profiles. Shortly after decompression onset a strongly nonlinear, steep pressure evolution was found near the sample surface. With ongoing decompression a transition to quasi-static conditions could be observed. This was also observed at the pressure profiles of the four Unzen samples (Fig. 5.7).

In Figure 5.9 (left) the measured pressure drop curve of the Unzen sample MUZ 2001 C at 60 mm length is compared to the pressure drop calculated with the filtration code. The numerically derived curve agrees very well with experimentally gained
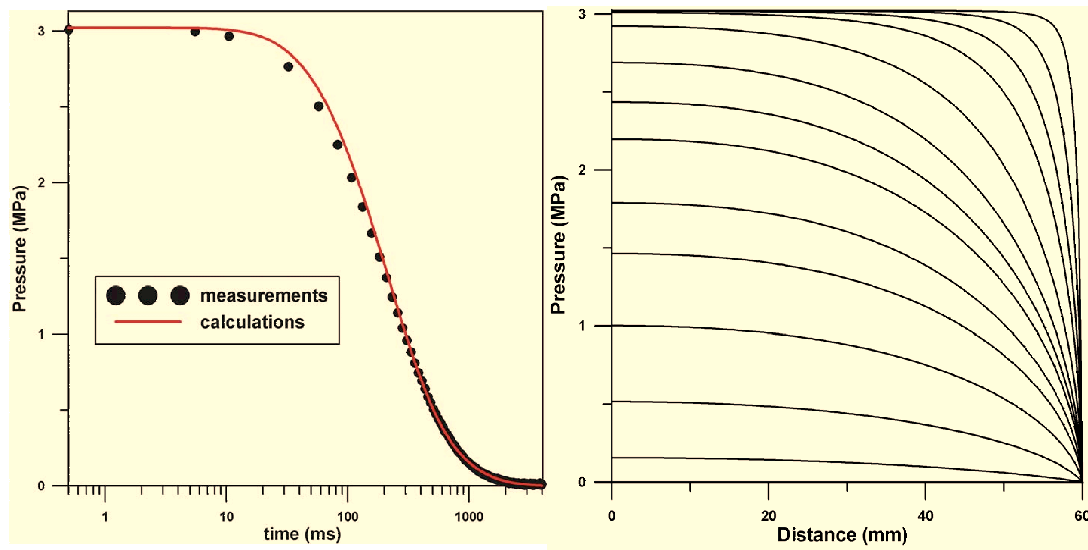
Figure 5.9: Best fit solutions and pressure profiles along the Unzen sample with 20.0 % porosity. Left: A comparison of the measured pressure drop curve of a sample at 60 mm length with the calculated pressure drop as described above. Right: Calculated pressure profiles for the same sample after 0.5, 2, 5, 10, 25, 50, 75, 150, 500 and 1000 ms after the onset of decompression *(modelled by Oleg Melnik).*

curve. In a next step, the pressure profiles for the same sample after 0.5, 2, 5, 10, 25, 50, 75, 150, 500 and 1000 ms after the onset of decompression were calculated (Fig. 5.9, right). At the initial stage of decompression the velocity of the gas phase is very high and, therefore, the sample friction is controlled by the non-linear term in the modified Darcy law. This leads to a sharp pressure gradient near the top of the sample. As the decompression proceeds the pressure gradient decrease.

A comparison of the measured and calculated pressure drop curves at different sample lengths of this MUZ 2001 C sample is shown in Figure 5.10. At short sample lengths the pressure dropped faster in the experiments than predicted by the theoretical calculations. Hence it can be concluded that there exists a critical sample length, beneath which the permeability of a sample starts to increase with shorter sample length. This is supposed to affect the fragmentation behavior of a sample; for instance it is one parameter controlling the thickness of the fragmentation layer.
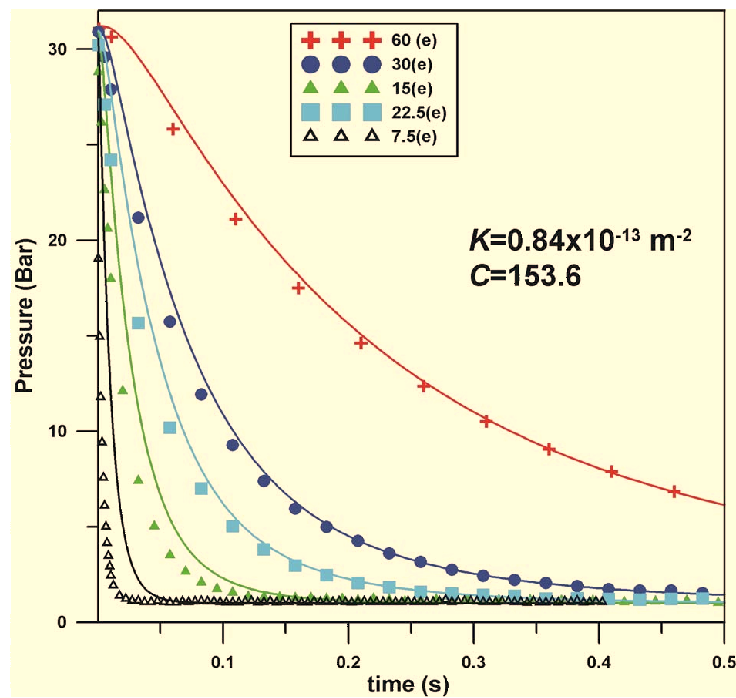
Figure 5.10: Comparison of the measured and calculated pressure drop curves at different sample lengths. The solid lines represent the calculated, the single symbols the measured data. All curves were calculated using constant parameters of K and C, with K being the linear permeability coefficient and C being the nonlinear correction coefficient due to rapid gas flow. For short samples the permeability increases and thus the pressure drops faster in the experiments compared to the theoretical calculations *(modelled by Oleg Melnik).*

5.3 Fragmentation profile along a sample at rapid decompression

Further experiments with different sample lengths were conducted above the fragmentation threshold. This set of experiments was aimed to investigate the fragmentation speed profile along a sample undergoing a rapid decompression event. Hereby samples with three different lengths were analyzed. Firstly, the regular sample length of 60 mm, then 30 mm and 15 mm were used for fragmentation experiments at the same applied pressure. These experiments were carried out at Montserrat pumice samples, as this is one of the most homogeneous data sets, exhibiting only a small deviation due to natural inhomogeneities. In case a change of the fragmentation speed with respect to the sample length exists, it should be clearly detectable within this data set. Variations of the fragmentation speed with the sample length should be most pronounced, around the threshold at a low energy density. Therefore all experiments to test the relationship between fragmentation speed and sample length were performed at 4.0 MPa and 7.5 MPa representing an energy density of $(2.6 - 4.9) \cdot 10^{-6}$ J/m^3. A first fragmentation initiation was observed around 2.5 MPa and the threshold of Montserrat pumice was determined to be 3.0 - 3.5 MPa or $(2.0 - 2.3) \cdot 10^{-6}$ J/m^3.

The experiments yielded for same pressure values coincident fragmentation speed values (Fig. 5.11). No influence of the sample length could be observed. Therefore it can be concluded that the fragmentation speed remains constant over the entire sample, assuming a homogeneous sample.

This result implies direct applications for the modelling of fragmentation events at a volcanic system. The layer-by-layer fragmentation process seems to be a self sustained mechanism. As long as the boundary conditions (pressure difference, porosity) do not change, the fragmentation due to vesicle bursting will propagate at constant speed. In contrast, fragmentation based on an unloading wave will attenuate as the unloading wave looses energy due to viscous dissipation and fracturing of the rock. The difference between the both mechanisms is the source and the way, the energy is applied to them. In the following a body with constant porosity and pressure is assumed. The fragmentation due to unloading is fed by fixed energy applied to the process once at its origin, this energy is consumed by the propagation itself and e.g. dissipation.
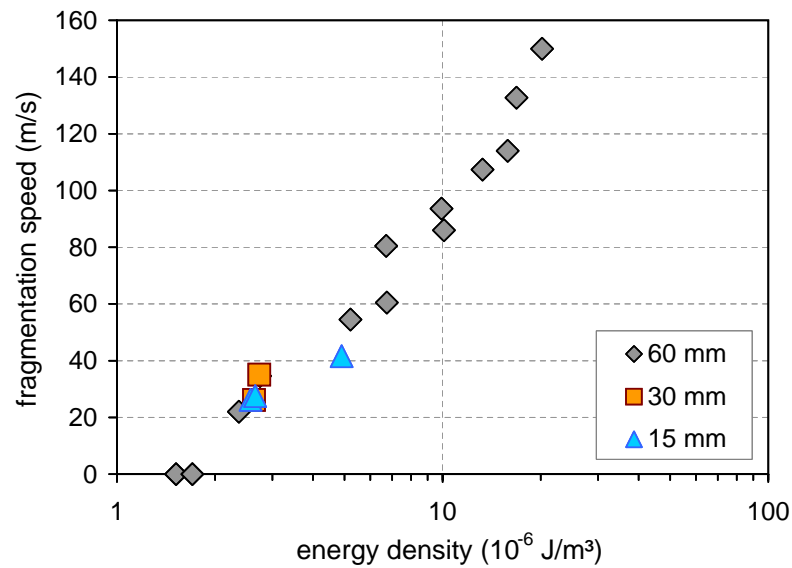
Figure 5.11: Fragmentation speed results of Montserrat Pumice (67 % open porosity) at different sample lengths of 60, 30 and 15 mm. Apparently the fragmentation speed is independent from sample length, thus the fragmentation speed remains constant over the entire sample.

The fragmentation attenuates and finally ceases. The layer-by-layer fragmentation is, once initiated, fed by the energy (gas pressure in vesicles) within the body, in which it propagates. In other words, the propagation process has no feedback to the energy driving it, the energy available for fragmentation remains constant. Effects like frictional heating do not affect this mechanism, as these are syn-fragmentation effects. If the energy provided by pressurized gas in the vesicles of the body is higher than the energy needed for fragmentation and frictional heating, the fragmentation will propagate at constant speed through the body. A change of the physical properties of the body is needed to cease the process.

Chapter 6

Implications for volcanic fragmentation

During a dome collapse or a sector collapse of a volcanic edifice, vesicular magma, pressurized due to lithostatic load and volatile diffusion, is exposed to rapid decompression. It depends on the properties of the magma whether a fragmentation occurs, leading to an explosive event. Dome lavas, for instance, are highly viscous and relatively degassed. (*Murase and Melson*, 1985; *Anderson et al.*, 1995; *Sato et al.*, 1992). At Unzen dacites of the recent eruption water contents of 0.25 - 0.5 wt. % were measured (*Kusakabe et al.*, 1999), Montserrat pumice clasts from the 1997 Vulcanian explosions contained 0.2 - 0.6 wt.% of water (*Harford et al.*, 2003).

A fragmentation will occur if the tensile strength of the magma is exceeded by any mechanism explained in chapter 1.2. The tensile strength of solidified andesite lavas has been estimated to be 10 - 20 MPa (*Self et al.*, 1979; *Fink and Kieffer*, 1993). Fracture toughness values ranging between 0.3 - 1.5 $MPa\sqrt{m}$ were determined for Unzen dacites in this study. They correspond to tensile strengths of 1.9 - 10.4 MPa (chapter 2.4).

In the following, several collapse and eruptions scenarios are introduced. They are based on field observations and on results of the fragmentation analysis of vesicular magma in this study. Most of the introduced scenarios can occur combined during one eruptive cycle. The discussion of these scenarios is preceded by a section dealing with a very interesting field observation: a porosity layering, which bears direct implications for the proposed collapse models.

Figure 6.1: Rock features observed at the endogenous dome of Unzen Volcano. (a) A block with 5-10 cm thick parallel layers of varying porosity. The layering may result from an internal shearing parallel to the conduit wall. In the uppermost layer (at the right-hand side of this picture) a 8 cm large enclave with a pressure shadow can be seen. The crack running through all layers in an angle of about 30° - 45° results from a subsequent event later than the layering, e.g. a cooling effect or shearing after the lava was solidified (or highly viscous). (b) This picture shows a porous area most likely generated by a cavitation process.

6.1 Porosity layering

During two field campaigns at Unzen Volcano a porosity layering in large blocks of the pyroclastic flow deposits as well as on parts of the endogenous dome could be observed. Zones with high porosity may either be areas, that were somehow protected from bubble collapse processes or are the result of a late gas exsolution event. *Smith et al.* (2001) mentioned cavitation, triggered by shearing of highly viscous magma as further possibility for their origin. Pressure shadows behind enclaves and shear fractures were found in large blocks of the pyroclastic flow deposits and at dome material (Fig. 6.1), supporting the notion of shear-driven cavitation. Finally, autobrecciation of large blocks during magma extrusion or slow flowing of the lobes is yet another process that could give rise to heterogeneously layered blocks. The zones of high porosity define bands, which appear to be caused by internal shearing parallel to the conduit wall during magma ascent (*Tuffen et al.*, 2003; *Gonnermann and Manga*, 2003; *Kueppers et al.*, 2005a; *Kennedy et al.*, 2005). Banded blocks provide information on the internal structure of the dome, and as a result, the dispersion of a fragmentation wave inside such a layered medium needs to be considered in dome models.
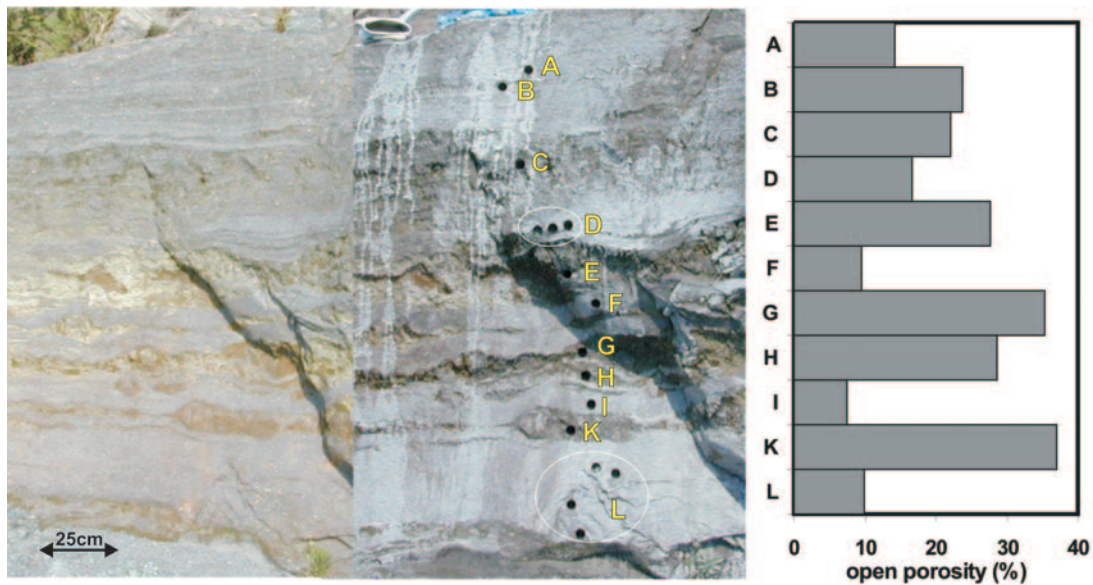
Figure 6.2: The two photos show the same large layered block in the pyroclastic flow deposits of the 1990-1995 eruption of Unzen Volcano before and after drilling. A portable diamond drill device was used to core samples out of the block to analyze the density variation and open porosity, respectively. The diagram at the right-hand side shows the porosity variation of the layers in the block from top to bottom, determined by helium pycnometry.

Samples were drilled out of eleven layers of a large block with layered porosity variation (Fig. 6.2). Density and open porosity of these samples were analyzed using a helium pycnometer. The density values range from 1.63 g/cm^3 to 2.37 g/cm^3 over the distance of several decimeters, according to an open porosity variation from 7.6 vol.% up to 39.0 vol.% (Fig. 6.2, right). Hence these values cover the larger part of the porosity bandwidth observed in the deposits and at the dome after the last eruptive activity, which ranges from 3 vol.% to 39 vol.%, not including breadcrust bombs (chapter 2.2.1; Fig. 6.4).
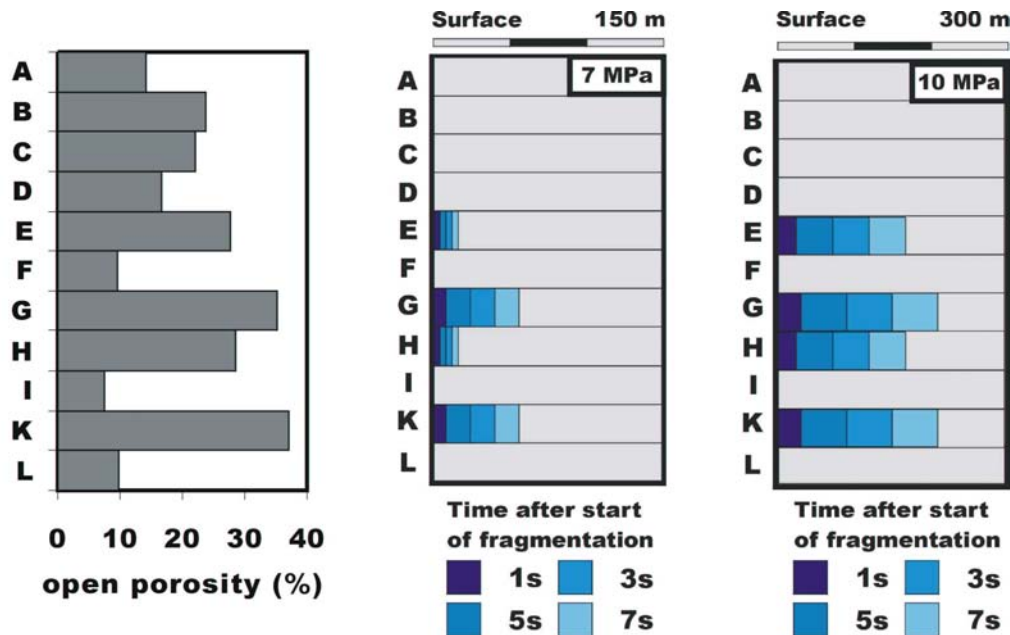
Figure 6.3: The porosity variation of the layered block (left) was used as a model to analyze the threshold and the speed distribution in a layered medium. At a pressure difference of 7 MPa four layers start to fragment (middle). At layers E and H, the threshold is only slightly exceeded, resulting in a very slow fragmentation speed. At layers G and K, the fragmentation propagates in 7 sec 60 m into the medium. At a pressure difference of 10 MPa the same four layers as before fragment (right). In this case, the threshold of all layers is clearly overcome. After 7 sec the fragmentation wave has travelled 210 m into the most porous layers G and K and 160 m into the still highly porous layers E and H. The threshold of layers B and C is reached, but not overcome.

6.2   Fragmentation behavior of a layered medium

Field evidence showed that the endogenous dome and the dome lobes of Unzen contain areas and layers with differing porosity. As observed in the fragmentation speed and threshold experiments of this study, the influence of porosity on the fragmentation behavior is large. Thus porosity changes in the dome must be taken into account as a first order factor in eruption models.

The investigated layered block described above (Fig. 6.2) was used as a model for a possible layering inside extruded dome lobes or magma in the upper conduit of Unzen. The fragmentation behavior at several overpressure situations was analyzed for this block, using the fragmentation threshold and speed values obtained for Unzen dacites (chapter 4.4).

First, the response of that block to a pressure differential of 7 MPa was evaluated (Fig. 6.3, middle). At the four most porous layers the threshold is overcome and they start to fragment. The manner in which the fragmentation wave travels along the layers into the assumed dome is represented by bars for 1 sec, 3 sec, 5 sec and 7 sec. Within layers E and H the pressure is only slightly above FT, therefore they fragment very slowly. Only the two most porous layers G and K are clearly above the fragmentation threshold. In these layers the fragmentation wave runs within 7 sec 60 m deep into the medium, assuming steady conditions.

The right diagram of Figure 6.3 shows the fragmentation behavior at a pressure difference of 10 MPa. As before, only at the four most porous layers E, G, H and K a fragmentation is initiated. But in contrast to the situation at 7 MPa, here the threshold of all four layers is clearly exceeded. The fragmentation speed in all four layers is > 20 m/s and thus the fragmentation front propagates in 7 seconds 160 m along the layers E and H, in the higher porous layers G and K even 210 m. In the medium porous layers B and C the internal pressure reaches the threshold, but FT is not overcome. These layers therefore should be in an unstable and weak condition and any further external perturbation may initiate a fragmentation or collapse.

Some estimates were made for initial pressure of gas inside the vesicles of magma in a dome or cryptodome. The excess gas pore pressure inside the dome lava of 1991 Unzen volcano eruptions was estimated to be several MPa (*Sato et al.*, 1995). The hydrostatic pressure drop caused by the 18 May 1980 landslide of Mount St. Helens leading to a lateral blast, was estimated to up to 20 MPa (*Eichelberger and Hayes*, 1982).

The observed density distribution of the eruptive products of the 1990 - 1995 eruption at Unzen Volcano (Fig. 2.4) allows to constrain the eruption style during that time. In Figure 6.4 the measured field density values are recalculated to the equivalent open porosity distribution. For the conversion a mean matrix density of 2.56 g/cm^3 was assumed for all samples but the breadcrust bombs, here a value of 2.22 g/cm^3 was used. The porosity ranges affected by fragmentation, if exposed to a rapid decompression of 5, 7, 10 or 20 MPa are indicated (Fig. 6.4).

At a pressure difference of 5 MPa, only the breadcrust bombs contain enough energy to be explosively erupted, none of the investigated dome magma tends to frag-
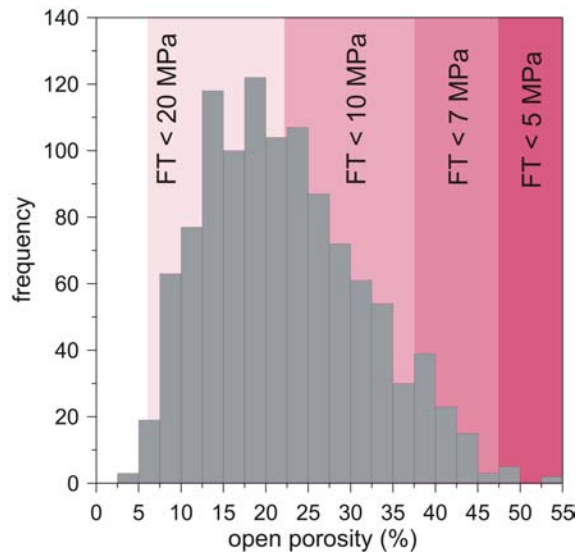
Figure 6.4: Porosity distribution of the 1990-1995 eruptive deposits of Unzen volcano (converted from Fig. 2.4). The areas that will undergo a fragmentation event, exposed to an initial pressure difference of 5, 7, 10 and 20 MPa are indicated.

ment. At 7 MPa most of the magma with porosity higher than 37 vol. % will start to fragment. For a pressure difference of 10 MPa, the fragmentation threshold is around 22 vol. % open porosity, this would be sufficient to initiate a fragmentation in nearly half of the analyzed samples. A landslide of the same dimension as the one causing the lateral blast at Mount St. Helens, would have had similar consequences at Unzen, as at a rapid decompression of around 20 MPa, almost all observed samples at the Unzen deposits would have been disrupted leading to a vigorous explosive event.

Fig. 6.4 shows clearly that most of the erupted material during the last period of activity at Unzen was too less vesicular and therefore not energetic enough to cause more major explosive events. Thus the major activity during the 1990-1995 eruption consisted in quiescent extrusive behavior as exogenous and endogenous dome growth, accompanied by Merapi-type block-and-ash flows and only few explosive events.

6.3   Dome collapse events

In the following section the implications of this layered model to several dome collapse scenarios are discussed, in special consideration of the last period of activity of Unzen volcano. The 1990 - 1995 eruption of Unzen was relatively quiet and non-violent compared to other dome-forming volcanoes as Soufrière Hills Volcano, Montserrat (*Young et al.*, 1997; *Sparks and Young*, 2002). Nevertheless, dome collapse events frequently occurred, leading to pyroclastic flows.

The magma erupted at Montserrat is, in general, more porous with a higher total fraction of pumices, whereas the magma of Unzen is relatively dense because it degassed very efficiently during ascent and emplacement. Thus, in general, the high density and the reduced explosivity at Unzen is in good agreement with the experimental results documented in this study. Specifically it is consistent with the observation, that the energy needed to fragment dense parts of the extruded lava lobes or the upper conduit of Unzen was too high to have been achieved by internal overpressure (Fig. 6.4). The result was, that most pyroclastic flows were triggered by gravitational dome collapse events, and only few small volume Vulcanian eruptions occurred.

In some cases puffs of ash were noted just below the resulting collapse scar, directly preceding the crumbling of the blocks (*Sato et al.*, 1992; *Ui et al.*, 1999). This phenomenon may be interpreted as a locally restricted fragmentation event. Due to the internal pressure and maybe additional cooling tensions, the fragmentation threshold of a highly porous area or layer within the dome may be reached and the layer fragments (Fig. 6.5). After a small fragmentation event due to a locally restricted overpressure situation, the overlying material becomes gravitationally destabilized and starts to crumble, inducing a pyroclastic flow. Thus, the fragmentation of a small but highly porous layer may be sufficient to initiate a pyroclastic flow. The fragmentation might be arrested by a thinning out of the porous layer.

Compared to landslides, dome collapse events can last for a long time, even several hours or a day, consisting of different violent events. This happened for example during the last major dome collapse event at Montserrat in July 2003 (*Carn et al.*, 2004). Also the large pyroclastic flow events in June - September 1991 and March - June 1993 at Unzen lasted at least several hours and consisted of a series of single events (*Nakada*
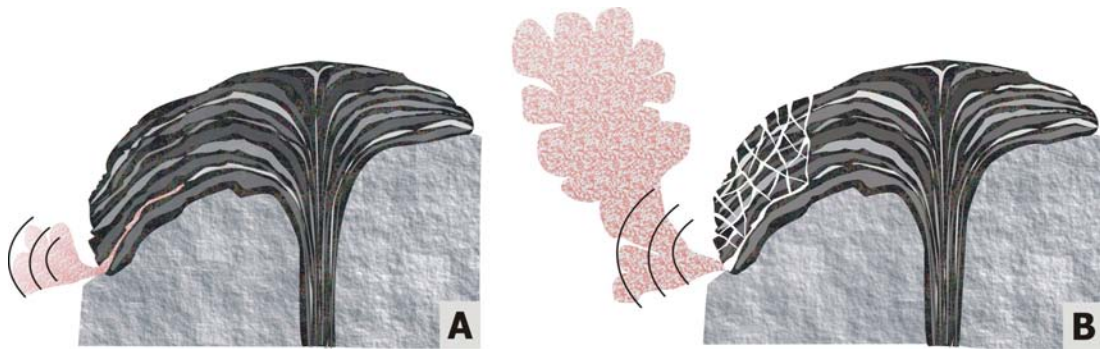
Figure 6.5: A dome collapse scenario due to the fragmentation of a highly porous layer. (A) A highly porous layer within the dome lobe fragments due to the internal overpressure. (B) The fragmentation of the porous layer destabilizes the overlying part of the dome lobe causing it to collapse.

et al., 1999). At this, a fragmentation may be triggered by the major or minor (gravitational) dome collapse. The collapse removes the outer parts of the dome, exposing a new surface of higher pressurized to ambient pressure conditions. For highly porous areas at the newly created surface, the fragmentation threshold may be exceeded and a fragmentation process is initiated (Fig. 6.6). The reduction of lithostatic load associated with dome collapse increases additionally the relative overpressure inside vesicles and thus enhances the likelihood of driving more fragmentation and collapse events. This may be one mechanism to keep a collapse and pyroclastic flow event ongoing for several hours. The most violent and destructive pyroclastic flows at Unzen occurred at the end of the series of events (*Nakada et al.*, 1999; *Fujii and Nakada*, 1999). This seems reasonable, based on the mechanism proposed here. The fragmentation events and the associated pyroclastic flows become more violent towards the central part of the dome as the pressure differential which drives the fragmentation process increases. At Montserrat, jets coming out of the rock face were observed after big dome collapses (*R. Herd, pers. comm.*). These jets can be interpreted as explosions caused by the collapse and probably related to decompression of small locally restricted areas, which is a good evidence for the proposed mechanism.
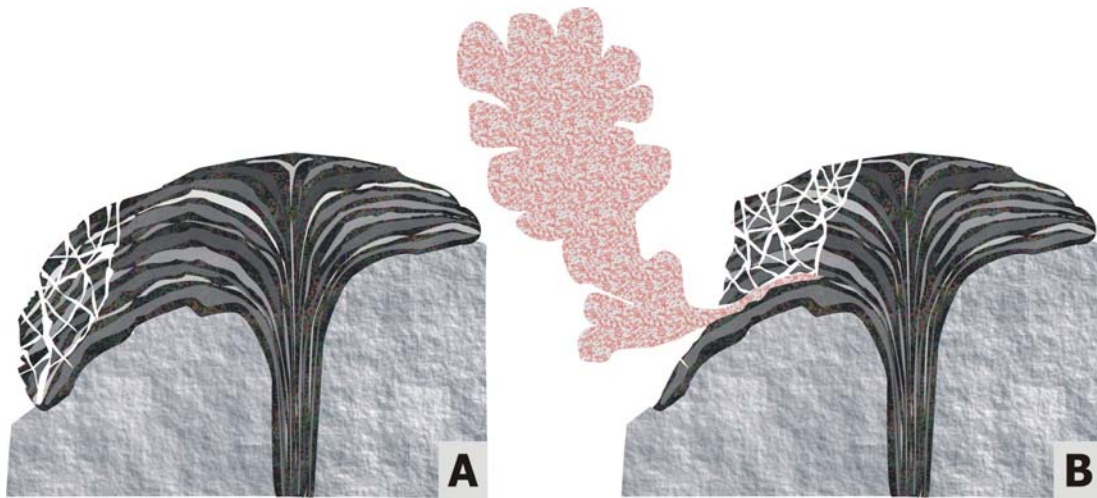
Figure 6.6: Dome collapse scenario amplified by a fragmentation event. (a) A small gravitational dome collapse takes place and exposes more highly pressurized magma to the atmosphere. (b) On the newly exposed surface the threshold is now overcome for a highly porous layer and the layer fragments. This fragmentation triggers the collapse of another part of the dome.

6.4 Vulcanian events

Observations of numerous dome forming eruptions exhibit extended periods of effusive dome growth, with intermittent short-lived explosive activity. During the effusive phase, degassed magma builds up a dome, while the exsolved volatiles filtrate through the permeable dome to the atmosphere (*Eichelberger et al.*, 1986; *Melnik and Sparks*, 1999). Field observations as well as models of dome growth indicated that considerable overpressure, defined as pressure above local lithostatic pressure, can develop in such lava domes (*Sato et al.*, 1992; *Fink and Kieffer*, 1993; *Sparks et al.*, 1998; *Melnik and Sparks*, 1999, 2002). Gas exsolution increases the viscosity of the magma by orders of magnitude and triggers crystallization, which can also increase the pressure in the upper parts of the conduit. Such overpressure at the base of a growing dome may reach several MPa and is dissipated by the escape of gas through the porous structure of the dome (*Woods et al.*, 2002).

The pressure changes associated with a dome or sector collapse may be sufficient to initiate a Vulcanian explosion (*Woods et al.*, 2002). For example, all Vulcanian explosions during 1997 at Soufrière Hills Volcano, Montserrat, were preceded by large

dome collapse events (*Druitt et al.*, 2002) and also the Vulcanian explosions at Unzen Volcano occurred after large pyroclastic flows and a landslide.

A dome collapse event may occur as indicated in Fig. 6.6, becoming increasingly vigorous with duration, as due to the retrograde moving new surface of the volcanic edifice more and more highly pressurized magma is exposed. Again, for a few highly porous layers on this newly exposed surface the threshold is overcome and these layers fragment. This fragmentation triggers the collapse of another part of the dome (Fig. 6.6, Fig. 6.7b). In case the fragmentation is not stopped by the punching out of the layer or a density increase within the layer, it may reach the conduit. This leads to another large collapse and the opening of the conduit. If the pressure difference is high enough, a fragmentation is initiated within the highly viscous conduit, usually leading to a Vulcanian explosion (Fig. 6.7).

Additional changes of the properties of the uprising magma, e.g. due to slight variations in melt composition, crystal content or water, might generate variations in the degree of vesiculation at a constant depth level. Such variations might destabilize the fragmentation level in the following manner. A porosity decrease during an eruption reduces the gas expansion energy available for the fragmentation process and the ejection of the fragmented particles. One consequence could be a decrease in the fragmentation speed in the ascending magma and a rise of the fragmentation level. A porosity increase could result in the opposite effect, a higher propagation speed of the fragmentation front, a higher acceleration of the pyroclasts and moving of the fragmentation level down the conduit. In combination these effects could lead again to a pulsation, or, even cessation of the eruption.

6.4.1 Vulcanian events at Unzen

Two Vulcanian explosions at Unzen Volcano occurred at an early stage of the eruption during the period of highest effusion rate. After rapid inflation of the summit area, first dome growth started on 20 May 1991. Large pyroclastic flow events took place on 3 and 8 June 1991, both associated with dome collapse events. The latter resulted in a collapse of 2/3 of the dome, leading to a Peléan pyroclastic flow (*Nakada et al.*, 1999). The removal of the upper part of a dome complex exposed magma with a higher pore
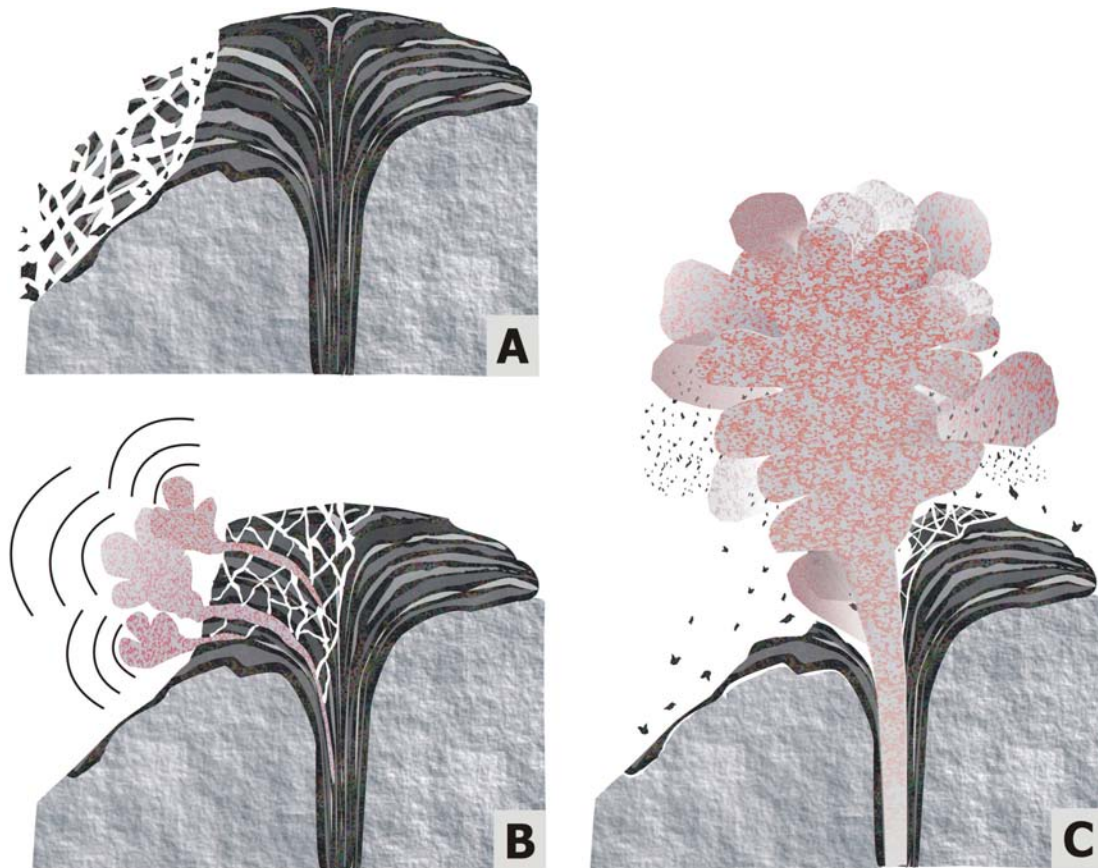
Figure 6.7: A possible dome collapse scenario, amplified by a fragmentation event, leading to an explosive eruption. (a) A small gravitational dome collapse takes place and exposes more highly pressurized magma to the atmosphere. (b) On the newly exposed surface the threshold is overcome for a few highly porous layers and these layers fragment. This fragmentation triggers the collapse of another part of the dome. If the fragmentation is not stopped by the punching out of the layer or a density increase within the layer, the fragmentation front may reach the conduit area. (c) A large dome collapse exposes highly pressurized magma to the atmosphere. This allows to fragment high to mid porous magma, and the fragmentation propagates down into the conduit. An explosive event takes place, it depends on the magma properties within the conduit whether a Vulcanian or Plinian event occurs.

pressure due to the lithostatic pressure. The resulting pressure gradient at the newly created surface may therefore has been high enough to fragment the porous magma within the vent. If this occurred, a fragmentation wave could start to propagate in this porous zone down the conduit, leading to a Vulcanian event (Fig. 6.7).

On 11 June another Vulcanian event took place, which was not accompanied by large pyroclastic flows. Nevertheless, it is very likely that this event was triggered or at least favored by the removal of parts of the overlying dome by the preceding collapse event (8 June). Similar observations were made and successfully modelled at Soufrière Hills Volcano, Montserrat. A sub-Plinian explosion occurred a certain time after a big collapse, implicating unloading of the magma in the conduit as a causative key factor (*Melnik and Sparks*, 2002). A very similar mechanism leading to the 11 June Vulcanian event at Unzen is proposed here. Magma that was still volatile rich started foaming in the conduit until the gas pressure overcame the yield strength of the magma (equivalent to the fragmentation threshold) and an explosion occurred. This event may have been the result of an isolated magma phase that was ascending slightly faster than the mean ascent rate of most extruded magma. This ascending magma phase seemed to have a lower viscosity than the average extruded lava either due to a lower total crystallinity or, more probably, due to a higher water content or higher temperature. The magma may have ascended through fissures or shear cracks between the conduit walls and the host rock (Fig. 6.8). A slightly inclined conduit can be deduced from the location of the hypocenter region of volcanic tremor and LF earthquakes, which are related to the magma movement (*Nakada et al.*, 1999; *Umakoshi et al.*, 2001). The inclination of the conduit may have eased the rise of bubble-rich magma to the top of the conduit, similar to the idea proposed by *Lane et al.* (2001) for bubbly flow in inclined tubes. The location of the vent of this eruption, at the rim of the old crater, vertically above the inclined conduit supports this mechanism (Fig. 6.8) (*Nakada*, 1992). Since gas exsolution is less efficient at high ascent velocities, the water content in this magma remained higher than the mean water content of 0.25 wt.% at the initial stage of the eruption. This is confirmed by *Kusakabe et al.* (1999), who measured a higher water content in the Vulcanian bombs; 0.5 wt.% in the quenched rims and around 0.35 wt.% in the cores.

The Vulcanian explosion on 11 June was accompanied by shallow earthquakes, located 500 m below the surface (*Nakada et al.*, 1999). This may be the maximum
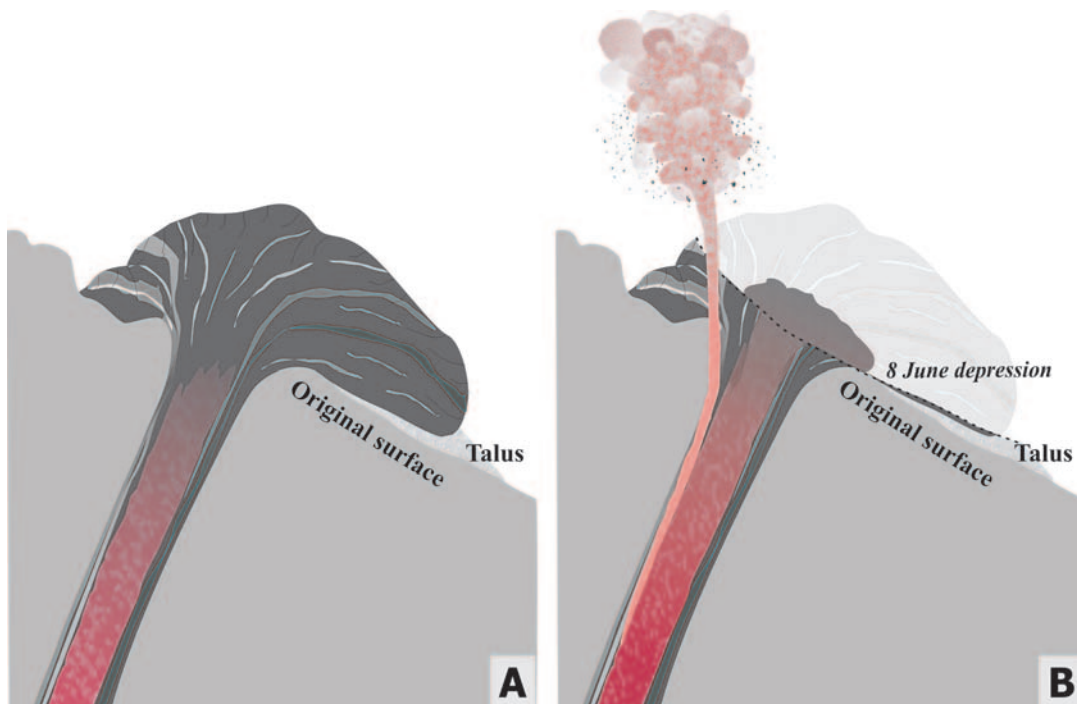
Figure 6.8: A dome complex, fed by an inclined conduit. This complex is similar to the structure of Unzen volcano in June 1991. The inclined conduit and a fractured dome structure may have eased the Vulcanian eruption on 11 June 1992. (a) The inclined conduit allowed highly mobile, bubble-rich magma to accumulate at the roof of the conduit. (b) A major dome collapse on 8 June removed the upper part of the dome. The bubble-rich magma ascended along the top of the conduit and opened a fissure to the surface. The fissure may has been generated by shearing and cooling processes.

depth reached by the fragmentation process. The lithostatic pressure at this depth is 10 MPa, assuming a magma density of 2.0 g/cm^3. This corresponds to the pressure of the explosion calculated by *Nakada et al.* (1999) from the vertical velocity of the projectiles. Besides the lithostatic pressure, the excess pore pressure has to be taken into account, as due to the high viscosity of the Unzen magma the bubble growth during depressurization is limited. *Sparks* (1978, 1994) pointed out that at high viscosities, on the order of 10^8 poise, an excess pore pressure of several MPa can be reached. Based on the viscosity and the water content of the Unzen dacite, an excess pore pressure of up to 5 MPa can be assumed. The experimentally determined fragmentation speed of the breadcrust bombs at around 10 MPa initial pressure difference is 40 - 50 m/s. *Woods et al.* (2002) assumed a fragmentation speed of 10 m/s for the Vulcanian events

at Montserrat, which seems to be very slow, taking into account the higher porosity of the ejecta at Montserrat. With the results of this study, the time needed for the fragmentation front to reach 500 m depth can be deduced to 10 - 12.5 seconds. The volume of the ejected material was estimated by *Nakada et al.* (1999) to be $3 - 6 \cdot 10^3$ m^3. As a first order approximation, this would represent a cylinder 500 m in length with a diameter of 3 - 4 m. There appears to be several different ways to stop the fragmentation process. Firstly, the fragmentation may loose momentum and slow down as the magma gradually becomes denser or less foamed. Secondly, a batch of foamed magma, whose volume might be restricted in some way, may be blown out completely and the fragmentation will cease quite sharply by entering the denser surrounding magma or wall rock. Further, the fragmentation may stop if the conduit becomes choked, because the volume of gas in the vesicles is insufficient to propel the pyroclasts out of the conduit. Finally, small scale "lateral fragmentation" at the sidewalls of the vent during a Vulcanian eruption may plug it up.

6.4.2   The 1997 Vulcanian eruptions at Montserrat

The recent eruptive activity at Montserrat Soufrière Hills Volcano included numerous vigorous explosions, most of them during the first phase of activity lasting from 1995 - 1999. Two major cycles of Vulcanian explosions occurred between August and October 1997. At both, the explosions started several hours after a major dome collapse event, which uncovered the conduit (*Druitt et al.*, 2002). Pyroclasts from this closely monitored 1997 Vulcanian eruptions of Montserrat provide an excellent data base to reconstruct conduit dynamics.

Characteristic dimensions of dome sections to collapse at Montserrat were found to be 200 m in height and $6 - 14 \cdot 10^6$ m^3 in volume, respectively (*Sparks et al.*, 2002). A collapse of this height will cause 4.7 MPa of overpressure, assuming 10 % porosity - a typical value for the dome forming magma at Montserrat (*Robertson et al.*, 2000). The results of this study indicate that a pressure difference of 3 MPa is sufficient to initiate fragmentation in the pumice, whereas more than 30 MPa is needed to fragment the very dense rocks. The overpressure estimated for the center of the dome prior to the collapse were around 5 - 10 MPa (*Robertson et al.*, 1998; *Druitt et al.*, 2002; *Woods et al.*, 2002). These values are consistent with recent models of conduit flows,

which included the effects of volatile exsolution and microlite crystallization in the ascending magma leading to high viscosities and hence a pressurization of the upper conduit (*Sparks et al.*, 1998; *Melnik and Sparks*, 1999). According to that, the residual water contents of 0.2 - 0.6 wt.% found in pumice clasts indicate minimum pressures of 1.1 - 3.7 MPa at the 1997 Vulcanian explosions. The residual water content of 1.8 wt.% of a sample from the sub-Plinian event 1996 implies a larger pressure drop of $\sim$ 20 MPa. Variable residual water contents in dome samples are consistent with pressure variations of up to 9 MPa in the lava dome interior (*Harford et al.*, 2003).

The experimental results of this study show that 10 MPa is a sufficient overpressure to fragment samples with 19 % or higher porosity. The fragmentation front moves downwards at a speed determined by the porosity of the magma and the magnitude of decompression.

Pumiceous material was found to represent 95 % of the explosive products (*Clarke et al.*, 2002). *Formenti et al.* (2003) observed a porosity range of 50 - 80 % at pumices derived by fallout and pyroclastic flows, with a mean of 63 %. Thus, the pumice investigated in this study, with a porosity of 67 %, can be regarded as representative for the conduit filling. Only about 5 % of the ejected products were poorly vesicular and derived presumably from the conduit walls. Figure 6.9a, b shows a possible cross section through the conduit of Soufrière Hills Volcano leading to the 1997 Vulcanian explosions, constructed by hand of the clasts, investigated in this study (chapter 4.4.2). The center consists of pumice, followed by the more dense stripy or banded pumices, closer to the conduit walls, where considerable shear processes take place. The transition from the pumices to the conduit walls is formed by the mid dense clasts, which were also found to be partially banded. The very dense clasts are regarded as representative for the dense conduit walls.

Since porosity varies within the conduit, the fragmentation front moves more rapidly in the pumiceous center than in the denser conduit lining. The fragmentation front is therefore not restricted to a single depth, but instead is deeper in the conduit center than in the margin and becomes increasingly concave (Fig. 6.9a, c). The different fragmentation surfaces in Figure 6.9a are calculated based on the approximation of a constant pressure difference of 10 MPa. The experimental data indicate that after 20 seconds the fragmentation front in the conduit center may be 1100 m deeper than in the more dense parts at the conduit walls. As a result, the fragmentation front preferentially ex-

cavates the high-porosity pumiceous magma in the center. Hypothetically, this could leave a pressurized conduit lining exposed to a lower- pressure gas-particle mixture (Fig. 6.9c). Consequently, the more dense magma of the conduit lining is exposed in addition to the vertical decompression at shallower depth to a horizontal decompression in greater depth, behind the fast moving fragmentation surface within the pumice. This denser magma could spall off, fragment laterally, and the conduit could partially implode. *Kennedy et al.* (2005) found evidence for lateral fragmentation within banded pumices and mid dense clasts. They observed predominantly vertical fractures in the phenocrysts of this clasts, parallel to the conduit flow direction, whereas the crystals in the pumices showed fractures perpendicular to this direction. Lateral fragmentation of relatively dense conduit lining may contribute to a pulsation or even cessation of an explosive event as follows: The ejection direction of the disrupted particle-gas mixture at lateral fragmentation is perpendicular to the ejection of the pyroclasts generated by the main fragmentation within the pumiceous center of the conduit. This leads to intense particle-particle interactions in the gas-particles mixture and thus reduces the ejection velocity. The majority of the clasts originating from horizontal fragmentation may catch up enough momentum by these collision to be ejected out of the conduit, but a smaller part may also drop down the conduit starting to burry the fragmentation surface. This all leads to an increasing pressure behind the fragmentation surface, which is equivalent to a reduction of the pressure difference driving the fragmentation process. Hence the fragmentation slows down or even stops, allowing the magma to refill the conduit. In the rising magma again bubble growth takes place and overpressure is built up due to viscous resistance of vesicles and microlite growth. If this overpressure exceeds a critical amount, fragmentation is again initiated. The cyclic activity of the 1997 Vulcanian explosions at Montserrat occurred at an interval of about 10 hours (*Druitt et al.*, 2002). The magma discharge rate during this time was very high, around 8 m^3/s (*Sparks and Young*, 2002), resulting in a conduit refilling of about 720 m. From the eruption volume data *Druitt et al.* (2002) calculated that the fragmentation front would have reached approximately 1400 m depth. Using the fragmentation speed data for a 20 second eruption, calculations reveal that the depth of the fragmentation front in the pumice could reach about 1500 m. This close agreement of the observed volume and the measured speeds supports the experimental data of this study.
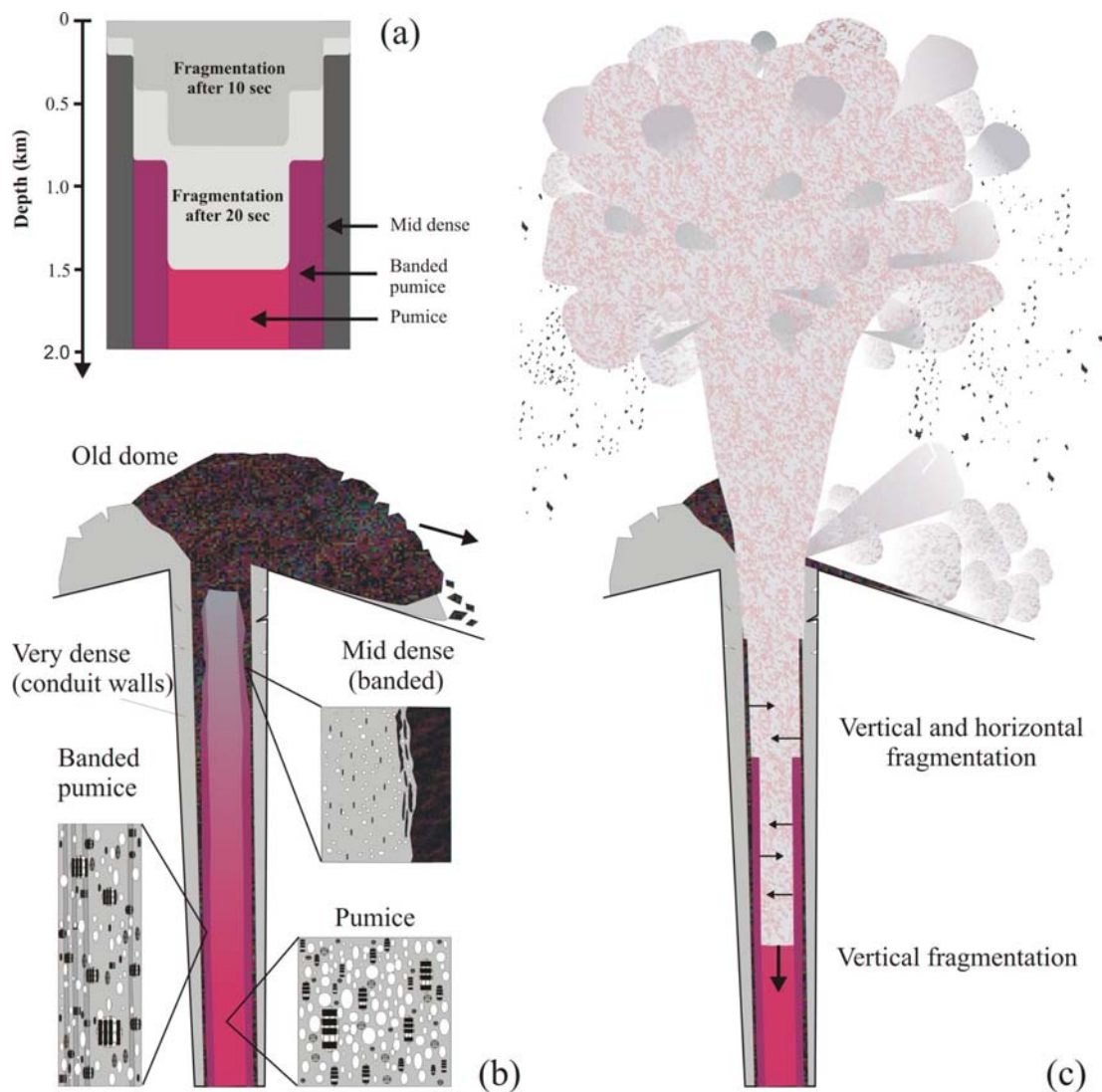
Figure 6.9: The less vesicular magma close to the conduit walls fragments slower than the pumice in the center of the conduit, leading to a strongly concave or in this model stepwise fragmentation surface (a). Here a constant pressure difference of 10 MPa is assumed. This bears significant implications to the mechanism of a energy density (10-6 J/m)Vulcanian explosion. (b) The great majority of the ejecta during Vulcanian events were found to be pumices. More dense material, as the banded pumices or the partially banded mid dense clasts are supposed to form the transition from the conduit filling to the conduit walls (b). After a dome collapse event the pressurized magma is rapidly decompressed and a fragmentation is initiated, running down the conduit. As the pumiceous center fragments much faster than more dense magma close to the conduit walls, a stepwise fragmentation surface is generated. Thus the pressurized conduit margin is exposed additionally to a horizontal pressure difference and a lateral fragmentation may be initiated, leading to a partial implosion of the conduit. This may result in a pulsation or even cessation of the explosive event (c).

Chapter 7

Conclusions

The elastic wave velocities of differently porous Unzen dacite samples were investigated with the use of a cubic multi-anvil press. The main results of this study show that porosity (density) and texture affect the elastic properties of samples at a given temperature. In particular, it can be stated:

Seismic velocities increase with pressure due to compaction and closing of microcracks. The Vp anisotropy decreases with pressure for the same reason. Mean P-wave velocities of 4.21 - 5.38 km/s and mean S-wave velocities of 2.20 - 3.15 km/s were obtained at a pressure of 100 MPa within the analyzed density range of 1.93 - 2.50 g/cm^3.

Increasing the temperature also leads to higher elastic wave velocities and lower anisotropies. This must be highlighted as the inverse behavior is documented for the majority of rocks. The effect may be linked to reduction of pore volume and further closing of microcracks due to reduction of cooling tensions. At 600 °C mean Vp values of 4.31 - 5.64 km/s and mean Vs* values of 2.20 - 3. 32 km/s could be determined.

The velocity anisotropy can be linked to the texture of the samples: Those with a high anisotropy show a pronounced shape-preferred orientation of phenocrysts and microcrystals, sometimes in addition to layering within the groundmass of the sample. Since the crystals are typically aligned parallel to walls of volcanic conduits, the velocity normal to the walls is likely to be reduced.

The data allows better estimates of the properties of silicic volcanic rocks at shallow depths within volcanoes, e.g. at conduit walls. These estimates are vital for computation of conduit models as well as the modelling of volcano seismic data, and may

lead to an improved analysis of precursor phenomena in volcanic areas.

The physical properties of magma within volcanic conduits and domes are crucial for modelling eruptions. This study comprises a detailed investigation of the fragmentation behavior (threshold and propagation speed) of differently porous sets of dacitic and andesitic samples derived from Unzen Volcano, Japan and Soufrière Hills Volcano, Montserrat, West Indies. The experiments were performed with a shock-tube based fragmentation apparatus and pertain to the brittle fragmentation process. The results show a strong influence of the open porosity and the initial pressure on the fragmentation behavior. The speed of fragmentation follows a logarithmic relationship with the pressure difference, the fragmentation threshold an inversely proportional power-law relationship with increasing porosity. In this study fragmentation speed values ranging from 15 - 150 m/s were observed for applied pressure differences of up to 40 MPa and open porosities from 2.5 - 67.1 %.

The expansion of the pressurized gas in the vesicles largely provides the energy driving the fragmentation process. The fragmentation speed results of all analyzed samples show a close relationship to the energy density (fragmentation energy standardized to volume). A logarithmical increase of the propagation speed was observed with the energy density as soon as the energy threshold of 2.0 ± 0.5 J/m^3 was exceeded. The fragmentation speed is independent from the origin and composition of the samples, proving the governing role of the energy to the initiation a propagation of fragmentation process.

Different fragmentation mechanisms were discussed and the layer-by-layer fragmentation due to vesicle bursting is concluded to be the main process responsible for the disintegration of vesicular rocks. The increased importance of fracturing due to the passing of the unloading wave after a rapid decompression could be proved for low porous samples. Further the influence of the sample's permeability on the fragmentation behavior was evaluated. It could be shown that a high permeability hinders the initiation of a fragmentation and reduces the propagation speed of this process at a certain energy density.

The fragmentation results were applied to the dome collapse events and Vulcanian events of the 1990-1995 Unzen eruption and the 1997 Vulcanian events at Montserrat. Large blocks with layers of various porosity were observed at the block-and-ash

flow deposits of Unzen Volcano and support the model that a dome and dome lobes consist of areas of differing porosity. In addition, the samples gained from Montserrat, allow to postulate a porosity gradient within a volcanic conduit, with low porous magma close to the conduit walls. A layered composition of a dome and dome lobes, respectively, may lead to the fragmentation of single layers, followed by the collapse of the overlaying sections. These events could catalyze gravitationally induced dome collapse events leading to vigorous pyroclastic flows and / or trigger a sector collapse followed by an Vulcanian event. A porosity gradient at the magma in the conduit leads to a concave shape of the fragmentation surface and facilitates lateral fragmentation of dense magma close to the conduit walls. Conduit implosion may to occur during most explosive eruptions and is likely to influence the cessation or pulsation of the eruption.

The slow magma ascent and extrusion rate at Unzen resulted in relatively dense extruded magma, as the magma could almost completely degas during the ascent. The low porosity of this magma causes a high fragmentation threshold of most material, which is too high for unassisted fragmentation. Therefore dome collapse events were the most abundant events of the 1990-1995 activity of Unzen Volcano, leading to numerous block-and-ash flows. Also the fragmentation-amplified collapse of dome lobes or parts of the dome are reasonable. This accounts especially for the long lasting collapse events with vigorous pyroclastic flows at the early stage of the eruption in June 1991, which were followed by minor Vulcanian events. Nevertheless a larger explosive event would have been possible, triggered by a landslide or a sector collapse of the dome.

Similarly to Unzen, the first phase of activity of the recent eruption of Montserrat is characterized by numerous dome collapse events leading to violent pyroclastic flows. As the magma extrusion rate was quite high during this phase, the extruded magma was higher vesiculated compared to the Unzen magma and thus a more violent evolution of the eruption activity took place. Large dome collapse events frequently caused Vulcanian events, and even two cycles of Vulcanian activity from August to September 1997 occurred. The calculations of the fragmentation depth, reached by this explosions yielded about 1500 m, based on the laboratory gained fragmentation speeds, which is in good agreement numerical models and observations.

In silicic volcanic systems the conduit seems not to be sharply defined. The conduit walls are more to be seen as a kind of transition zone between a hot, ductile and vesicular magma within the conduit and the host rock. The rocks forming this transition zone are assumed to be quite hot, but presumably below glass transition and react therefore solely brittle. Furthermore these rocks should be quite dense, compared to magma in the conduit, and heavily fractured due to the high shear strains this zone is presumably exposed to. The transition zone is less likely affected by a fragmentation event. Their rocks (magma as well as host rocks) are too dense to fragment due to pore pressure. The needed pressure difference is unrealistically high, for example an overpressure of 18 MPa would be needed to initiate the fragmentation of rocks with a porosity of 7.5 %. Nevertheless this material may be found in the deposits of explosive events, due to processes like conduit wall erosion or as remnant of dense lenses within more porous areas. Indeed, also fragmentation may take place, the most likely process fragmenting even this dense material is by lateral fragmentation, which may occur from a certain depth on behind a fast propagating fragmentation of highly vesicular magma at the center of the conduit.

The style and progression of an eruption is depending on the properties of this vesicular magma. If its fragmentation threshold can be exceeded, an explosive event may take place. Otherwise the magma is extruded quiescent in a dome forming eruption. The transition zone bears important implications on the one hand for the explosive event as a lateral fragmentation of a certain area may cause cessation or pulsation of the event, on the other hand for the propagation of seismic signals related to the eruption. Within this transition zone as well as the nearby host rock a decisive change of temperature and porosity can be supposed. This leads to a significant shift of the elastic wave velocities within this zone, sometimes resulting in trapped waves within this zone as observed for Montserrat. Especially the abnormal velocity increase with increasing temperatures has to be mentioned.

Thus implications for an overall view of a volcanic system are provided in this study, with the transition zone as the common link. The properties of the elastic wave velocities account for the for host rock as well as the transition zone and bear vital constraints for the interpretation and modelling of volcano seismic data. The results of the fragmentation experiments are applicable for dome rocks, the vesicular interior

of a conduit as well as the transition zone and contain important implications for the modelling of conduit processes. Together the results of this study may contribute to a refined understanding of processes typical for silicic volcanism. This may allow an improved analysis of precursor phenomena in volcanic areas and consequently provide important constraints to the hazard and risk management.

Bibliography

Alidibirov, M., and D. B. Dingwell (1996a), An experimental facility for the investigation of magma fragmentation by rapid decompression, *Bulletin of Volcanology*, *58*(5), 411–416.

Alidibirov, M., and D. B. Dingwell (1996b), Magma fragmentation by rapid decompression, *Nature*, *380*(6570), 146–148.

Alidibirov, M., and D. B. Dingwell (2000), Three fragmentation mechanisms for highly viscous magma under rapid decompression, *Journal of Volcanology and Geothermal Research*, *100*, 413–421.

Alidibirov, M. A. (1994), A model for viscous magma fragmentation during volcanic blasts, *Bulletin of Volcanology*, *56*(6-7), 459–465.

Anderson, S. W., J. H. Fink, and W. I. Rose (1995), Mount st helens and santiaguito lava domes: The effect of short-term eruption rate on surface texture and degassing processes, *Journal of Volcanology and Geothermal Research*, *69*(1-2), 105–116.

Balme, M. R., V. Rocchi, C. Jones, P. R. Sammonds, P. G. Meredith, and S. Boon (2004), Fracture toughness measurements on igneous rocks using a high-pressure, high-temperature rock fracture mechanics cell, *Journal of Volcanology and Geothermal Research*, *132*(2-3), 159–172.

Barclay, J., M. J. Rutherford, M. R. Carroll, M. D. Murphy, J. D. Devine, J. Gardner, and R. S. J. Sparks (1998), Experimental phase equilibria constraints on pre-eruptive storage conditions of the soufriere hills magma, *Geophysical Research Letters*, *25*(18), 3437–3440.

Belikov, B. P., B. V. Zalesskii, Y. A. Rozanov, E. A. Sanina, I. P. o. s. t. p. p. o. r. I. Z. B. e. P. Timchenko, and .-. mechanical properties of rocks. Izdatel'stvo Nauka, Moskau (1964), Methods of studying the physicomechanical properties of rocks., in *Physical and mechanical properties of rocks.*, edited by B. V. Zalesskii, pp. 1–58, Izdatel'stvo Nauka, Moskau.

Ben-Zion, Y. (1998), Properties of seismic fault zone waves and their utility for imaging low-velocity structures, *Journal of Geophysical Research-Solid Earth*, *103*(B6), 12,567–12,585.

Birch, F. (1960), The velocity of compressional waves in rocks to 10 kilobars, part 1, *Journal of Geophysical Research*, *65*(1083).

Birch, F. (1961), The velocity of compressional waves in rocks to 10 kilobars, part 2, *Journal of Geophysical Research*, *66*(2199).

Botcharnikov, R., F. Holtz, H. Behrens, and H. Sato (2003), Phase equilibrium study and constraints on pre-eruptive conditions of unzen magmas., *Abstract volume of Schwerpunktkolloquium IODP-ICDP*, p. 3pp.

Brace, W. (1965), Relation of elastic properties of rocks to fabric, *Journal of Geophysical Research*, *70*(22).

Brook, N. (1993), The measurement and estimation of basic rock strength., in *Comprehensive rock engineeringprinciples, practice and projects.*, vol. vol. 3 (Rock testing and site characterization), edited by J. A. Hudson, E. T. Brown, C. Fairhurst, and E. Hoek, p. 4166, Pergamon Press, Oxford.

Brunauer, S., P. H. Emmett, and E. Teller (1938), Adsorption of gases in multimolecular layer., *Journal of American Chemical Society*, *60*, 309–319.

Cagnoli, B., A. Barmin, O. Melnik, and R. S. J. Sparks (2002), Depressurization of fine powders in a shock tube and dynamics of fragmented magma in volcanic conduits, *Earth and Planetary Science Letters*, *204*(1-2), 101–113.

Carn, S. A., R. B. Watts, G. Thompson, and G. E. Norton (2004), Anatomy of a lava dome collapse: the 20 march 2000 event at soufriere hills volcano, montserrat, *Journal of Volcanology and Geothermal Research*, *131*(3-4), 241–264.

Cas, R. A. F., and J. V. Wright (1987), *Volcanic successions: modern and ancient.*, Chapman and Hall, London.

Cashman, K. (1992), Groundmass crystallization of mount st. helens dacite, 1980 1986: a tool for interpreting shallow magmatic processes., *Contributions to Mineralogy and Petrology*, *109*, 431–449.

Cashman, K. V., B. Sturtevant, P. Papale, and O. Navon (2000), Magmatic fragmentation, in *Encyclopedia of Volcanoes*, edited by H. Sigurdsson, Academic Press.

Cayol, V., and F. H. Cornet (1997), 3d mixed boundary elements for elastostatic deformation field analysis, *International Journal of Rock Mechanics and Mining Sciences*, *34*(2), 275–287.

Cayol, V., and F. H. Cornet (1998), Three-dimensional modeling of the 1983-1984 eruption at piton de la fournaise volcano, reunion island, *Journal of Geophysical Research-Solid Earth*, *103*(B8), 18,025–18,037.

Cayol, V., D. Green, and J. Neuberg (2004), Location of the source of deformations and hybrid earthquakes cycles at montserrat, *Geophysical Research Abstracts*, *6*(06471).

Chouet, B., G. Saccorotti, M. Martini, P. Dawson, G. DeLuca, G. Milana, and R. Scarpa (1997), Source and path effects in the wave fields of tremor and explosions at stromboli volcano, italy, *Journal of Geophysical Research-Solid Earth*, *102*(B7), 15,129–15,150.

Chouet, B. A. (1996), *New Methods and future trends in seismological volcano monitoring*, Monitoring and mitigation of volcano hazards, Springer-Verlag, Berlin.

Christensen, N. (1982), Seismic velocities, in *CRC Handbook of Physical Properties of Rocks*, vol. Vol. II,, edited by R. S. Carmichael, CRC Press.

Clarke, A. B., A. Neri, B. Voight, G. Macedonio, and T. H. Druitt (2002), Computational modelling of the transient dynamics of the august 1997 vulcanian explosions at soufrire hills volcano, montserrat: influence of initial conduit conditions on near-vent pyroclasic dispersal, in *The Eruption of Soufrire Hills Volcano, Montserrat, from 1995 to 1999.*, vol. Memoirs, edited by T. H. Druitt and B. P. Kokelaar, pp. 319–348, Geological Society, London.

Devine, J. D., M. J. Rutherford, and J. E. Gardner (1998), Petrologic determination of ascent rates for the 1995-1997 soufriere hills volcano andesitic magma, *Geophysical Research Letters*, *25*(19), 3673–3676.

Devine, J. D., M. J. Rutherford, G. E. Norton, and S. R. Young (2003), Magma storage region processes inferred from geochemistry of fe-ti oxides in andesitic magma, soufriere hills volcano, montserrat, wi, *Journal of Petrology*, *44*(8), 1375–1400.

Dingwell, D. (1998), Recent experimental progress in the physical description of silicic magma relevant to explosive volcanism., in *The physics of explosive volcanic eruptions.*, vol. 145, edited by J. S. Gilbert and R. S. J. Sparks, pp. 9–26, Geological society of London.

Dingwell, D. B. (1996), Volcanic dilemma: Flow or blow?, *Science*, *273*, 1054–1055.

Dingwell, D. B., and S. L. Webb (1989), Structural relaxations in silicate melts and non-newtonian melt rheology in geologic processes, *Physics and Chemistry of Minerals*, *16*, 508–516.

Dobran, F. (1992), Nonequilibrium-flow in volcanic conduits and application to the eruptions of mt st-helens on may 18, 1980, and vesuvius in ad 79, *Journal of Volcanology and Geothermal Research*, *49*(3-4), 285–311.

Druitt, T. H., et al. (2002), Episodes of cyclic vulcanian explosive activity with fountain collapse at soufrire hills volcano, montserrat., in *The Eruption of Soufrire Hills Volcano, Montserrat, from 1995 to 1999.*, vol. Memoirs, edited by T. H. Druitt and B. P. Kokelaar, pp. 281–306, Geological Society, London.

Eichelberger, J. C., and D. Hayes (1982), Magmatic model for the mount st. helens blast of may 18, 1980., *Journal of Geophysical Research*, *87*, 7727–7738.

Eichelberger, J. C., H. R. Carrigan, H. R. Westrich, and R. H. Price (1986), Non-explosive silicic volcanism., *Nature*, *323*, 595–602.

Elsworth, D., B. Voight, G. Thompson, and S. R. Young (2004), Thermal-hydrologic mechanism for rainfall-triggered collapse of lava domes, *Geology*, *32*(11), 969–972.

Fink, J., and R. W. Griffiths (1990), Radial spreading of viscous gravity currents with solidifying crust., *Journal of Fluid Mechanics*, *221*, 485–509.

Fink, J. H., and S. W. Kieffer (1993), Estimate of pyroclastic flow velocities resulting from explosive decompression of lava domes, *Nature*, *363*(6430), 612–615.

Finlayson, D. M., O. Gudmundsson, I. Itikarai, Y. Nishimura, and H. Shimamura (2003), Rabaul volcano, papua new guinea: seismic tomographic imaging of an active caldera, *Journal of Volcanology and Geothermal Research*, *124*(3-4), 153–171.

Formenti, Y., T. H. Druitt, and K. Kelfoun (2003), Characterisation of the 1997 vulcanian explosions of soufriere hills volcano, montserrat, by video analysis, *Bulletin of Volcanology*, *65*(8), 587–605.

Fujii, T., and S. Nakada (1999), The 15 september 1991 pyroclastic flows at unzen volcano (japan), a flow model for associated ash-cloud surges, *Journal of Volcanology and Geothermal Research*, *89*(1-4), 159–172.

Gardner, J. E., R. M. E. Thomas, C. Jaupart, and S. Tait (1996), Fragmentation of magma during plinian volcanic eruptions, *Bulletin of Volcanology*, *58*(2-3), 144–162.

Gardner, J. E., M. Hilton, and M. R. Carroll (1999), Experimental constraints on degassing of magma: Isothermal bubble growth during continuous decompression from high pressure., *Earth Planetary Science Letters*, *168*, 201–218.

Gebrande, H. (1982), Elastic wave velocities and constants of elasticity of rocks at room temperature and pressures up to 1 gpa, in *in Landolt-Boernstein, New Series*, *Physical Properties of Rocks*, vol. V/1b, edited by K.-H. Hellwege, Springer Verlag, Berlin.

Gilbert, J., and R. Sparks (1998), The physics of explosive volcanic eruptions., *Special Publication of the Geological Society of London*, *145*.

Glenn, E. (2005), The physics hypertextbook.

Gonnermann, H. M., and M. Manga (2003), Explosive volcanism may not be an inevitable consequence of magma fragmentation, *Nature*, *426*(6965), 432–435.

Gregg, S. J., and K. S. W. Sing (1982), *Adsoption, Surface Area and Porosity*, 2nd edition ed., Academic Press.

Harford, C. L., R. S. J. Sparks, and A. E. Fallick (2003), Degassing at the soufriere hills volcano, montserrat, recorded in matrix glass compositions, *Journal of Petrology*, *44*(8), 1503–1523.

Hidayat, D., B. Voight, C. Langston, A. Ratdomopurbo, and C. Ebeling (2000), Broadband seismic experiment at merapi volcano, java, indonesia: very-long-period pulses embedded in multiphase earthquakes, *Journal of Volcanology and Geothermal Research*, *100*(1-4), 215–231.

Horwell, C. J., L. P. Brana, R. S. J. Sparks, M. D. Murphy, and V. L. Hards (2001), A geochemical investigation of fragmentation and physical fractionation in pyroclastic flows from the soufriere hills volcano, montserrat, *Journal of Volcanology and Geothermal Research*, *109*(4), 247–262.

Hoshizumi, H., K. Uto, and K. Watanabe (1999), Geology and eruptive history of unzen volcano, shimabara peninsula, kyushu, sw japan, *Journal of Volcanology and Geothermal Research*, *89*(1-4), 81–94.

Hughes, D. S., and H. J. Jones (1950), Variation of elastic moduli of igneous rocks with pressure and temperature, *Geological Society of America Bulletin*, *61*(8), 843–856.

Hurwitz, S., and O. Navon (1994), Bubble nucleation in rhyolitic melts: Experiments at high pressure, temperature, and water content., *Earth Planetary Science Letters*, *122*, 267–280.

Ichihara, M., D. Rittel, and B. Sturtevant (2002), Fragmentation of a porous viscoelastic materials: implication to magma fragmentation., *Journal of Geophysical Research*, *106*, 2226–2239.

ISRM, ., Commission on testing methods (1988), Suggested methods for determining the fracture toughness of rock., *International Journal of Rock Mechanics and Mining Sciences & Geomechanics Abstracts*, *25*, 71–97.

Jaeger, J. C., and N. G. W. Cook (1979), *Fundamentals of rock mechanics.*, 3rd edition ed., Chapman & Hall, London.

Jahnke, G., H. Igel, and Y. Ben-Zion (2002), Three-dimensional calculations of fault-zone-guided waves in various irregular structures, *Geophysical Journal International*, *151*(2), 416–426.

Jaupart, C., and C. J. Allègre (1991), Gas content, eruption rate and instabilities of eruption regime in silicic volcanoes, *Earth and Planetary Science Letters*, *102*, 413–429.

Jousset, P., J. Neuberg, and S. Sturton (2003), Modelling the time-dependent frequency content of low-frequency volcanic earthquakes, *Journal of Volcanology and Geothermal Research*, *128*(1-3), 201–223.

Kennedy, B., O. Spieler, B. Scheu, U. Kueppers, J. Taddeucci, and D. D.B. (2005), Conduit implosion during vulcanian eruptions., *Geology*, p. Accepted for publication.

Kern, H. (1982a), Elastic wave velocities and constants of elasticity of rocks at elevated pressures and temperatures, in *Landolt-Boernstein, New Series*, *Physical Properties of Rock*, vol. V/1b, edited by K.-H. Hellwege, Springer Verlag, Berlin.

Kern, H. (1982b), P- and s-wave velocities in crustal and mantle rocks under the simultaneous action of high confining pressure and high temperature and the effect of the rock microstructure, in *High-pressure researches in geoscience; behaviour and properties of earth materials at high pressures and temperatures; results of a priority program and proceedings of its final colloquium*, edited by W. Schreyer, E. Schweizerbart'sche Verlagsbuchhandlung, Stuttgart.

Kern, H. (1993), P-wave and s-wave anisotropy and shear-wave splitting at pressure and temperature in possible mantle rocks and their relation to the rock fabric, *Physics of the Earth and Planetary Interiors*, *78*(3-4), 245–256.

Kern, H., and M. Fakhimi (1975), Effect of fabric anisotropy on compressional-wave propagation in various metamorphic rocks for the range 20-700 degrees c at 2 kbars, *Tectonophysics*, *28*(4).

Kern, H., and J. M. Tubia (1993), Pressure and temperature-dependence of p-wave and s-wave velocities, seismic anisotropy and density of sheared rocks from the sierra alpujata massif (ronda peridotites, southern spain), *Earth and Planetary Science Letters*, *119*(1-2), 191–205.

Kern, H., B. Liu, and T. Popp (1997), Relationship between anisotropy of p and s wave velocities and anisotropy of attenuation in serpentinite and amphibolite, *Journal of Geophysical Research-Solid Earth*, *102*(B2), 3051–3065.

Kilburn, C. R. J. (2003), Multiscale fracturing as a key to forecasting volcanic eruptions, *Journal of Volcanology and Geothermal Research*, *125*(3-4), 271–289.

Klug, C., and K. V. Cashman (1996), Permeability development in vesiculating magmas: Implications for fragmentation, *Bulletin of Volcanology*, *58*(2-3), 87–100.

Kovalenko, Y. F. (1980), Effective characteristics of bodies with isolated cracks filled by gas: fracturing wave., *Mechan. AS USSR, Moscow*, *155*, 52pp (in russian).

Kueppers, U., B. Scheu, O. Spieler, and D. Dingwell (2005a), Field-based density measurements as tool to identify pre-eruption dome structure: set-up and first results from unzen volcano, japan., *Journal of Volcanology and Geothermal Research*, *141*(1-2), 65–75.

Kueppers, U., B. Scheu, O. Spieler, and D. Dingwell (2005b), Fragmentation efficiency of explosive volcanic eruptions: a study of experimentally generated pyroclasts, *Journal of Volcanology and Geothermal Research*, p. accepted for publication.

Kusakabe, M., H. Sato, S. Nakada, and T. Kitamura (1999), Water contents and hydrogen isotopic ratios of rocks and minerals from the 1991 eruption of unzen volcano, japan, *Journal of Volcanology and Geothermal Research*, *89*(1-4), 231–242.

Lane, S. J., B. A. Chouet, J. C. Phillips, P. Dawson, G. A. Ryan, and E. Hurst (2001), Experimental observations of pressure oscillations and flow regimes in an analogue volcanic system, *Journal of Geophysical Research-Solid Earth*, *106*(B4), 6461–6476.

Lebedev, E. B., and A. V. Zharikov (2000), Study of intergranular films and interstitial phases in geomaterials using high temperature centrifuge and ultrasonic method at high pressure, *Physics and Chemistry of the Earth Part a-Solid Earth and Geodesy*, *25*(2), 209–214.

Lensky, N. G., O. Navon, and V. Lyakhovsky (2004), Bubble growth during decompression of magma: Experimental and theoretical investigation., *Journal of Volcanology and Geothermal Research*, *129*, 7–22.

Li, Y. G., and P. C. Leary (1990), Fault zone trapped seismic-waves, *Bulletin of the Seismological Society of America*, *80*(5), 1245–1271.

Li, Y. G., and F. L. Vernon (2001), Characterization of the san jacinto fault zone near anza, california, by fault zone trapped waves, *Journal of Geophysical Research-Solid Earth*, *106*(B12), 30,671–30,688.

Londono, J. M., and Y. Sudo (2003), Velocity structure and a seismic model for nevado del ruiz volcano (colombia), *Journal of Volcanology and Geothermal Research*, *119*(1-4), 61–87.

Lyman, A. W., E. Koenig, and J. H. Fink (2004), Predicting yield strengths and effusion rates of lava domes from morphology and underlying topography, *Journal of Volcanology and Geothermal Research*, *129*(1-3), 125–138.

Mader, H. M., Y. Zhang, J. C. Phillips, R. S. J. Sparks, B. Sturtevant, and E. Stolper (1994), Experimental simulations of explosive degassing of magma, *Nature*, *372*(6501), 85–88.

Mader, H. M., M. Manga, and T. Koyaguchi (2004), The role of laboratory experiments in volcanology, *Journal of Volcanology and Geothermal Research*, *129*, 1–5.

Mangan, M., and T. Sisson (2000), Delayed, disequilibrium degassing in rhyolite magma: decompression experiments and implications for explosive volcanism, *Earth and Planetary Science Letters*, *183*(3-4), 441–455.

Martel, C., D. B. Dingwell, O. Spieler, M. Pichavant, and M. Wilke (2000), Fragmentation of foamed silicic melts: an experimental study, *Earth and Planetary Science Letters*, *178*(1-2), 47–58.

Matthews, A. J., J. Barclay, S. Carn, G. Thompson, J. Alexander, R. Herd, and C. Williams (2002), Rainfall-induced volcanic activity on montserrat, *Geophysical Research Letters*, *29*(13), 16–44.

Mayfield, J., and P. Schiffman (1998), Measuring the density of porous volcanic rocks in the field using a saran coating., *Journal of geoscience education*, *46*, 460–464.

McBirney, A. R., and T. Murase (1970), Factors governing the formation of pyroclastic rocks., *Bulletin of Volcanology*, *34*, 372–384.

Melnik, O. (2000), Dynamics of two-phase conduit flow of high-viscosity gas-saturated magma: large variations of sustained explosive eruption intensity, *Bulletin of Volcanology*, *62*(3), 153–170.

Melnik, O., and R. S. J. Sparks (1999), Nonlinear dynamics of lava dome extrusion, *Nature*, *402*(6757), 37–41.

Melnik, O., and R. S. J. Sparks (2002), Modelling of conduit flow dynamics during explosive activity at soufriere hills volcano, montserrat., in *The Eruption of Soufrière Hills Volcano, Montserrat, from 1995 to 1999.*, vol. Memoirs, edited by T. H. Druitt and B. P. Kokelaar, pp. 307–317, Geological Society, London.

Meredith, P. G., and B. K. Atkinson (1985), Fracture-toughness and subcritical crack-growth during high-temperature tensile deformation of westerly granite and black gabbro, *Physics of the Earth and Planetary Interiors*, *39*(1), 33–51.

Mourtada-Bonnefoi, C. C., and D. Laporte (2000), Homogeneous bubble nucleation in rhyolitic magmas: An experimental study of the effect of h2o and co2, *Journal of Geophysical Research-Solid Earth*, *107*(B4), 1–21.

Mourtada-Bonnefoi, C. C., and H. M. Mader (2004), Experimental observations of the effect of crystals and pre-existing bubbles on the dynamics and fragmentation of vesiculating flows, *Journal of Volcanology and Geothermal Research*, *129*(1-3), 83–97.

Moynihan, C. T. (1995), Structural relaxation and the glass transition, in *Structure, Dynamics and Properties of Silicate Melts*, *Reviews in Mineralogy*, vol. 32, pp. 1–19.

Mueller, H., and S. Raab (1997), Elastic wave velocities of granite at experimental simulated partial melting conditions, *Physics and Chemistry of the Earth*, *22*(1-2).

Mueller, S., O. Melnik, O. Spieler, B. Scheu, and D. B. Dingwell (2004), Permeability and degassing of porous volcanic rocks undergoing rapid decompression: an experimental determination., *Eos Trans. AGU*, *85*(Fall Meet. Suppl.), V43D–1444.

Mueller, S., O. Spieler, B. Scheu, and D. B. Dingwell (2005), Permeability and degassing of dome lavas undergoing rapid decompression: an experimental determination,, *Bulletin of Volcanology*, pp. DOI: 10.1007/s00,445–004–0392–4.

Murase, A. R., T.and McBirney, and W. G. Melson (1985), Viscosity of the dome of mount st. helens, *Journal of Volcanology and Geothermal Research*, *24*, 193–204.

Murphy, M. D., R. S. J. Sparks, J. Barclay, M. R. Carroll, and T. S. Brewer (2000), Remobilization of andesite magma by intrusion of mafic magma at the soufriere hills volcano, montserrat, west indies, *Journal of Petrology*, *41*(1), 21–42.

Nakada, S. (1992), Lava domes and pyroclastic flows of the 1991-1992 eruption at unzen volcano., in *Unzen Volcano, the 1990-1992 eruption*, edited by T. Yanagi, H. Okada, and K. Ohta, pp. 56–66, The Nishinippon and Kyushu University Press, Fukuoka.

Nakada, S., and Y. Motomura (1992), Mineralogy of lavas of 1991-1992 eruption at unzen volcano, *The Fall Meeting of the Volcanological Society of Japan*, p. 148.

Nakada, S., and Y. Motomura (1999), Petrology of the 1991-1995 eruption at unzen: effusion pulsation and groundmass crystallization, *Journal of Volcanology and Geothermal Research*, *89*(1-4), 173–196.

Nakada, S., H. Shimizu, and K. Ohta (1999), Overview of the 1990-1995 eruption at unzen volcano, *Journal of Volcanology and Geothermal Research*, *89*(1-4), 1–22.

Neuberg, J. (2000), Characteristics and causes of shallow seismicity in andesite volcanoes, *Philosophical Transactions of the Royal Society of London Series a-Mathematical Physical and Engineering Sciences*, *358*(1770), 1533–1546.

Neuberg, J., R. Luckett, B. Baptie, and K. Olsen (2000), Models of tremor and low-frequency earthquake swarms on montserrat, *Journal of Volcanology and Geothermal Research*, *101*(1-2), 83–104.

Neuberg, J., H. Tuffen, L. Collier, D. Green, T. Powell, and D. Dingwell (2005), The trigger mechanism of low-frequency earthquakes on montserrat, *Journal of Volcanology and Geothermal Research*, *in press*.

Norton, G. E., et al. (2002), Pyroclastic flow and explosive activity of the lava dome of soufrire hills volcano, montserrat, during a period of no magma extrusion (march 1998 - november 1999), in *The Eruption of Soufrire Hills Volcano, Montserrat, from 1995 to 1999.*, vol. Memoirs, edited by T. H. Druitt and B. P. Kokelaar, pp. 467–482, Geological Society, London.

Ohmi, S., and J. M. Lees (1995), 3-dimensional p-wave and s-wave velocity structure below unzen volcano, *Journal of Volcanology and Geothermal Research*, *65*(1-2), 1–26.

Ouchterlony, F. (1989), On the background to the formulas and accuracy of rock fracture-toughness measurements using isrm standard core specimens, *International Journal of Rock Mechanics and Mining Sciences & Geomechanics Abstracts*, *26*(1), 13–23.

Pallister, J. S., R. P. Hoblitt, and A. G. Reyes (1992), A basalt trigger for the 1991 eruptions of pinatubo volcano?, *Nature*, *356*, 426–428.

Papale, P. (1999), Strain-induced magma fragmentation in explosive eruptions, *Nature*, *397*(6718), 425–428.

Papale, P., A. Neri, and G. Macedonio (1998), The role of magma composition and water content in explosive eruptions i. conduit ascent dynamics., *Journal of Volcanology and Geothermal Research*, *87*, 75–93.

Phillips, J. C., S. J. Lane, A.-M. Lejeune, and M. Hilton (1995), Gum-rosin-acetone system as an analogue to the degassing behaviour of hydrated magmas., *Bulletin of Volcanology*, *57*, 263–268.

Polacci, M., P. Papale, and M. Rosi (2001), Textural heterogeneities in pumices from the climactic eruption of mount pinatubo, 15 june 1991, and implications for magma ascent dynamics, *Bulletin of Volcanology*, *63*(2-3).

Polacci, M., L. Pioli, and M. Rosi (2003), The plinian phase of the campanian ignimbrite eruption (phlegrean fields, italy): evidence from density measurements and textural characterization of pumice, *Bulletin of Volcanology*, *65*(6), 418–432.

Poplawski, R. F. (1997), Seismic parameters and rockburst hazard at mt charlotte mine, *International Journal of Rock Mechanics and Mining Science*, *34*(8), 1213–1228.

Robertson, R., et al. (1998), The explosive eruption of soufriere hills volcano, montserrat, west indies, 17 september, 1996, *Geophysical Research Letters*, *25*(18), 3429–3432.

Robertson, R. E. A., W. P. Aspinall, R. A. Herd, G. E. Norton, R. S. J. Sparks, and S. R. Young (2000), The 1995-1998 eruption of the soufrière hills volcano, montserrat, wi, *Philosophical Transactions of the Royal Society of London Series a-Mathematical Physical and Engineering Sciences*, *358*(1770), 1619–1637.

Roobol, M. J., and A. L. Smith (1998), Pyroclastic stratigraphy of the soufrière hills volcano, montserrat - implications for the present eruption, *Geophysical Research Letters*, *25*(18), 3393–3396.

Saar, M. O., and M. Manga (1999), Permeability-porosity relationship in vesicular basalts., *Geophysical Research Letters*, *26*(1), 111–114.

Sahimi, M. (1994), *Applications of Percolation Theory.*, 300pp pp., Taylor and Francis, London.

Sato, H., T. Fujii, and S. Nakada (1992), Crumbling of dacite dome lava and generation of pyroclastic flows at unzen volcano, *Nature*, *360*(6405), 664–666.

Sato, H., T. Kitamura, M. Kusakabe, and S. Nakada (1995), Critical pore gas pressure of dacite lavas in transition from dome extrusion to vulcanian explosion at unzen volcano, japan., *IUGG XXI General Assembly, Boulder, CO, Abstracts*, B414.

Schopper, J. R. (1982), Porosity and permeability., in *Numerical Data and Functional Relationships in Science and Technology.*, edited by G. Angenheister, pp. 184–193, Springer, Berlin.

Self, S., L. Wilson, and I. Nairn (1979), Vulcanian eruption mechanisms., *nature*, *277*, 440443.

Smith, J. V., Y. Miyake, and T. Oikawa (2001), Interpretation of porosity in dacite lava domes as ductile-brittle failure textures, *Journal of Volcanology and Geothermal Research*, *112*(1-4), 25–35.

Sparks, R. (1978), The dynamics of bubble formation and growth in magmas: a review and analysis, *Journal of Volcanology and Geothermal Research*, *3*, 1–37.

Sparks, R. (1994), Comment on "dynamics of diffusive bubble growth in magmas: Isothermal case"by a. a. proussevitch, d.l sahagian, and a. t. anderson, *Journal of Geophysical Research*, *99*(B9), 17,827–17,828.

Sparks, R. S. J., and S. R. Young (2002), The eruption of soufrire hills volcano, montserrat (1995-1998): overview of scientific results:, in *The Eruption of Soufrire Hills Volcano, Montserrat, from 1995 to 1999.*, vol. Memoirs, edited by T. H. Druitt and B. P. Kokelaar, pp. 45–71, Geological Society, London.

Sparks, R. S. J., et al. (1998), Magma production and growth of the lava dome of the soufriere hills volcano, montserrat, west indies: November 1995 to december 1997, *Geophysical Research Letters*, *25*(18), 3421–3424.

Sparks, R. S. J., et al. (2002), Generation of a debris avalanche and violent pyroclastic density current on 26 december (boxing day) at soufrire hills volcano. montserrat., in *The Eruption of Soufrire Hills Volcano, Montserrat, from 1995 to 1999.*, vol. Memoirs, edited by T. H. Druitt and B. P. Kokelaar, pp. 409–434, Geological Society, London.

Spieler, O., M. Alidibirov, and D. B. Dingwell (2003), Grain-size characteristics of experimental pyroclasts of 1980 mount st. helens cryptodome dacite: effects of pressure drop and temperature, *Bulletin of Volcanology*, *65*(2-3), 90–104.

Spieler, O., D. B. Dingwell, and M. Alidibirov (2004a), Magma fragmentation speed: an experimental determination, *Journal of Volcanology and Geothermal Research*, *129*(1-3), 109–123.

Spieler, O., B. Kennedy, U. Kueppers, D. B. Dingwell, B. Scheu, and J. Taddeucci (2004b), The fragmentation threshold of pyroclastic rocks, *Earth and Planetary Science Letters*, *226*(1-2), 139–148.

Sturton, S., and H. Neuberg (2003), The effects of a decompression on seismic parameter profiles in a gas-charged magma, *Journal of Volcanology and Geothermal Research*, *128*(1-3), 187–199.

Sugioka, I., and M. Bursik (1995), Explosive fragmentation of erupting magma, *Nature*, *373*(6516), 689–692.

Tada, T. (1985), Spreading of the okinawa trough and its relation to the crustal deformation in the kyushu (2)., *Journal of the Seismological Society of Japan (Zisin)*, *38*, 1–12.

Tuffen, H., D. B. Dingwell, and H. Pinkerton (2003), Repeated fracture and healing of silicic magma generate flow banding and earthquakes?, *Geology*, *31*(12), 1089–1092.

Ui, T., N. Matsuwo, M. Sumita, and A. Fujinawa (1999), Generation of block and ash flows during the 1990-1995 eruption of unzen volcano, japan, *Journal of Volcanology and Geothermal Research*, *89*(1-4), 123–137.

Umakoshi, K., H. Shimizu, N. Matsuwo, and K. Otha (1992), Surface temperature measurements of lava domes and pyroclastic flows by infrared thermal video system., in *Unzen Volcano, the 1990-1992 eruption*, edited by T. Yanagi, H. Okada, and K. Ohta, pp. 44–48, The Nishinippon and Kyushu University Press, Fukuoka.

Umakoshi, K., H. Shimizu, and N. Matsuwo (2001), Volcano-tectonic seismicity at unzen volcano, japan 1985-1999, *Journal of Volcanology and Geothermal Research*, *112*(1-4), 117–131.

Verhoogen, J. (1951), Mechanics of ash formation., *American Journal of Science*, *249*, 729–739.

Watanabe, K., and H. Hoshizumi (1995), Geological map of unzen volcano.

Woods, A. W., R. S. J. Sparks, L. J. Ritchie, J. Batey, C. Gladstone, and M. I. Bursik (2002), The explosive decompression of a pressurized volcanic dome: the 26 december 1997 collapse and explosion of soufrire hills volcano, montserrat., in *The Eruption of Soufrire Hills Volcano, Montserrat, from 1995 to 1999.*, vol. Memoirs, edited by T. H. Druitt and B. P. Kokelaar, pp. 595–602, Geological Society, London.

Yanagi, T., H. Okada, and K. Ohta (1992), *Unzen Volcano, the 1990-1992 eruption*, 137pp pp., The Nishinippon and Kyushu University Press, Fukuoka.

Young, S. R., et al. (1997), The ongoing eruption in montserrat, *Science*, *276*(5311), 371–372.

Zhang, Y. X. (1999), A criterion for the fragmentation of bubbly magma based on brittle failure theory, *Nature*, *402*(6762), 648–650.

Zhang, Y. X., B. Sturtevant, and E. M. Stolper (1997), Dynamics of gas-driven eruptions: Experimental simulations using co2-h2o-polymer system, *Journal of Geophysical Research-Solid Earth*, *102*(B2), 3077–3096.

Zhang, Z. X. (2002), An empirical relation between mode i fracture toughness and the tensile strength of rock, *International Journal of Rock Mechanics & Mining Sciences*, *39*, 401406.

Acknowledgements

Initially, I would like to thank my supervisors Donald B. Dingwell and Oliver Spieler for their advice and guidance through the thesis and their encouragement to present and publish my results. Oli, thanks for inaugurating me into the mystery of destroying rocks and other wicked stuff.

Thanks to Hartmut Kern for his interest at my very porous Unzen dacites and helpful discussions as well as his willingness to share his broad knowledge of the behavior of elastic wave velocities at HT-HP conditions.

I am indebted to Pete Sammonds and Valentina Rocchi for their warm welcome and the opportunity to perform high-temperature fracture toughness tests at the Mineral Rock & Ice Physics Laboratory at the University College London.

Special thanks to Setsuya Nakada and Hiroshi Shimizu who provided qualitative information, SEVO (Shimabara Earthquake and Volcano Observatory) infrastructure and enabled the access to the Unzen National Park.

Thanks to Joachim Gottsmann for his guidance in Japan during the 2000 field campaign and drilling the layered block.

I am grateful to Oleg Melnik for the modelling of the pressure profiles and the pressure drop curves during decompression.

Special thanks are given to Ulli Küppers, Bastl Müller, Ben Kennedy, Jacopo Taddeucci, Yan Lavallee, Hugh Tuffen, and all other members of the volcanology group for many fruitful discussions during and after work hours. I appreciate, that all of you are not just stimulating colleagues but also great friends. I am deeply grateful to Ulli for carrying my tiny little (but apparently extremely massive) blue rock down the Unzen dome and two great field campaigns in Japan, including two unforgettable evenings at the Yakitori-bar. Thanks also for providing always good mood and "coffee at the balcony" with all kinds of discussions. Thanks, Bastl, for believing in my math

and physics skills even at the time I doubted that, your helpfulness and sense of humor, that saved more than once my day as well as the thorough reading of the manuscript.

I would like to thank all employees from the workshop and the secretary for their help with the laboratory equipment and administrative problems.

Thanks to Yvonne and Greta for showing me that some things are even worse than university bureaucracy and for her friendship, trust and motivation especially in the final stage of this work.

Thanks Babe, for the emotional support during all stages of this PhD and the smaller and bigger catastrophes of the daily life.

Many thanks to my parents and my relatives for their constant support and interest in my work.
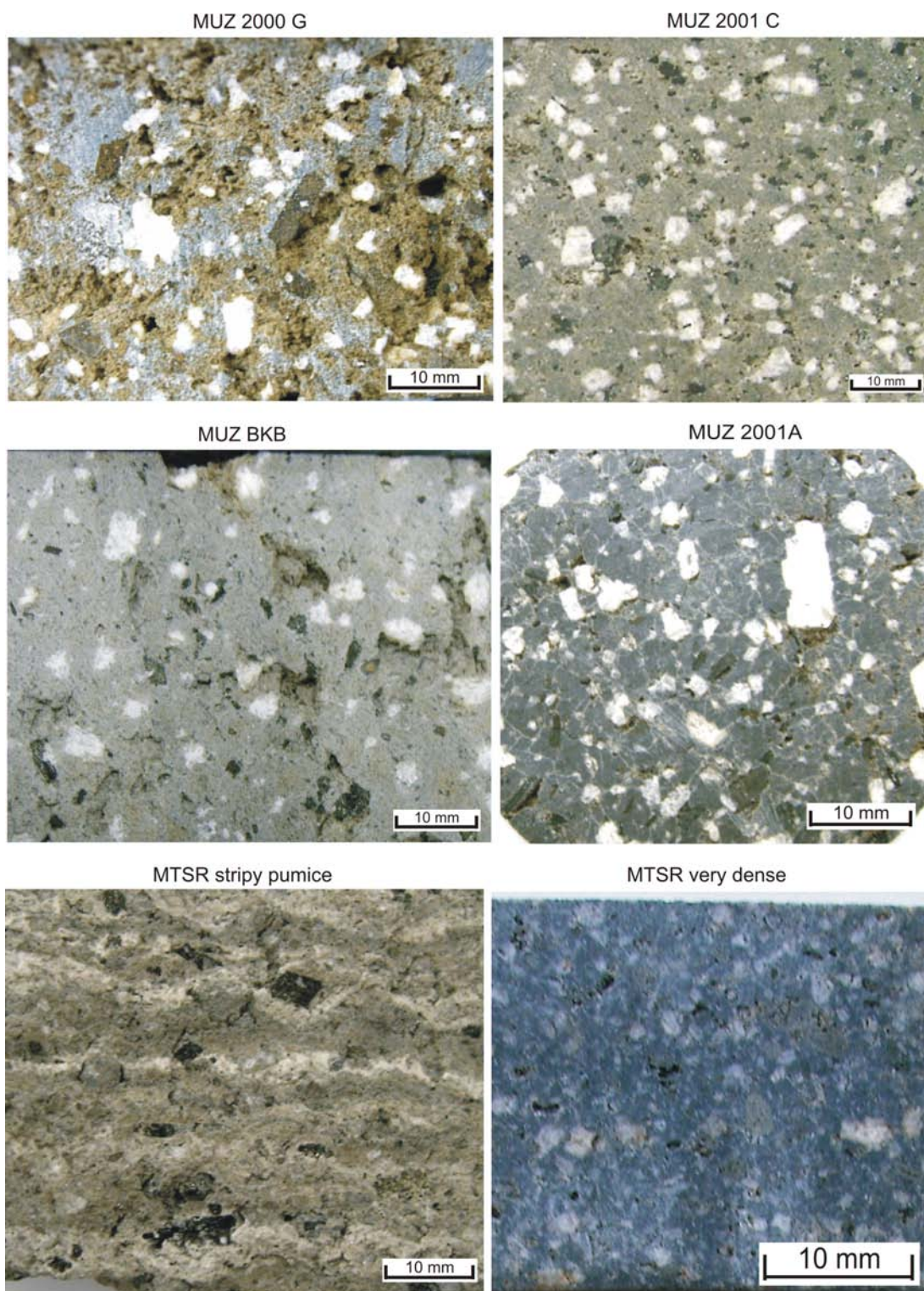
Appendix A

Photographs of samples

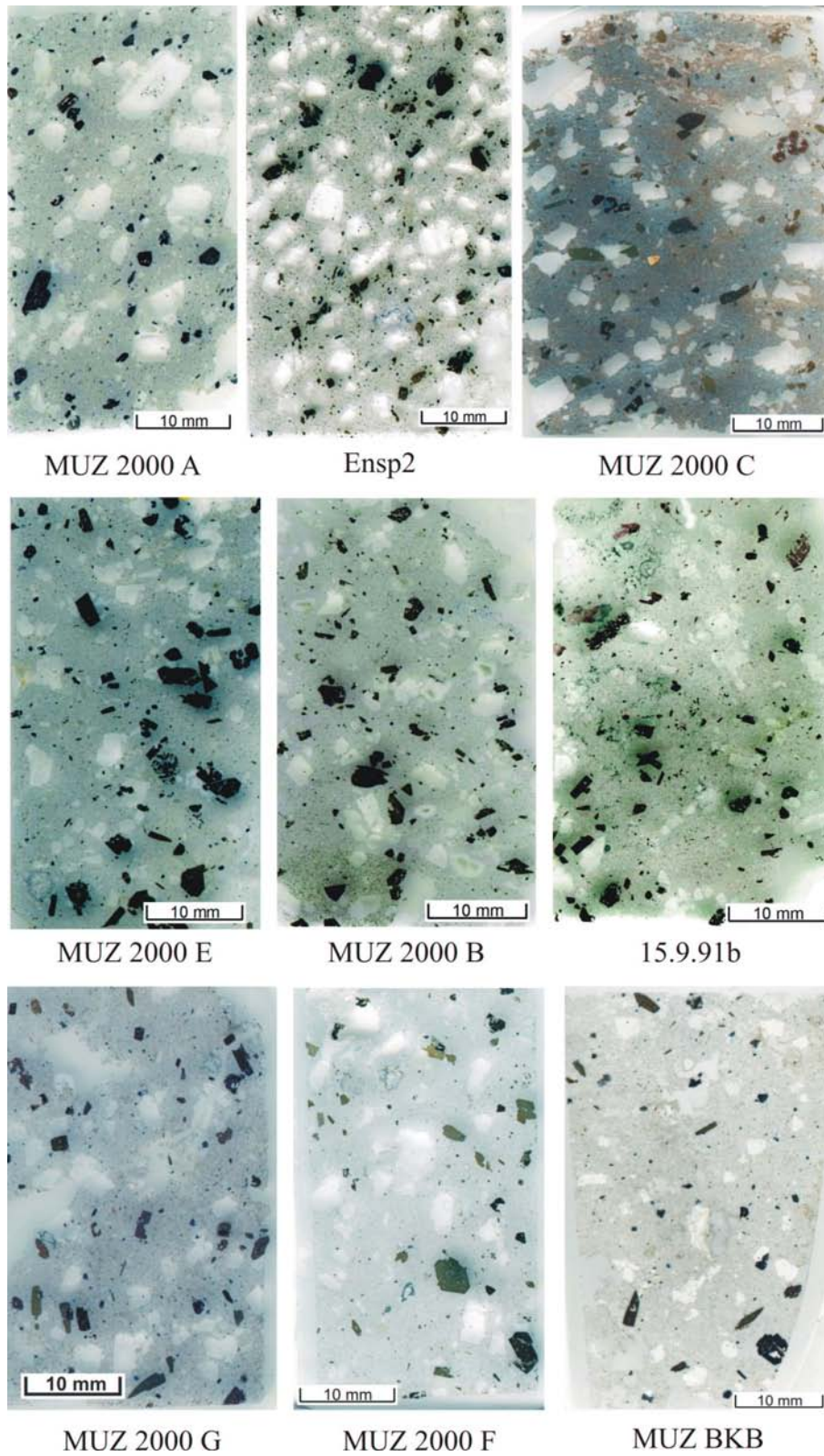**Figure A.1:** Photographs of analyzed samples from Unzen Volcano and Montserrat.

Figure A.2: Scanned thinsections of Unzen dacite samples.

Appendix B

Tables of experimental results

Sample	Pressure (MPa)	Temperature (°C)	Density (g/cm³)	Porosity (%)	Vp (km/s)			mean Vp (km/s)	A vp (%)	Vs* (km/s)			mean Vs* (km/s)	A vs* (%)
					X	Y	Z			X	Y	Z		
15.9.91-b	25	20	1,93	24,31	3,944	3,882	3,788	3,871	4,04	2,253	2,373	2,195	2,274	11,68
	100	20	1,97	22,75	4,187	4,358	4,083	4,209	6,53	2,67	2,595	2,541	2,602	10,86
	100	600	1,96	23,14	4,231	4,489	4,203	4,308	6,66	2,695	2,665	2,588	2,650	10,72
MUZ 2000B	35	20	2,08	18,21	4,487	4,651	4,221	4,453	9,64	2,757	2,669	2,548	2,658	13,93
	100	20	2,10	17,42	5,093	5,233	4,778	5,035	9,03	3,002	2,802	2,668	2,824	14,70
	100	600	2,07	18,6	4,987	5,205	4,922	5,038	5,62	3,061	2,860	2,726	2,882	14,80
MUZ 2000E	25	20	2,19	13,68	4,052	4,414	4,306	4,257	8,49	2,530	2,541	2,432	2,501	10,29
	100	20	2,20	13,28	4,728	4,971	4,927	4,875	4,98	2,818	2,854	2,834	2,836	3,98
	100	600	2,17	14,47	4,861	5,125	5,124	5,037	5,23	2,882	2,955	2,930	2,922	3,37
MUZ 2000C	25	20	2,29	10,2	3,755	3,520	4,190	3,822	17,52	2,085	2,024	1,806	1,972	20,05
	100	20	2,31	9,41	4,922	4,569	5,032	4,841	9,56	2,288	2,297	2,018	2,201	22,63
	100	600	2,28	10,59	5,063	4,672	5,255	4,997	11,67	2,281	2,285	2,028	2,198	14,05
Ensp-2	25	20	2,45	6,13	4,339	4,147	3,955	4,147	9,25	2,516	2,484	2,420	2,473	7,54
	100	20	2,46	5,75	4,915	4,726	4,768	4,803	3,93	2,882	2,879	2,904	2,888	6,31
	100	600	2,42	7,28	5,249	5,130	5,231	5,204	2,28	3,122	3,105	3,018	3,081	9,55
MUZ 2000A	25	20	2,50	3,29	4,866	4,780	4,146	4,597	15,66	2,902	2,747	2,639	2,763	12,27
	100	20	2,51	2,9	5,482	5,446	5,114	5,347	6,88	3,172	3,162	3,117	3,150	3,55
	100	600	2,48	4,06	5,693	5,730	5,509	5,644	3,92	3,344	3,356	3,254	3,318	4,07

Table B.1: Summary of the elastic wave velocities, velocity anisotropy and density at room temperature and 600 °C.

Sample	mean porosity (vol. %)	initial pressure (MPa)	fragmentation speed (m/s)
MUZ 2001 A*	5,5	15	no fragmentation
	5,5	18	no fragmentation
	5,5	20	no fragmentation
	5,5	23	0
	5,5	25	0
	5,5	30	23,8
MUZ 2001 A	7,6	10	no fragmentation
	7,6	15	no fragmentation
	7,6	17	no fragmentation
	7,6	18	0
	7,6	20	11,7
	7,6	30	34
	7,6	40	45
MUZ 2000 D	13,3	7	no fragmentation
	13,3	9	no fragmentation
	13,3	11	no fragmentation
	13,3	12	no fragmentation
	13,3	13	0
	13,3	15	0
	13,3	20	20
	13,3	30	49,5
	13,3	40	64
MUZ 2001 C	20,8	5	no fragmentation
	20,8	6	no fragmentation
	20,8	7	no fragmentation
	20,8	8	no fragmentation
	20,8	8,5	0
	20,8	10	0
	20,8	11	0
	20,8	12	15,6
	20,8	24	38,5
	20,8	30	59
	20,8	40	76,5
MUZ 2000 G	33,0	3,2	no fragmentation
	33,0	4,2	no fragmentation
	33,0	5	no fragmentation
	33,0	6,3	28,3
	33,0	7	no fragmentation
	33,0	7	0
	33,0	8,3	0
	33,0	9,5	0
	33,0	10	22
	33,0	20	53,4
	33,0	30	66,5
	33,0	40	102,4

Table B.2: Results of fragmentation experiments conducted at samples from Unzen. The list comprehends experiments to determine the fragmentation threshold as well as speed of fragmentation.

Sample	mean porosity (vol. %)	initial pressure (MPa)	fragmentation speed (m/s)
MUZ 2000 F	33,8	2	no fragmentation
	33,8	3	no fragmentation
	33,8	4,4	no fragmentation
	33,8	5	0
	33,8	7	no fragmentation
	33,8	7,6	18,8
	33,8	10	no fragmentation
	33,8	10,5	38,7
	33,8	20	36,2
	33,8	30	90
MUZ BKB	52,2	2,2	no fragmentation
	52,2	3	no fragmentation
	52,2	3,8	0
	52,2	4,2	0
	52,2	10	43
	52,2	20	56
	52,2	30	81
	52,2	40	134

Table B.2 (continued): Results of fragmentation experiments conducted at samples from Unzen. The list comprehends experiments to determine the fragmentation threshold as well as speed of fragmentation.

Sample	mean porosity (vol. %)	initial pressure (MPa)	fragmentation speed (m/s)
MTSR very dense	2,5	15	no fragmentation
	2,5	20	no fragmentation
	2,5	25	no fragmentation
	2,5	30	0
	2,5	40	32
MTSR mid dense	19,4	5	no fragmentation
	19,4	7,5	no fragmentation
	19,4	9	no fragmentation
	19,4	10	0
	19,4	11	16,6
	19,4	15	22,4
	19,4	20	44,6
	19,4	25	51
	19,4	30	53
MTSR stripy	43,9	2	no fragmentation
	43,9	3,5	no fragmentation
	43,9	4,5	no fragmentation
	43,9	5	0
	43,9	6	22,4
	43,9	10	21,8
	43,9	15	60,4
	43,9	20	87
	43,9	25	69,9
	43,9	30,5	83
MTSR pumice	67,1	1,2	no fragmentation
	67,1	1,5	no fragmentation
	67,1	2	no fragmentation
	67,1	2,2	no fragmentation
	67,1	2,3	0
	67,1	2,45	no fragmentation
	67,1	2,5	0
	67,1	3,5	22
	67,1	4,1	34,6
	67,1	7,6	54,5
	67,1	10	70,5
	67,1	15	89,8
	67,1	20	107,4
	67,1	23,5	114
	67,1	25	132,7
	67,1	30	150

Table B.3: Results of fragmentation experiments conducted at samples from Montserrat. The list comprehends experiments to determine the fragmentation threshold as well as speed of fragmentation.

CURRICULUM VITAE

PERSÖNLICHE DATEN

Bettina Scheu, geboren am 01.06.1972 in Würzburg.

SCHULBILDUNG

1979 - 1983	Besuch der Burkarder Grundschule, Würzburg
1983 - 1992	Besuch des Wirsberg-Gymnasiums, Würzburg
Juli 1992	Erwerb der allgemeinen Hochschulreife

STUDIUM

1992 - 1995	Studium der Physik an der Julius-Maximilians-Universität Würzburg
Nov. 1994	Erwerb des Vordiploms in Physik
1995 - 1999	Studium der Geophysik an der Ludwig-Maximilians-Universität München
April 1999	Erwerb des Hauptdiploms in Geophysik
2000 - 2003	Promotionsstudiengang in Mineralogie an der Ludwig-Maximilians-Universität München

BERUFSTÄTIGKEIT

1999 - 2000	Wissenschaftliche Angestelle am Institut für Geophysik an der Ludwig-Maximilians-Universität München
2000 - 2002	Wissenschaftliche Angestellte am Institut für Mineralogie, Petrologie und Geochemie der Ludwig-Maximilians-Universität München
seit 2002	Wissenschaftliche Angestellte am Department für Geo- und Umweltwissenschaften der Ludwig-Maximilians-Universität München